

Electronic Thesis and Dissertation Repository

8-9-2013 12:00 AM

In Situ High-Pressure Studies of Ammonia Borane Derivatives by Vibrational Spectroscopy

Zhihao Yu, *The University of Western Ontario*

Supervisor: Yang Song, *The University of Western Ontario*

A thesis submitted in partial fulfillment of the requirements for the Master of Science degree in Chemistry

© Zhihao Yu 2013

Follow this and additional works at: <https://ir.lib.uwo.ca/etd>

 Part of the [Analytical Chemistry Commons](#), [Materials Chemistry Commons](#), and the [Physical Chemistry Commons](#)

Recommended Citation

Yu, Zhihao, "In Situ High-Pressure Studies of Ammonia Borane Derivatives by Vibrational Spectroscopy" (2013). *Electronic Thesis and Dissertation Repository*. 1403.
<https://ir.lib.uwo.ca/etd/1403>

This Dissertation/Thesis is brought to you for free and open access by Scholarship@Western. It has been accepted for inclusion in Electronic Thesis and Dissertation Repository by an authorized administrator of Scholarship@Western. For more information, please contact wlsadmin@uwo.ca.

IN SITU HIGH-PRESSURE STUDIES OF AMMONIA BORANE DERIVATIVES
BY VIBRATIONAL SPECTROSCOPY

(Thesis format: Integrated-Article)

by

Zhihao Yu

Graduate Program in Chemistry

A thesis submitted in partial fulfillment
of the requirements for the degree of
Master of Science

The School of Graduate and Postdoctoral Studies
The University of Western Ontario
London, Ontario, Canada

©Zhihao Yu 2013

Abstract

Hydrogen has been regarded as a promising candidate to replace conventional fossil fuels, and thus attracted enormous research efforts. However, hydrogen storage remains to be a big challenge to its practical applications. Consequently, the investigation of suitable hydrogen storage materials has become a highly active research field. Here, we report the first high pressure studies of three promising hydrogen storage materials, $\text{N}(\text{CH}_3)_3\text{BH}_3$, $\text{NH}(\text{CH}_3)_2\text{BH}_3$ and NaNH_2BH_3 , by Raman and IR spectroscopy.

First, $\text{N}(\text{CH}_3)_3\text{BH}_3$ was studied at room temperature and pressures up to 30 GPa. Under ambient conditions, $\text{N}(\text{CH}_3)_3\text{BH}_3$ forms rhombohedral crystals. During compression, two phase transitions were observed, which was evidenced by rich profile changes in Raman and IR spectra as well as by examining the pressure dependence of Raman and IR modes. Raman and IR spectra collectively revealed consistent structural information for $\text{N}(\text{CH}_3)_3\text{BH}_3$. The pressure-induced phase transitions were reversible, indicated by the recovered Raman and IR modes upon decompression.

Similarly, the other two hydrogen storage materials, $\text{NH}(\text{CH}_3)_2\text{BH}_3$ and NaNH_2BH_3 were investigated under high pressures up to 20 and 14 GPa, respectively. $\text{NH}(\text{CH}_3)_2\text{BH}_3$ was found to experience two phase transitions from the parent monoclinic structure. An interesting red shift and subsequent blue shift cycle of the N-H stretching mode was also observed. The decompression experiments suggested that the pressure-induced phase transitions were reversible. The changes in Raman and IR spectra under pressure together

with factor group analysis provided us a chance to examine the possible high-pressure structure. On the other hand, NaNH_2BH_3 , which crystalizes into an orthorhombic structure at ambient pressure, underwent two phase transitions during the compression process. The pressure-induced phase transitions turned out to be reversible upon decompression. Moreover, the bonding behaviors of NaNH_2BH_3 were found to be different from NH_3BH_3 , which has implications for improved hydrogen storage performance.

Keywords

High pressure, Hydrogen storage materials, Diamond anvil cell, Ammonia borane derivatives, Dimethylamine borane, Borane trimethylamine, Sodium amidoborane, Raman and IR spectroscopy

Acknowledgements

First of all, I would like to express my appreciation to my supervisor Dr. Yang Song for his patient guidance and encouragement in these two years. Without Dr. Song's lead and help, it's impossible to complete my work successfully. Dr. Song's professionalism and devotion to research make him an example to emulate. I would further like to thank Dr. Nicholas C. Payne and Dr. T.K. Sham for their instruction and help in and outside their course. In particular, I feel grateful for the recommendation letter from Dr. T.K. Sham.

Additionally, I would like to thank all members in Song's group, Dr. Vinod Panchal, Yue Hu, Ankang Zhao and Liang Zhou. It's them that helped my experiment go smoothly and made my life in the lab so joyful and colorful. I would like to extend my thanks to my friends, especially Ming Huang, Peng He, Xiaoxiao Wang, Xiaoxuan Guo, Zhiqiang Wang, Fuyan Zhao and Linda Wu. Without them, my memory in Canada couldn't have been so unforgettable and bright. It is you who drove the loneliness away from me.

Finally, I thank the help from Darlene McDonald and the guys in machine shop, Barakat, John and Jon.

I would like to dedicate this thesis to my parents for their selfless support and love.

Table of Contents

Abstract	ii
Acknowledgements	iv
Table of Contents	v
List of figures	ix
List of tables	xi
List of abbreviations	xii
Chapter 1: Introduction	1
1.1 Hydrogen energy and hydrogen storage materials	1
1.1.1 Hydrogen energy	1
1.1.2 Hydrogen storage materials	2
1.1.3 Ammonia-Borane and its derivatives for hydrogen storage	3
1.2 High pressure effect	5
1.3 High pressure studies of hydrogen storage materials	6
1.4 Motivation and thesis structure	11
1.5 Reference	12
Chapter 2: Instrumentation	16
2.1 High-pressure apparatus	16
2.1.1 Diamond anvil cell (DAC)	16
2.1.2 Pressure gauge	18
2.2 High-pressure vibrational spectroscopy	19

2.3 References.....	23
Chapter 3: <i>In-situ</i> high pressure study of borane trimethylamine by Raman and IR spectroscopy.....	25
3.1 Introduction.....	25
3.2 Experimental section.....	28
3.2.1 Sample preparation	28
3.2.2 High pressure Raman measurements	28
3.2.3 High pressure IR measurements	29
3.3 Results and discussion	30
3.3.1 Ambient-Pressure Raman and IR spectra	30
3.3.2 Raman spectra on compression.....	33
3.3.3 IR spectra on compression.....	36
3.3.4 Pressure effects on Raman and IR modes.....	38
3.3.5 Raman and IR spectra on decompression.....	41
3.3.6 Discussion	45
3.4 Conclusion	46
3.5 References.....	47
Chapter 4: <i>In-situ</i> high pressure study of dimethylamine borane by Raman and IR spectroscopy.....	50
4.1 Introduction.....	50
4.2 Experimental section.....	53
4.2.1 Sample preparation	53

4.2.2 High pressure Raman measurements	54
4.2.3 High pressure IR measurements	54
4.3 Results and discussion	55
4.3.1 Ambient-Pressure Raman and IR spectra.	55
4.3.2 Raman spectra on compression.....	57
4.3.3 IR Spectra on compression.	61
4.3.4 Pressure effects on Raman and IR modes.....	63
4.3.5 Raman and IR spectra on decompression.	67
4.3.6 Discussion	70
4.4 Conclusion	74
4.5 References.....	75
Chapter 5: Ball milling synthesis and <i>in-situ</i> high pressure study of sodium amidoborane	
.....	78
5.1. Introduction.....	78
5.2 Experimental section.....	81
5.2.1 Sample synthesis.....	81
5.2.2 Sample preparation	81
5.2.3 High pressure Raman measurements	82
5.2.4 High pressure IR measurements	83
5.3 Results and discussion	83
5.3.1 Ambient pressure Raman and IR spectra.....	83

5.3.2 Raman spectra on compression.....	86
5.3.3 IR spectra on compression.....	89
5.3.4 Pressure effects on Raman and IR modes.....	91
5.3.5 Raman and IR spectra on decompression.....	95
5.3.6 Discussion.....	98
5.4 Conclusion.....	100
5.5 References.....	101
Chapter 6: Summary and future work.....	104
6.1 Reference.....	105
Appendix.....	106
Curriculum Vitae.....	107

List of Figures

Figure 2.1 General schematic of a symmetric diamond anvil cell.....	17
Figure 2.2 Ruby fluorescence at different pressures.....	19
Figure 2.3 Schematic of the Raman system.....	21
Figure 2.4 Schematic diagram of the IR micro-spectroscopy system	23
Figure 3.1 Ambient-pressure crystal structure of BTMA.	27
Figure 3.2 Raman and IR spectra of BTMA at ambient pressure.	31
Figure 3.3 Selected Raman spectra of BTMA on compression.....	35
Figure 3.4 Selected IR spectra of BTMA on compression.	37
Figure 3.5 Pressure dependence of selected Raman modes of BTMA on compression...	39
Figure 3.6 Pressure dependence of selected IR modes of BTMA on compression	40
Figure 3.7 Selected Raman spectra of BTMA on decompression.	43
Figure 3.8 Selected IR spectra of BTMA on decompression.....	44
Figure 4.1 Ambient-pressure crystal structure of DMAB.....	51
Figure 4.2 Interchain interactions in the crystal structure of DMAB	52
Figure 4.3 Raman and IR spectra of DMAB in comparison with Raman spectrum of NH ₃ BH ₃ at ambient pressure	56
Figure 4.4 Selected Raman spectra of DMAB on compression	60
Figure 4.5 Selected IR spectra of DMAB on compression.....	62
Figure 4.6 Pressure dependence of selected Raman modes of DMAB on compression. .	65

Figure 4.7 Pressure dependence of selected IR modes of DMAB on compression	66
Figure 4.8 Selected Raman spectra of DMAB on decompression.....	69
Figure 4.9 Selected IR spectra of DMAB on decompression.....	70
Figure 5.1 Ambient-pressure crystal structure of NaAB.....	79
Figure 5.2 Raman and IR spectra of NaAB in comparison with Raman spectrum of NH ₃ BH ₃	84
Figure 5.3 Selected Raman spectra of NaAB on compression	88
Figure 5.4 Selected IR spectra of NaAB on compression.	90
Figure 5.5 Pressure dependence of selected Raman modes of NaAB on compression....	92
Figure 5.6 Pressure dependence of selected IR modes of NaAB on compression	93
Figure 5.7 Selected Raman spectra of NaAB on decompression	96
Figure 5.8 Selected IR spectra of NaAB on decompression.....	97

List of Tables

Table 1.1 Properties of hydrogen	2
Table 1.2 Summary of previous high pressure studies on hydrogen storage materials and systems	10
Table 3.1 Partial assignments and vibrational frequencies (cm^{-1}) of BTMA at ambient pressure	32
Table 3.2 Pressure dependence of the selected Raman modes of BTMA on compression	41
Table 3.3 Pressure dependence of the selected IR modes of BTMA on compression	41
Table 4.1 Partial assignments and vibrational frequencies (cm^{-1}) of DMAB at ambient pressure	57
Table 4.2 Pressure dependence of the selected Raman modes of DMAB on compression	67
Table 4.3 Pressure dependence of the selected IR modes of DMAB on compression	67
Table 4.4 Summary of the high pressure studies on methylamine-borane molecules, $\text{Me}_n\text{H}_{3-n}\text{N}\cdot\text{BH}_3$	73
Table 5.1 Partial assignments and vibrational frequencies (cm^{-1}) of NaAB at ambient pressure	85
Table 5.2 Pressure dependence of the selected Raman modes of NaAB on compression	94
Table 5.3 Pressure dependence of the selected IR modes of NaAB on compression	94

List of Abbreviations

BS	Beam splitter
CCD	Charge coupled device
DAC	Diamond anvil cell
FTIR	Fourier transform medium
IR	Infrared
IRIS	Infrared radiation interferometer spectrometer
MCT	Mercury cadmium telluride
NF	Notch filter
PTM	Pressure transmitting medium
XRD	X-ray diffraction
asym	Asymmetric
DMAB	Dimethylamine borane
BTMA	Borane trimethylamine
NaAB	Sodium amidoborane

Chapter 1. Introduction

1.1 Hydrogen energy and hydrogen storage materials

1.1.1 Hydrogen energy

Global warming and energy crisis are among the tremendous challenges that threaten the future of human beings. In order to tackle these challenges, a clean and highly efficient energy to replace the current large-scale-consumed fossil fuels is in urgent demand. In recent years, intensive research efforts have been devoted to the investigation of alternative energy sources, i.e. solar energy, nuclear energy, wind energy and hydrogen energy.^{1,2}

Unlike the conventional fossil fuels, the only combustion product of hydrogen is water without any emission of carbon dioxide. Moreover, hydrogen has excellent high energy density with per mass content of 143 MJ/kg, which is three times as high as liquid hydrocarbon based fuels.³ Also, researchers pointed out the hydrogen combusted in the same way as gasoline or natural gas in an internal combustion engine can provide 8% higher efficiency. Such outstanding properties make hydrogen one of the most promising candidates for both portable and stationary applications, and thus have attracted enormous research efforts.⁴⁻⁷

Hydrogen is the simplest and most abundant element in universe. It is colorless, odorless, and most importantly, non-toxic. Key properties of hydrogen are summarized in Table 1.1.

Table 1.1 Properties of hydrogen

Property	Value
Atomic weight	1.008
Color, odor	Colorless, odorless
Toxicity	None
Energy density	143 MJ/kg
Density	Gas: 0.089 g/L, liquid: 0.07 g/cm ³
Melting and boiling point	-259.14 °C, -252.87 °C

1.1.2 Hydrogen storage materials

To achieve the goal of widespread applications of hydrogen as the primary energy sources, several obstacles still remain to be overcome, such as the cost, regeneration and storage. Among these prominent issues, hydrogen storage is considered to be a key problem to be solved. To guide the research endeavors devoted to hydrogen storage, the U.S. Department of Energy (DOE) has set an ambitious target, that a gravimetric density of 9 wt% and a volumetric density of 82 g H₂·L⁻¹ should be fulfilled.⁸

Currently, there are two major strategies for hydrogen storage: physical storage and chemical storage.⁹ In physical storage, no covalent bonds or ionic interactions are formed between hydrogen and the host compound. In the category of physical storage, the high pressure tank technique is the most conventional and commercialized method,^{3,10} adopted

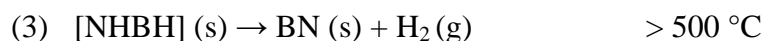
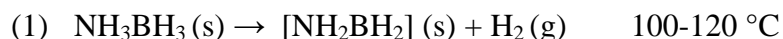
by most prototypes of fuel-cell-powered cars.⁹ Another technique focuses on porous materials, such as metal-organic frameworks (MOFs), zeolite and porous carbon. In such cases, hydrogen is physisorbed on the surface of pores via weak van der Waals forces, and thus the hydrogen storage capacity largely depends on the surface area and pore volume.⁵

On the other hand, for chemical storage, hydrogen is bonded to the storage medium through chemical bonds. Metal hydrides (e.g., MgH_2), complex hydrides (e.g., NaAlH_4) and amine-borane adducts (e.g., NH_3BH_3) belong to this class. In contrast to the physical hydrogen storage materials, the dehydrogenation of chemical storage materials requires high temperature owing to the strong interactions between hydrogen and the host compound. This is counted as a drawback for use as a fuel. However, the chemical hydrogen storage materials are still considered to be the ones closest to practical large-scale application due to their high hydrogen content.⁹ Recently, many breakthroughs have been achieved in the search for a suitable catalyst to lower the dehydrogenation temperature.¹¹⁻¹⁴

1.1.3 Ammonia-Borane and its derivatives for hydrogen storage

Among the various chemical hydrogen storage materials, ammonia borane is undoubtedly in the spotlight of this hot research field. Ammonia borane has several outstanding properties as a promising hydrogen storage material. First, it possesses a high

hydrogen content of 19.6 wt%, far exceeding the target set by the U.S Department of Energy. In addition, it is rather stable under ambient condition, neither flammable nor explosive.¹⁵ The thermal dehydrogenation of ammonia borane includes three steps and as follows^{16,17}:



Despite the aforementioned advantages, one drawback, however, is that toxic borazine is released during the decomposition process, which may poison the fuel cell. Another issue with NH_3BH_3 is its high decomposition temperature. These two major issues are considered as obstacles to practical use. For this reason, intense efforts have been devoted to lowering the decomposition temperature and to limiting the release of borazine.

Many approaches have been developed, such as incorporating ammonia borane into scaffolds, the use of iridium or base-metal catalysts, carbon cryogel and ionic liquid medium.^{13,18-21} One adopted strategy, chemical compositional modification, turns out to be an effective way. More and more research effort has been diverted to the derivatives of ammonia borane (e.g., dimethylamine borane, sodium amidoborane, lithium amidoborane), in the hope of finding an alternative storage materials with better performance.^{15,22-27} For example, NaNH_2BH_3 releases ~7.4 wt% hydrogen at around 91 °C, obviously lower than the onset dehydrogenation temperature of NH_3BH_3 at 108 °C.²⁸ Also, there is no borazine emission during the decomposition process.²⁹

Recently, the high pressure technique has been employed in developing novel hydrogen storage materials and many promising achievements have been reached. In the following section, the high pressure phenomenon will be discussed and more technical details can be found in Chapter 2.

1.2 High pressure effect

Pressure, as one of the three fundamental thermodynamic parameters, has a vital influence on the stability and the reactivity of chemical system. Pressure has a rather broad range, spanning over 60 orders of magnitude in the universe, from 10^{-32} Pascal in intergalactic space to 10^{32} Pascal in the center of a neutron star.

Nowadays, high pressure research in the laboratory is facilitated by anvil technology, which was originally developed by Nobel laureate Percy Bridgman. Thanks to the contribution of Percy Bridgman, high pressure research stepped into gigapascal (GPa) region. Now, the highest static pressure achieved in the laboratory has exceeded 100 GPa scale ($1 \text{ GPa} = 10^3 \text{ MPa} = 10^9 \text{ Pa} \approx 10^4 \text{ atm}$), comparable to the pressure at the Earth's core (330-360 GPa).^{30,31}

High pressure can drive materials to a lower volume state, efficiently shortening the inter-atomic and intra-atomic distance. Consequently, a number of interesting phenomena can occur, such as phase transitions, metallization, polymerization, ionization, amorphization and so on.³² High pressure has been proved to be an effective means to tune

the electronic, optical, magnetic and mechanical properties for novel applications.^{2,33} In fact, modern high pressure studies have demonstrated extraordinary breakthroughs in the discovery of superhard materials and superconductors. For example, cubic-BN synthesized under high pressure conditions has a comparable hardness to diamond.³⁴ For another example, superconducting behavior has been observed in the ionic salt CsI at high pressure.³⁵ More recently, high pressure scientists have expanded their research horizons on functional materials, including hydrogen storage materials and high energy density materials, which has become a vibrant research area.³⁶⁻⁴¹

1.3 High pressure studies of hydrogen storage materials

Supplementary to the traditional methods, recently, high pressure technique has been demonstrated as it a simple but effective as well as promising approach for developing potential hydrogen storage materials. The structure, stability and reversibility of hydrogen storage materials have fundamental influences on the storage performance. Under high pressure condition, the structure can be altered, and even unprecedented phases and complexes may be obtained, which has profound implications on improved hydrogen storage performance. Moreover, the high pressure study can provide a unique chance to reveal the atomic, electronic and structural information of potential storage materials, which in turn offers guidance for future design. For these reasons, numerous potential hydrogen storage materials have been intensively investigated under high pressure. A

detailed review article covering the current high pressure research progress on hydrogen storage materials is available.⁴²

The hydrogen-rich materials studied by high pressure techniques can be classified into four groups: (1) simple hydrides (e.g., LiH, MgH₂, AlH₃), (2) complex hydrides (LiAlH₄, NaBH₄) (3) chemical hydrides (e.g., B₂H₆, NH₃BH₃) (4) hydrogen containing complexes (CH₄-H₂, H₂O-H₂, NH₃BH₃-H₂). Various methods have been adopted to monitor the high pressure behavior of potential hydrogen storage materials, such as Raman, IR spectroscopy, X-ray diffraction. Previous high pressure studies of different hydrides are summarized in Table 1.2.⁴²

For instance, as a member of the simple hydride family, MgH₂ has received intensive investigations under high pressure, and was found to exhibit various phases in the high pressure region. At about 2 GPa, MgH₂ experienced a dramatic transition from α -MgH₂ to β -MgH₂.⁴³ In a subsequent experiment, a γ -MgH₂ was confirmed at 3.8 GPa.⁴⁴ More recently, the phase diagram of MgH₂ was further updated through theoretical calculation.⁴⁵ Both experimental and theoretical research suggests that MgH₂ has a strong ionic character. Thus, it can be predicted that weakening the ionic bond by pressure modification is possible to improve the dehydrogenation process.

As another example, with a gravimetric hydrogen content of 10.5 wt%, LiAlH₄ is a representative chemical in the class of complex hydrides. Under ambient conditions, LiAlH₄ crystallizes into α -phase with a monoclinic structure.⁴⁶ A slow and reversible phase transition from α to β was observed by Raman spectroscopy between 2.2 and 3.5 GPa.⁴⁷

Later, Chellappa *et al.* found that β -LiAlH₄ has a distorted [AlH₄⁻] tetrahedron with softened Al-H stretching mode.⁴⁸ The Al-H bond in AlH₄⁻ is believed to have important effects on the hydrogen release process. The weakening of the Al-H bond may have profound implications for the storage performance.

With excellent advantages such as high hydrogen capacity and stability, ammonia borane (NH₃BH₃) has been examined and reviewed extensively.⁴⁹⁻⁵² In recent years, it has attracted much attention from high pressure scientists. Under ambient conditions, NH₃BH₃ crystallizes into a tetragonal structure with the space group *I4mm*.⁵³ Two phase transitions were monitored upon compression to 4 GPa in early spectroscopy studies.⁵⁴ In the subsequent researches conducted by Lin *et al.*⁵⁵ and Xie *et al.*⁵⁶ respectively, similar new phase transitions were observed. Later, through X-ray diffraction and theoretical calculations, a new orthorhombic structure was established at 1.5 GPa.^{57,58} More recently, Liu and Song further extended the phase diagram of NH₃BH₃ in the temperature range of 80 to 350 K, and the pressure range from ambient to 15 GPa aided by *in situ* low-temperature Raman spectroscopy.⁴⁰ At the same time, a new phase was reported by Lin *et al.* at above 12.9 GPa with the help of synchrotron X-ray powder diffraction as well as density functional calculations.⁵⁹

In the case of hydrogen-containing complexes, hydrogen is enclosed as guest molecules in the framework constructed by the host molecules (e.g., CH₄, SiH₄ and NH₃BH₃) under high pressures.⁶⁰ Most of the host molecules are already hydrogen-rich compounds. Encapsulating hydrogen into the hydrogen-rich system with the aid of high pressure will

remarkably improve the hydrogen content, which is desirable for hydrogen storage. This approach is originated from the pioneering work of Vos *et al.*, who first reported the H₂O-H₂ system under high pressure.⁶¹ Subsequently, other hydrogen containing complexes, such as CH₄-H₂ and NH₃BH₃-H₂ were reported. Multiple molecular compounds, CH₄(H₂)₂, (CH₄)₂H₂, CH₄(H₂)₄ and CH₄H₂ were observed at pressures up to 10 GPa.⁶² In 2009, a novel complex, NH₃BH₃(H₂)_x (x=1.3-2) with 30 wt% H₂, was obtained at above 6.2 GPa.⁴¹

Table 1.2 Summary of previous high pressure studies on hydrogen storage materials and systems^a

Materials	Hydrogen content	Structural information	Pressure range^b(GPa)	Temperature range^b(K)
<i>Simple hydride</i>				
LiH	12.6%	$Fm\bar{3}m$	250	room
NaH	4.2%	$Fm\bar{3}m$ (B1); $Pm\bar{3}m$ (B2)	54	room
MgH ₂	7.6%	$P4_2/mnm$ (α); $Pa\bar{3}$ (β); $Pbcn$ (γ); $Pbca$ (δ)	16	1070
CaH ₂	4.8%	$Pnma$; $P6_3/mmc$	42	room
AlH ₃	10.0%	$R\bar{3}c$ (α); $Cmcm$ (α'); $Fd\bar{3}m$ (β); $Pnmm$ (γ); $P2$ (α -II); $Pm\bar{3}n$ (α -III)	164	4
<i>Complex hydride</i>				
LiAlH ₄	10.5%	$P2_1/c$ (α); $I2/b$ (β)	7	773
NaAlH ₄	7.4%	$I4_1/a$ (α); $P2_1/c$ (β)	27	room
LiBH ₄	18.4%	$Pnma$; $P6_3mc$; $Ama2$; $Fm\bar{3}m$	10	500
NaBH ₄	10.6%	$Fm\bar{3}m$ (α); $P4_2/c$ (β); $Pnma$ (γ)	30	80-673
Ca(BH ₄) ₂	11.5%	$Fddd$ (α); $P\bar{4}$ (β); $Pbca$ (γ); $I\bar{4}2d$ (α')	10	873
LiNH ₂	8.8%	$I\bar{4}$ (α); $P2_1$ (β)	28	room
NaNH ₂	5.2%	$Fddd$	16	room
<i>Chemical hydride</i>				
B ₂ H ₆	22%	$P2_1/n$ (β)	50	room
NH ₃ BH ₃	19%	$I4mm$; $Pmn2_1$; $Cmc2_1$; $P2_1$	65	15-350
<i>H₂ containing complex</i>				
CH ₄ -H ₂	50%	CH ₄ (H ₂) ₂ ; (CH ₄) ₂ H ₂ ; CH ₄ (H ₂) ₄ ; CH ₄ H ₂	60	10
H ₂ O-H ₂	20%	C ₁ ; C ₂ ; sII	80	10-450
NH ₃ BH ₃ -H ₂	29%	NH ₃ BH ₃ (H ₂) _x x=1.3-2	60	413
Ar-H ₂ &Xe-H ₂	9%&9.7%	Ar(H ₂) ₂ - $P6_3/mmc$; Xe(H ₂) ₇ - $R3$	200&255	room

^a This table is adapted from reference 42

^b For pressure, the range goes from ambient to the given value; for temperature, “room” refers to 298 K, the value refers to either the maximum or the minimum or to a range of temperature under which the materials were investigated under simultaneous high pressure conditions.

1.4 Motivation and thesis structure

As is mentioned above, although ammonia borane is regarded as a promising hydrogen storage material, there are still several prominent problems such as high onset dehydrogenation temperature and release of borazine, which limits its practical applications. Thus, the researchers have embarked on investigations of ammonia borane derivatives in the hope of finding a more suitable hydrogen storage material, and gaining enlightenments for the design of novel materials in the future. Many ammonia borane derivatives, such as LiNH_2BH_3 , NaNH_2BH_3 , $\text{NH}(\text{CH}_3)_2\text{BH}_3$ and $\text{N}(\text{CH}_3)_3\text{BH}_3$, have received extensive investigations under ambient conditions, with respect to structure, stability and dehydrogenation mechanism. However, few high pressure studies of ammonia borane derivatives have been reported. In my project, three compounds, $\text{NH}(\text{CH}_3)_2\text{BH}_3$, $\text{N}(\text{CH}_3)_3\text{BH}_3$ and NaNH_2BH_3 , were chosen to be examined for high pressure studies of their structures and properties by Raman and IR spectroscopy, which may extend our knowledge and shed light on the future design. Moreover, this project can contribute to finding a novel phase that has profound implications for improved hydrogen storage performance.

The layout of the thesis is as follows. Chapter 1 provides a general introduction of hydrogen storage materials. Chapter 2 focuses on the instrumentation including the diamond anvil cell (DAC), Raman and IR spectroscopy used in this thesis. Chapters 3 to 5

are the body chapters, in which detailed high pressure studies of $\text{NH}(\text{CH}_3)_2\text{BH}_3$, $\text{N}(\text{CH}_3)_3\text{BH}_3$ and NaNH_2BH_3 are included. Finally, Chapter 6 summarizes the general conclusions and proposes suggestions for future work.

1.5 Reference

- (1) Dunn, S. *Int. J. Hydrogen Energy* **2002**, 27, 235.
- (2) Liu, A. *In-situ high pressure studies of Hydrogen storage materials by vibrational spectroscopy* (M.Sc. thesis) University of Western Ontario, **2011**.
- (3) Mazloomi, K.; Gomes, C. *Renewable & Sustainable Energy Rev.* **2012**, 16, 3024.
- (4) Symes, M. D.; Cronin, L. *Nat. Chem.* **2013**, 5, 403.
- (5) Suh, M. P.; Park, H. J.; Prasad, T. K.; Lim, D. W. *Chem. Rev.* **2012**, 112, 782.
- (6) Van den Berg, A. W. C.; Arean, C. O. *Chem. Commun.* **2008**, 668.
- (7) Regatte, V. R.; Kaisare, N. S. *Chem. Eng. J.* **2013**, 215, 876.
- (8) Satyapal, S.; Petrovic, J.; Read, C.; Thomas, G.; Ordaz, G. *Catal. Today* **2007**, 120, 246.
- (9) Eberle, U.; Felderhoff, M.; Schuth, F. *Angew. Chem. Int. Ed.* **2009**, 48, 6608.
- (10) Ding, F.; Yakobson, B. I. *Front Phys-Beijing* **2011**, 6, 142.
- (11) Appelt, C.; Sloopweg, J. C.; Lammertsma, K.; Uhl, W. *Angew. Chem. Int. Ed.* **2013**, 52, 4256.
- (12) Tang, Z.; Chen, X.; Chen, H.; Wu, L.; Yu, X. *Angew. Chem. Int. Ed.* **2013**, 52, 5832.
- (13) Keaton, R. J.; Blacquiere, J. M.; Baker, R. T. *J. Am. Chem. Soc.* **2007**, 129, 1844.
- (14) Paul, A.; Musgrave, C. B. *Angew. Chem. Int. Ed.* **2007**, 46, 8153.
- (15) Xiong, Z. T.; Yong, C. K.; Wu, G. T.; Chen, P.; Shaw, W.; Karkamkar, A.; Autrey, T.; Jones, M. O.; Johnson, S. R.; Edwards, P. P.; David, W. I. F. *Nat. Mater.* **2008**, 7,

138.

- (16) Hu, M. G.; Geanangel, R. A.; Wendlandt, W. W. *Thermochim. Acta* **1978**, *23*, 249.
- (17) Sit, V.; Geanangel, R. A.; Wendlandt, W. W. *Thermochim. Acta* **1987**, *113*, 379.
- (18) Gutowska, A.; Li, L. Y.; Shin, Y. S.; Wang, C. M. M.; Li, X. H. S.; Linehan, J. C.; Smith, R. S.; Kay, B. D.; Schmid, B.; Shaw, W.; Gutowski, M.; Autrey, T. *Angew. Chem. Int. Ed.* **2005**, *44*, 3578.
- (19) Denney, M. C.; Pons, V.; Hebden, T. J.; Heinekey, D. M.; Goldberg, K. I. *J. Am. Chem. Soc.* **2006**, *128*, 12048.
- (20) Bluhm, M. E.; Bradley, M. G.; Butterick, R.; Kusari, U.; Sneddon, L. G. *J. Am. Chem. Soc.* **2006**, *128*, 7748.
- (21) Feaver, A.; Sepehri, S.; Shamberger, P.; Stowe, A.; Autrey, T.; Cao, G. *J. Chem. Phys.* **2007**, *111*, 7469.
- (22) Sewell, L. J.; Huertos, M. A.; Dickinson, M. E.; Weller, A. S.; Lloyd-Jones, G. C. *Inorg. Chem.* **2013**, *52*, 4509.
- (23) Zahmakiran, M.; Philippot, K.; Ozkar, S.; Chaudret, B. *Dalton Trans.* **2012**, *41*, 590.
- (24) Nixon, T. D.; Whittlesey, M. K.; Williams, J. M. J. *Tetrahedron Lett.* **2011**, *52*, 6652.
- (25) Kalidindi, S. B.; Esken, D.; Fischer, R. A. *Chem. Eur. J.* **2011**, *17*, 6594.
- (26) Wolstenholme, D. J.; Titah, J. T.; Che, F. N.; Traboulee, K. T.; Flogeras, J.; McGrady, G. S. *J. Am. Chem. Soc.* **2011**, *133*, 16598.
- (27) Sandra, F. P. R.; Demirci, U. B.; Chiriac, R.; Moury, R.; Miele, P. *Int. J. Hydrogen Energy* **2011**, *36*, 7423.
- (28) Xiong, Z. T.; Wu, G. T.; Chua, Y. S.; Hu, J. J.; He, T.; Xu, W. L.; Chen, P. *Energ Environ. Sci.* **2008**, *1*, 360.
- (29) Huang, Z. G.; Autrey, T. *Energ Environ. Sci.* **2012**, *5*, 9257.
- (30) Weir, C. E.; Lippincott, E. R.; Vanvalkenburg, A.; Bunting, E. N. *J. Res. Nbs. a*

Phys. Ch. **1959**, 63, 55.

- (31) Dong, Z. *High-pressure study of molecular solids and 1D nanostructures by vibrational spectroscopy and synchrotron X-ray diffraction* (Ph.D. thesis) University of Western Ontario, **2012**.
- (32) Grochala, W.; Hoffmann, R.; Feng, J.; Ashcroft, N. W. *Angew. Chem. Int. Ed.* **2007**, 46, 3620.
- (33) Hemley, R. J.; Mao, H. K. *Aip. Conf. Proc.* **2004**, 706, 17.
- (34) McMillan, P. F. *Nat. Mater.* **2002**, 1, 19.
- (35) Eremets, M. I.; Shimizu, K.; Kobayashi, T. C.; Amaya, K. *J. Phys.: Condens. Matter* **1998**, 10, 11519.
- (36) Song, Y.; Manaa, M. R. *J. Chem. Phys. C* **2012**, 116, 2059.
- (37) Vaitheeswaran, G.; Babu, K. R. *J. Chem. Sci.* **2012**, 124, 1391.
- (38) Hu, A. G.; Zhang, F. In *Shock Compression of Condensed Matter - 2011, Pts 1 and 2*; Elert, M. L., Buttler, W. T., Borg, J. P., Jordan, J. L., Vogler, T. J., Eds.; Amer Inst Physics: Melville, 2012; Vol. 1426.
- (39) Najiba, S.; Chen, J. H. *P Proc. Natl. Acad. Sci. U.S. A.* **2012**, 109, 19140.
- (40) Liu, A.; Song, Y. *J. Phys. Chem. C* **2012**, 116, 2123.
- (41) Lin, Y.; Mao, W. L.; Mao, H. K. *Proc. Natl. Acad. Sci. U.S. A.* **2009**, 106, 8113.
- (42) Song, Y. *Phys. Chem. Chem. Phys.* **2013**, in press
- (43) Bortz, M.; Bertheville, B.; Bottger, G.; Yvon, K. *J. Alloy Compd.* **1999**, 287, L4.
- (44) Vajeeston, P.; Ravindran, P.; Hauback, B. C.; Fjellvag, H.; Kjekshus, A.; Furuseth, S.; Hanfland, M. *Phys. Rev. B* **2006**, 73.
- (45) Moser, D.; Baldissin, G.; Bull, D. J.; Riley, D. J.; Morrison, I.; Ross, D. K.; Oates, W. A.; Noreus, D. *J. Phys.: Condens. Matter* **2011**, 23.
- (46) Hauback, B. C.; Brinks, H. W.; Fjellvag, H. *J. Alloy Compd.* **2002**, 346, 184.
- (47) Talyzin, A. V.; Sundqvist, B. *Phys. Rev. B* **2004**, 70.
- (48) Chellappa, R. S.; Chandra, D.; Gramsch, S. A.; Hemley, R. J.; Lin, J. F.; Song, Y. J.

- Phys. Chem. B* **2006**, *110*, 11088.
- (49) Yamauchi, K.; Hamada, I.; Huang, H. B.; Oguchi, T. *Appl. Phys. Lett.* **2011**, *99*.
- (50) Liang, Y. F.; Tse, J. S. *J. Phys. Chem. C* **2012**, *116*, 2146.
- (51) Marder, T. B. *Angew. Chem. Int. Ed.* **2007**, *46*, 8116.
- (52) Hamilton, C. W.; Baker, R. T.; Staubitz, A.; Manners, I. *Chem. Soc. Rev.* **2009**, *38*, 279.
- (53) Bowden, M. E.; Gainsford, G. J.; Robinson, W. T. *Aust. J. Chem.* **2007**, *60*, 149.
- (54) Custelcean, R.; Dreger, Z. A. *J. Phys. Chem. B* **2003**, *107*, 9231.
- (55) Lin, Y.; Mao, W. L.; Drozd, V.; Chen, J. H.; Daemen, L. L. *J. Chem. Phys.* **2008**, *129*.
- (56) Xie, S. T.; Song, Y.; Liu, Z. X. *Can. J. Chem.* **2009**, *87*, 1235.
- (57) Filinchuk, Y.; Nevidomskyy, A. H.; Chernyshov, D.; Dmitriev, V. *Phys. Rev. B* **2009**, *79*.
- (58) Chen, J. H.; Couvy, H.; Liu, H. Z.; Drozd, V.; Daemen, L. L.; Zhao, Y. S.; Kao, C. *Int. J. Hydrogen Energy* **2010**, *35*, 11064.
- (59) Lin, Y.; Ma, H. W.; Matthews, C. W.; Kolb, B.; Sinogeikin, S.; Thonhauser, T.; Mao, W. L. *J. Phys. Chem. C* **2012**, *116*, 2172.
- (60) Struzhkin, V. V.; Militzer, B.; Mao, W. L.; Mao, H. K.; Hemley, R. J. *Chem. Rev.* **2007**, *107*, 4133.
- (61) Vos, W. L.; Finger, L. W.; Hemley, R. J.; Mao, H. K. *Phys. Rev. Lett.* **1993**, *71*, 3150.
- (62) Somayazulu, M. S.; Finger, L. W.; Hemley, R. J.; Mao, H. K. *Science* **1996**, *271*, 1400.

Chapter 2. Instrumentation

2.1 High-pressure apparatus

2.1.1 Diamond anvil cell (DAC)

Static high pressure studies in the last few decades have been assisted by the diamond anvil cell (DAC), a device used to generate and maintain high pressures up to ~360 GPa. The modern DAC with two opposing diamonds acting as anvils was developed by Weir and his colleagues in the National Bureau of Standards.^{1,2} Diamonds were used because they are known as the hardest material in nature and, therefore, could sustain extreme high pressure. In addition, diamonds have excellent transparency in a broad spectral range, and thus can be utilized for structural characterization of materials under high pressure by various *in situ* probes, such as vibrational spectroscopy and X-ray diffraction (XRD).

Basically, there are two types of diamonds used in the DAC techniques, namely types I and II. Both diamonds have an intense first order Raman line at 1334 cm^{-1} .³ In terms of infrared absorption, Type I diamonds with higher impurity (e.g., nitrogen) have two strong absorption regions, which are at around 2000 cm^{-1} and $1000\text{-}1350\text{ cm}^{-1}$. In contrast, type II diamonds which only show IR absorption at around 2000 cm^{-1} allow IR measurements in the DAC. Based on their different properties, type I diamonds are only suitable for Raman spectroscopy, while type II diamonds are widely used for IR spectroscopy.

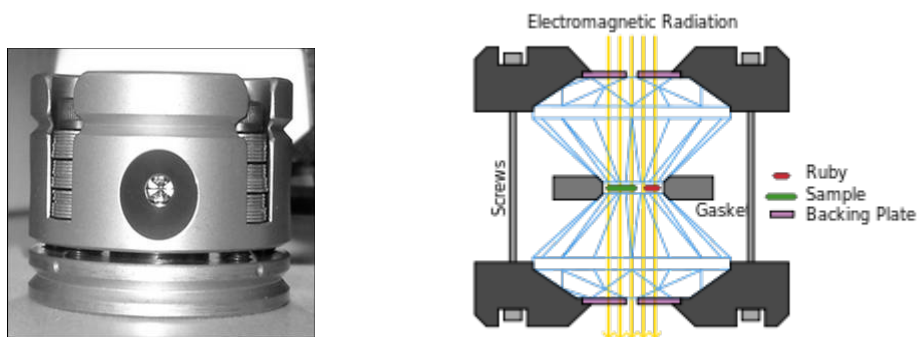


Figure 2.1 Left: the photo of a diamond anvil cell; right: schematic drawing of a DAC with the diamond anvils enlarged. (Adapted from Ref. 4)

Nowadays, in order to meet the requirements of various high pressure experiments, DACs have evolved into many types such as Merrill-Bassett type DAC for high temperature measurements⁵ and symmetric DAC for room temperature experiments.⁶ The schematic of a symmetric DAC is shown in Fig. 2.1. A pair of diamond anvils is mounted on the two supporting seats, typically made of tungsten carbide. The tips of the diamond anvils are generally tens to hundreds of microns in diameter. A pre-indented gasket with a hole drilled at the center is placed between the two diamonds, acting as the sample chamber. The backup seats will generate a pressure once a small force is applied to the DAC by tightening the screws. The low pressure will be amplified by the shape of the diamond tip and yield a much higher pressure on the tip.

2.1.2 Pressure gauge

A reliable and accurate way to determine the pressure inside the DAC is a vital component in high-pressure experiments. Based on Mao's work, a ruby fluorescence method was well-established, and is adopted in this thesis.⁷

Ruby, which is Al_2O_3 doped with Cr^{3+} , is loaded into the sample hole together with samples. It has two intense luminescent peaks R_1 and R_2 (Fig. 2.2) when excited by lasers. The positions of the R_1 and R_2 peaks are pressure-dependent and shift to a longer wavelength as pressure increases. Mao reported an equation (eq. 2.1) shown below to describe the relation between pressure and R_1 position.

$$P = \frac{1904}{B} \left[\left(1 + \frac{\Delta\lambda}{694.24} \right)^B - 1 \right] \quad (2.1)$$

where P is the *in-situ* pressure in GPa, and $\Delta\lambda$ is the difference between the wavelength of R_1 in nm at pressure P and that at ambient pressure. The parameter B equals 7.665 under quasi-hydrostatic condition, and 5 under non-hydrostatic condition. Using this method, the resolution of the pressure can be achieved to ± 0.05 GPa.

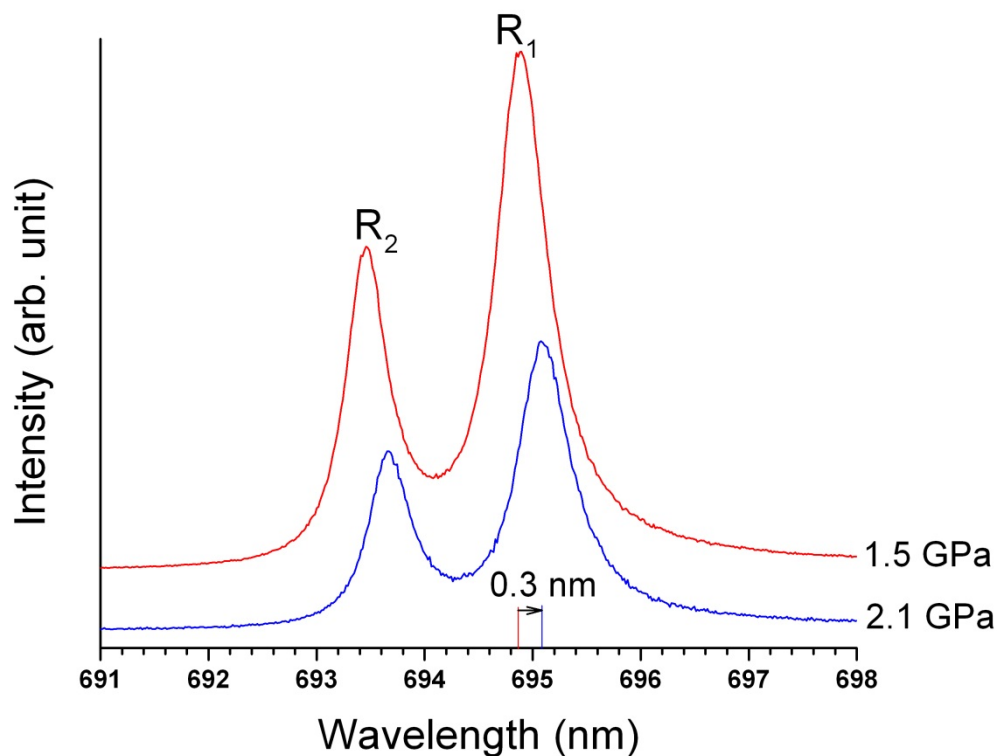


Figure 2.2 Ruby fluorescence measured at different pressures with the two luminescent peaks labeled (R_1 and R_2). The pressure condition for each spectrum is labeled beside. (Adapted from Ref. 4)

2.2 High-pressure vibrational spectroscopy

Raman and IR absorption spectroscopies, whose designs are compatible with the DAC, are widely used in high pressure studies. Both Raman and IR spectroscopies can provide similar information about molecular vibrations, but their selection rules are different. If the vibration in the molecules can cause a change in polarizability, the vibration mode is Raman-active. On the other hand, if dipole moment is changed, this mode is considered as IR-active. In a practical situation, a vibration can be either Raman-active or IR-active, and

even active/inactive to both probes. For this reason, for the non-silent vibrations, IR spectra and Raman spectra are complementary to each other.⁸

Raman spectroscopy originates from the scattering of monochromatic light, normally from a laser in the visible, near infrared, or near ultraviolet range. After interactions with atoms or molecules in the sample, a small amount of laser photons are scattered. Among the scattered photons, most of them have the same frequency as the incident beam, which is referred to as Rayleigh scattering, and therefore carry no spectroscopic information. At the same time, some photons are scattered with frequencies lower or higher than the incident beam; the former process is referred to as Stokes scattering while the latter is called anti-Stokes scattering. Energies between the incident and the anti-Stokes or Stokes energies fall into the gaps between different vibrational or rotational energy levels of the molecule in the sample. In consequence, valuable spectroscopic information for the vibrational or rotational energy levels of that sample can be revealed by the measurement of Raman shifts (energy differences between the incident beam and Stokes/anti-Stokes scattering).

IR absorption spectroscopy is based on the absorption of the incident infrared beam in molecules. Molecules will be excited to various discrete vibrational or rotational energy levels through absorbing infrared photons. Monitoring the absorption can provide vibrational information of studied molecules.

A customized Raman system was used for Raman measurements in our lab. The schematic diagram of this Raman system is depicted in Fig. 2.3. The system is

constructed on an optical table. Briefly, a single longitudinal mode, pumped solid state green laser was used as the excitation source. The Raman signal was detected by the objective lens with backscattering geometry. A pair of notch filters was used to remove the Rayleigh scattering. The scattered light was then dispersed by an imaging spectrograph equipped with a triple grating. The Raman signal was recorded using an ultrasensitive, liquid nitrogen cooled, back-illuminated and charge-coupled device (CCD) detector from Acton. The system was calibrated by neon lines with an uncertainty of $\pm 1 \text{ cm}^{-1}$.

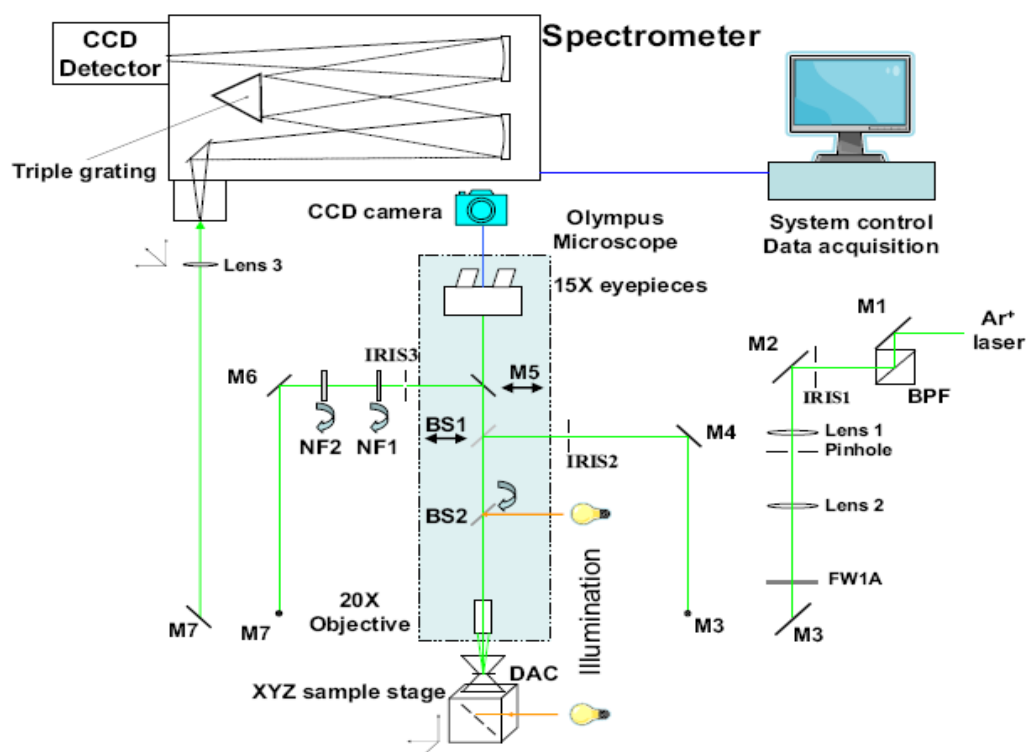


Figure 2.3 Schematic of the Raman system. BPF: band path filter; IRIS: IRIS aperture; M1-7: broadband dielectric reflecting mirrors; FW1A: Six station filter wheel; BS: beam splitter; NF: notch filter; DAC: diamond anvil cell; Triple gratings: 300 lines/mm, 1200 lines/mm, and 1800 lines/mm. Blue area is the microscope system with a CCD camera,

which is perpendicular to the other parts. (Adapted from Ref. 4)

In our lab, a customized IR micro-spectroscopy system was used for all room-temperature IR absorption measurements. A commercial Fourier transform infrared (FTIR) spectrometer (Model Vertex 80v) from Bruker Optics Inc. equipped with Global mid-IR light source constituted the main component of the micro-IR system. The system was operated under a vacuum of < 5 mbar so the H_2O and CO_2 absorption could be efficiently removed. A collimated IR beam was directed into a relay box through a KBr window on the spectrometer and then focused onto the sample by an iris optics and $15\times$ reflective objective lens with a numerical aperture of 0.4. The diameter of the IR beam was adjusted to be identical to the entire sample size (e.g., $\sim 150 \mu\text{m}$) by a series of iris apertures. The transmitted IR beam was collected using another identical reflective objective as the condenser, and was then directed to a wide-band mercury cadmium telluride (MCT) detector equipped with a ZnSe window that enables a spectral range of 400 to 10000 cm^{-1} to be measured.⁸

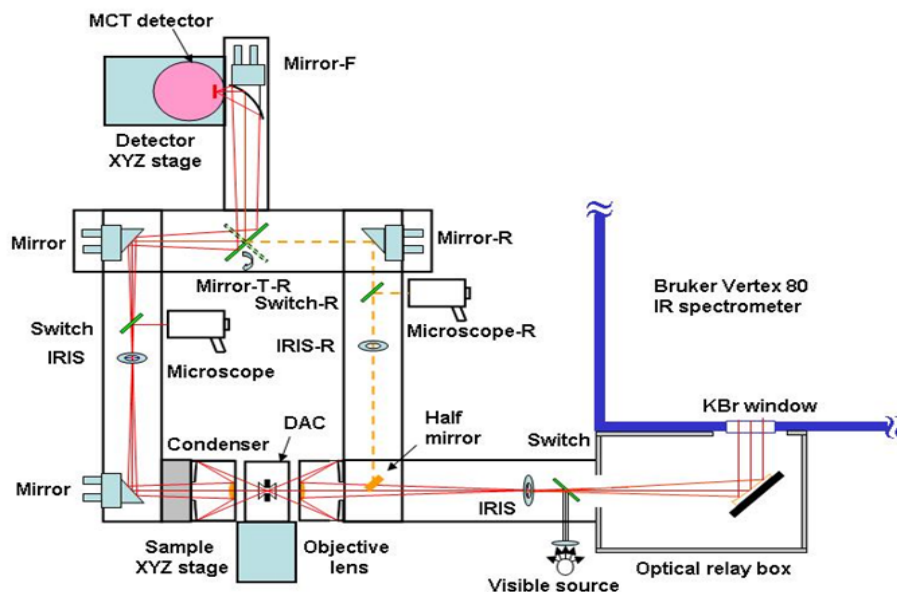


Figure 2.4 Schematic diagram of the IR micro-spectroscopy system. All major optical components are labeled. Those with ‘-R’ and half mirror are for reflection measurements while the rest for transmission/absorption measurements. ‘Switch’ refers to switchable mirrors for illumination purpose. ‘mirror-T-R’ is a mirror used to switch between transmission and reflection modes. ‘Mirror-F’ is used to focus the IR signal to the detector. (Adapted from Ref. 8)

2.3 References

- (1) Block, S.; Piermarini, G. *Phys. Today* **1976**, 29, 44.
- (2) Block, S.; Piermarini, G. *Usp. Fiz. Nauk* **1979**, 127, 705.
- (3) Solin, S. A.; Ramdas, A. K. *Phys. Rev. B* **1970**, 1, 1687.
- (4) Dong, Z. *High-pressure study of molecular solids and 1D nanostructures by vibrational spectroscopy and synchrotron X-ray diffraction* (Ph.D. thesis) University of Western Ontario, **2012**.
- (5) Schiferl, D. *Rev. Sci. Instrum.* **1987**, 58, 1316.

- (6) Jayaraman, A. *Rev. Mod. Phys.* **1983**, 55, 65.
- (7) Mao, H. K.; Xu, J.; Bell, P. M. *J. Geophys. Res.-Solid* **1986**, 91, 4673.
- (8) Liu, A. *In-situ high pressure studies of Hydrogen storage materials by vibrational spectroscopy* (M.Sc. thesis) University of Western Ontario, **2011**.

Chapter 3. *In-situ* high pressure study of borane trimethylamine by Raman and IR spectroscopy

3.1 Introduction

Regarded as one of the promising hydrogen storage materials, NH_3BH_3 has attracted immense research interest over the past decade.¹⁻¹⁰ With high gravimetric hydrogen content of 19.5 wt%, NH_3BH_3 far exceeds the requirement (9 wt%) of the U.S. Department of Energy for on-board hydrogen systems.¹¹

Under high pressure conditions, materials may display a series of changes in molecular structures and associated properties, such as enhanced hydrogen storage capacities.¹² Therefore, a wide range of hydride complexes (e.g., ammonia borane, diborane, metal hydrides, calcium borohydride and sodium amide) as potential hydrogen storage materials have been studied under extreme high pressure.¹³⁻¹⁹ Recently, NH_3BH_3 has been extensively studied under high pressures by means of vibrational spectroscopic techniques such as Infrared and Raman spectroscopy, X-ray diffraction and neutron diffraction.^{17,20-23} Based on previous efforts by many researchers, Liu *et al.* determined the phase diagram of NH_3BH_3 in the pressure region of 0-15 GPa and temperature region of 80-350 K.¹⁷

Although we have gained deep insights into the structure and related properties of NH_3BH_3 owing to previous research, there are still many problems which limit application of NH_3BH_3 . NH_3BH_3 has intrinsic disadvantages such as high decomposition temperature

and borazine released in the decomposition process which may damage the fuel cell.^{24,25}

Investigating the derivatives of NH_3BH_3 will therefore help us find an alternative ammonia borane-based hydrogen storage material with improved performance. Recently, for example, Russell *et al.* have used Raman spectroscopy and synchrotron X-ray diffraction to examine the high pressure behavior of tetramethylammonium borohydride (TMAB) at room temperature.²⁶

To continue the high pressure research on ammonia borane derivatives, we shifted our focus to another compound in this series, borane trimethylamine ($\text{N}(\text{CH}_3)_3\text{BH}_3$). Compared to ammonia borane, borane trimethylamine (BTMA) may not be an ideal hydrogen storage material due to its relatively low hydrogen content. However, systematic study of the derivative series of NH_3BH_3 will allow a more in-depth understanding of structures and bonding properties of amine borane complexes, and thus may provide some guidance for choosing and improving potential hydrogen storage materials.

As shown in Figure 3.1, at ambient conditions, $\text{N}(\text{CH}_3)_3\text{BH}_3$ forms rhombohedral crystals with space group $R\bar{3}m$ and cell parameters $a = 9.079 \text{ \AA}$, $b = 9.079 \text{ \AA}$, $c = 5.892 \text{ \AA}$.²⁷ In Naresh's theoretical study, C-H \cdots H-B dihydrogen bonding is predicted between BTMA and acetylenes.²⁸ In addition, a dehydrogenation reaction was once reported between dihydrogen bonded borane trimethylamine and phenol in the gas phase.²⁹

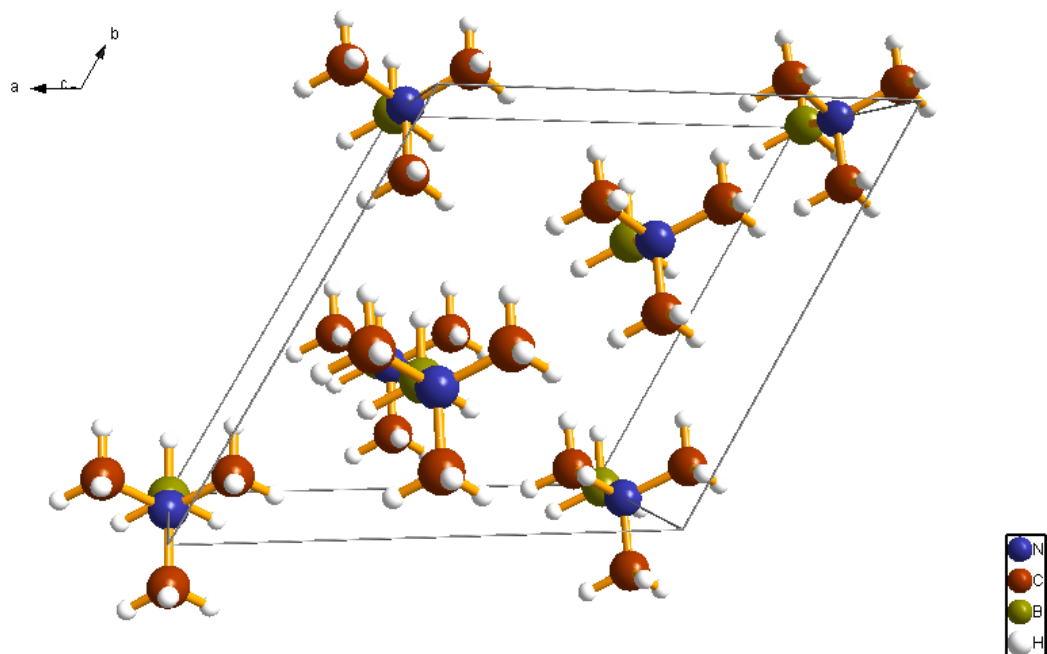


Figure 3.1 Ambient-pressure crystal structure of BTMA in space group $R3m$. The coordinate system is indicated to show the orientations of the unit cell.

In this study, using vibrational spectroscopy, we reported the first *in situ* high-pressure Raman and IR spectra of BTMA up to 30 GPa and 35 GPa in diamonds anvil cells (DACs), respectively. We observed interesting pressure-induced phase transitions in this pressure region. These findings not only further deepened our understanding of amine borane complexes, but also fulfilled our interest of having fullest knowledge and shed lights on research of hydrogen storage materials.

3.2 Experimental section

3.2.1 Sample preparation

White powders borane trimethylammonia (97% purity) were purchased from Alfa-Aesar and used without further purification.

A symmetrical DAC with two type-I diamonds with 400 μm culets was used for the high-pressure Raman measurements, while a pair of type-II diamonds with a culet size of 300 μm was used for the IR measurements. Sample loading was conducted in an MBraun LAB Master 130 glovebox filled with N_2 atmosphere (< 10 ppm O_2 and H_2O). To accommodate the hygroscopicity of the material, no fluid pressure-transmitting medium was used. A few ruby (Cr^{3+} doped $\alpha\text{-Al}_2\text{O}_3$) chips were carefully placed inside the gasket chamber before the sample loading as the pressure calibrant. The pressure was determined by using the R_1 ruby fluorescence line shift with an accuracy of ± 0.05 GPa under quasi-hydrostatic conditions.²⁰ For IR measurements, spectral quality KBr powders were also loaded into the DAC to dilute the sample. In the entire compression process, no significant pressure gradient or non-hydrostatic effect was indicated by ruby fluorescence spectra obtained on different ruby chips across the sample chamber.

3.2.2 High pressure Raman measurements

A customized Raman micro-spectroscopy system was used to collect the Raman spectra.

The instrumental set-up was discussed in Chapter 2 and specific experimental parameters are described as follows. A green laser with wavelength 532.10 nm was used as the excitation source. The laser was focused to $< 5 \mu\text{m}$ on the sample by a 20 \times Mitutoyo objective. A 1200 lines/mm grating was used to disperse the scattered light, achieving a 0.1 cm^{-1} resolution. To avoid the strong first-order Raman mode of diamond at 1334 cm^{-1} , the spectra were collected in ranges of 0-1300 cm^{-1} and 1350-3400 cm^{-1} in several collection windows. A collection time of 30 s was employed for each spectrum, and the average laser power on the sample was kept at ~ 30 mW. All Raman measurements were conducted at room temperature and pressures of up to ~ 30 GPa, and were reproduced several times.

3.2.3 High pressure IR measurements

A customized IR micro-spectroscopy system was used for all room-temperature IR absorption measurements and the detailed instrumentation has been described in Chapter 2. All the IR measurements were undertaken in absorption (or transmission) mode. A resolution of 4 cm^{-1} and 512 scans were applied for each spectrum measurement to achieve an excellent signal-to-noise ratio. The absorption of diamond anvils loaded with KBr but without any sample was used as reference spectrum, and was later divided as background from each sample spectrum to obtain the absorbance.

3.3 Results and discussion

3.3.1 Ambient-Pressure Raman and IR spectra

Firstly, Raman and IR spectra shown in Figure 3.2 were collected under ambient pressure.

Our measurements of BTMA were in excellent agreement with previous research by Durig.³⁰ The peak assignments of observed modes could be made based on Durig's work. The tentative assignment results of BTMA were listed in Table 3.1 in comparison with reference. In the Raman spectra, 4 lattice modes at 353, 442, 450 and 480 cm^{-1} in the lattice region, were labeled as 1, 2, 3 and 4, respectively (Figure 3.3a). Other assigned modes were labeled as $\nu_{\text{B-H def}}$, $\nu_{\text{N-H def}}$, $\nu_{\text{B-H str}}$, $\nu_{\text{B-N str}}$ and $\nu_{\text{N-H str}}$ (“str” is short for stretching and “def” stands for deformation) according to their mode origins.

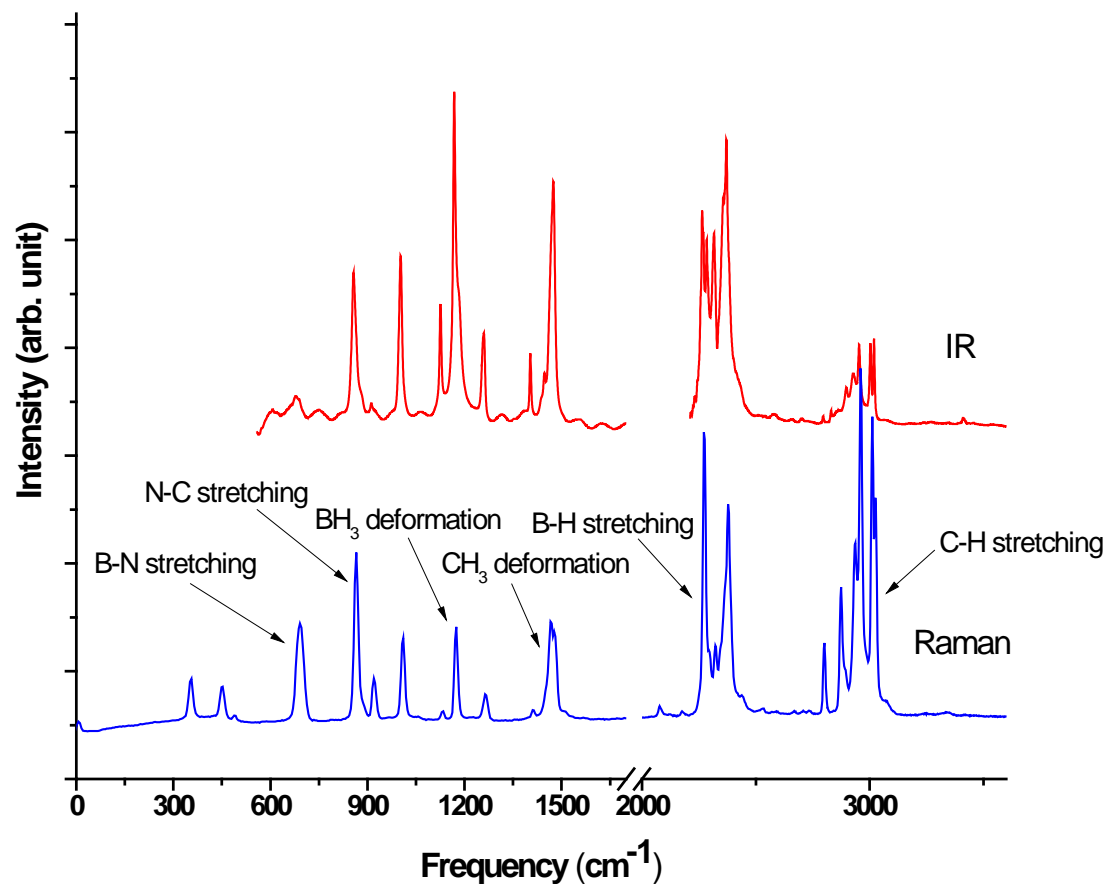


Figure 3.2 Raman spectrum of $N(CH_3)_3BH_3$ (bottom) in comparison with IR spectrum (top) in the spectral region $0-3800\text{ cm}^{-1}$, both collected at near ambient pressure and room temperature. The omitted spectral regions are due to the lack of spectroscopic features.

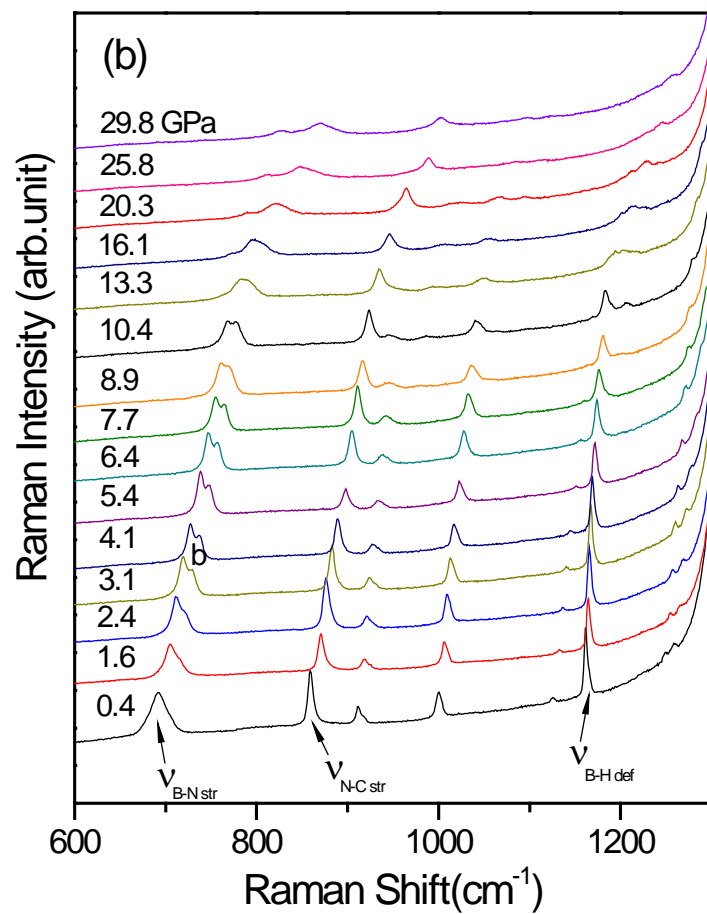
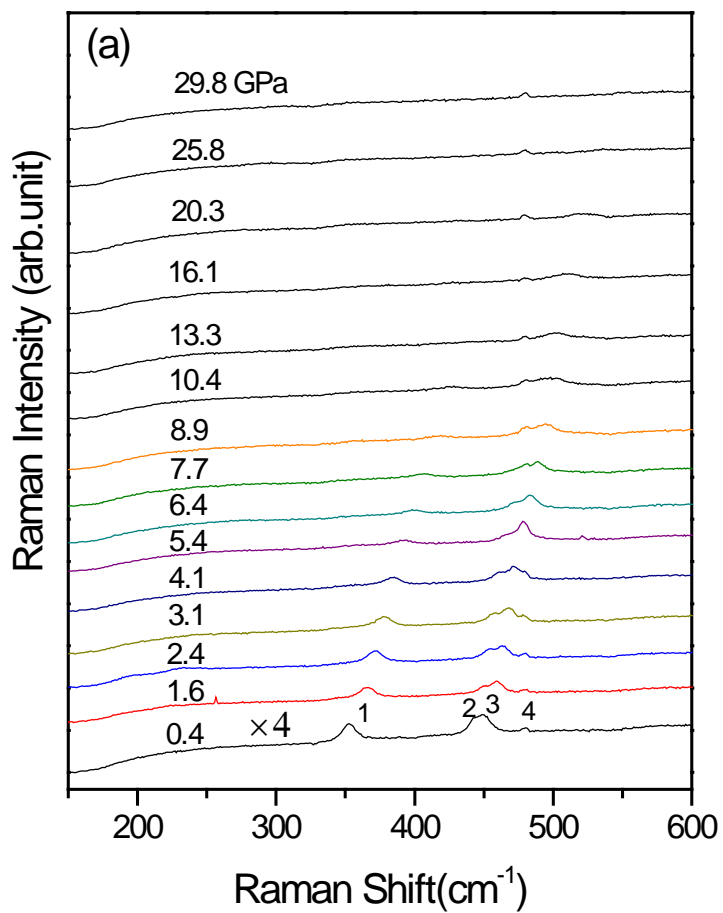
Table 3.1 Partial assignments and vibrational frequencies (cm⁻¹) of BTMA at ambient pressure

Description	BTMA		Reference ³⁰	
	Raman	IR	Raman	IR
asym. C-H stretching	3025	3019	3019	3018
	3013	3003	3004	3002
sym. C-H stretching	2961	2952	2953	2954
asym. B-H stretching	2377	2371	2373	2360
sym. B-H stretching	2270	2263	2266	2264
B-H deformation	1174	1168	1168	1168
C-H deformation	1468	1474	1475	1473
B-N stretching	691	-	680	680
N-C stretching	865	856	860	859

3.3.2 Raman spectra on compression

Starting from ambient pressure, Raman spectra of BTMA were collected up to 30 GPa with selected spectra depicted in Figure 3.3. In Figure 3.3 (a), lattice mode 3 became broad and intensified at around 3 GPa, which implies a phase transition. Meanwhile, in Figure 3.3 (b), the $\nu_{\text{B-N str}}$ at 718.5 cm^{-1} obviously split into two modes, where the new mode was labeled as $\nu_{\text{B-N str (b)}}$. The pressure evolution of other modes such as $\nu_{\text{N-C str}}$ were very gradual and lacked distinctive profile changes, with the exception of blue shifts in this pressure region. This new phase remained in the pressure region of 3.1-8.9 GPa as suggested by the similar Raman spectra.

Another round of phase transition could be identified when the pressure went beyond 8.9 GPa. First of all, all the lattice modes became extremely weak and broad at 8.9 GPa. In particular, lattice mode 1 almost disappeared. Moreover, the intensity of sharp $\nu_{\text{B-N str}}$ was significantly reduced. In Figure 3.3 (c), $\nu_{\text{B-H str (a)}}$ and $\nu_{\text{B-H str (b)}}$ remarkably faded away, and $\nu_{\text{B-H str (b)}}$ merged with the second order Raman mode of diamond at 2469.3 cm^{-1} . In Figure 3.3 (d), $\nu_{\text{C-H str (b)}}$ vanished at 8.9 GPa with the appearance of the shoulder peak of $\nu_{\text{asym C-H str(c)}}$ at 3062.3 cm^{-1} . This new peak was further resolved when the pressure increased up to 10.4 GPa. All of the profile changes mentioned above collectively suggested a new phase transition at around 9 GPa. Upon compression to 29.8 GPa, the highest pressure reached in our study, all the modes obviously weakened and broadened, indicating the appearance of amorphous phase. It is worth noting that no red shifts could be observed in the whole pressure region. That means the dihydrogen bonds observed in NH_3BH_3 ^{17,31} do not exist in $\text{N}(\text{CH}_3)_3\text{BH}_3$.



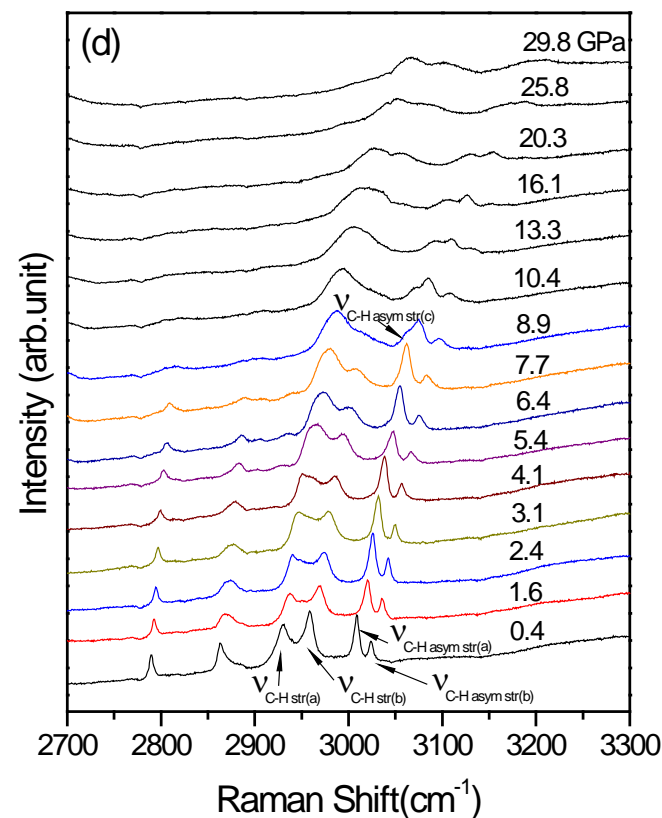
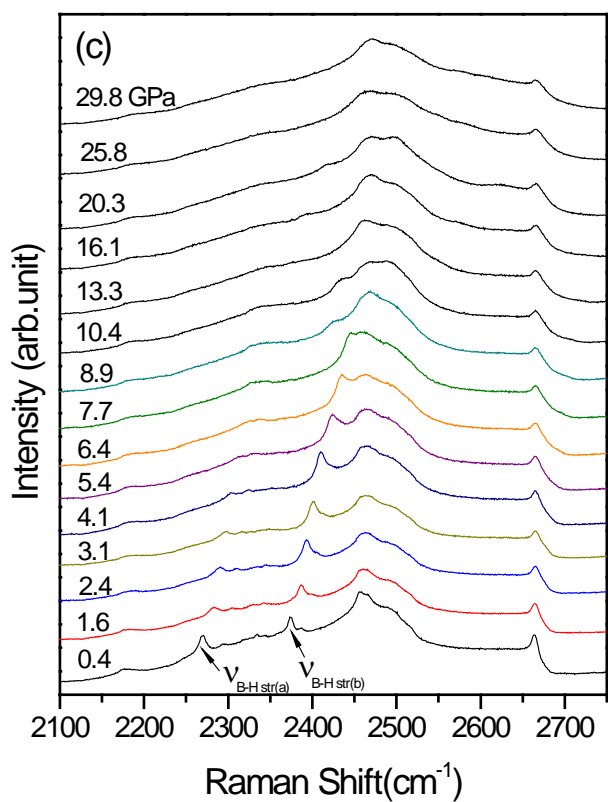


Figure 3.3 Selected Raman spectra of BTMA collected at room temperature on compression in the region of 0-600 cm^{-1} , the lattice region with enhanced intensity (A) 600-1300 cm^{-1} (B) 2100-2700 cm^{-1} (C) and 2700-3350 cm^{-1} (D) at pressures of 0.4-29.8 GPa. The relative intensities are normalized and thus are directly comparable. The pressures in GPa are labeled for each spectrum. The assignments are labeled for selected Raman modes (see text).

3.3.3 IR spectra on compression

The Mid-IR spectra of BTMA were collected from ambient pressure up to 35 GPa. Selected absorption spectra in the region of 600-3500 cm^{-1} are depicted in Figure 3.5. Similar to the Raman measurements, the first phase transition could be identified at 3.7 GPa, as indicated by rich changes in IR features. First, a former shoulder peak (1459.8 cm^{-1}) in C-H deformation region evolved into a sharp peak. In addition, $\nu_{\text{B-H str (b)}}$, split into two components. These clear profile changes were indicative of phase transition at this pressure point, and were consistent with the result obtained from Raman spectra.

When the pressure was further increased, all bands gradually became broadened and shifted to higher frequencies. The most drastic changes occurred at 9.4 GPa. At this pressure point, a new peak suddenly appeared at 1236.2 cm^{-1} as the shoulder peak of the $\nu_{\text{B-H def}}$. At the same time, the two components of $\nu_{\text{C-H def}}$ at 1247 cm^{-1} developed into a triplet. Moreover, the formation of a sharp peak at 2434.1 cm^{-1} right in front of the $\nu_{\text{asym B-H str}}$ could be easily noticed. All the changes mentioned above provided substantial evidences of phase transition at 9.4 GPa.

Beyond 9.4 GPa, all the modes continually broadened with reduced intensities. At 34.8 GPa, the peaks became extremely weak and broad. No further dramatic phase transitions occurred in the third pressure region, which suggested that the third phase observed in our high pressure study has a much wider stability region than the previous two. It is important to point out that, in agreement with the Raman spectra, all the IR modes exhibited blue shifts in the entire pressure region. Again, this phenomenon suggested the absence of dihydrogen bonding between $\text{N}(\text{CH}_3)_3\text{BH}_3$ molecules.

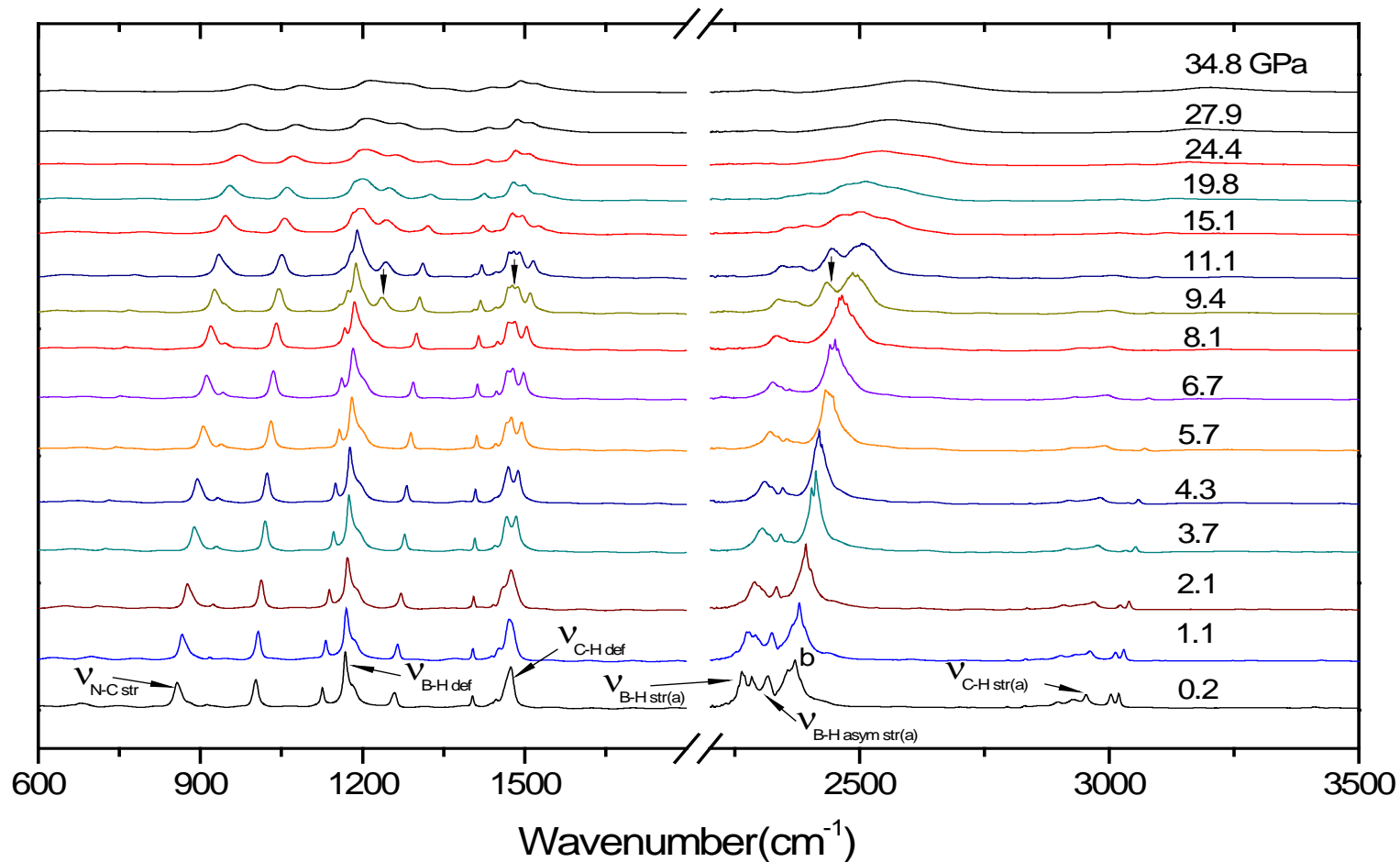


Figure 3.4 Selected IR spectra of BTMA collected at room temperature on compression in the spectral region of 600-3500 cm^{-1} in the pressure region of 0.2-34.8 GPa. The pressures in GPa are labeled for each spectrum respectively. The assignments are labeled for selected IR modes.

3.3.4 Pressure effects on Raman and IR modes

The suggested phase transitions in the Raman and IR spectra could be further visualized by plotting the characteristic modes as a function of pressure as depicted in Figures 3.5 and 3.6. Pressure coefficients for the assigned modes were calculated by the least-square fitting of the experimental data and are listed in Tables 3.2 and 3.3. The proposed phase boundaries can be further evidenced by the changes in pressure coefficients between different phases.

In the Raman spectra, a significant change in the slope could be observed between different phases. In general, the pressure coefficients in Phase I are relatively larger than those in the other two phases. Different pressure coefficients indicate different compressibilities of different phases. Moreover, all the pressure coefficients are positive, meaning all of the Raman modes displayed blue shifts in the entire pressure region due to bond stiffening upon compression.

The compression behavior of the IR modes of $\text{N}(\text{CH}_3)_3\text{BH}_3$ was similar to the Raman modes. The monitored IR modes shifted to higher frequencies in the entire pressure region. Nonetheless, the changes of pressure coefficients of the IR modes were less significant than those of the Raman modes. Overall, the pressure coefficients of the monitored Raman and IR modes collectively suggested 3 pressure regions: 0-3 GPa, 3-9 GPa and 9-35 GPa.

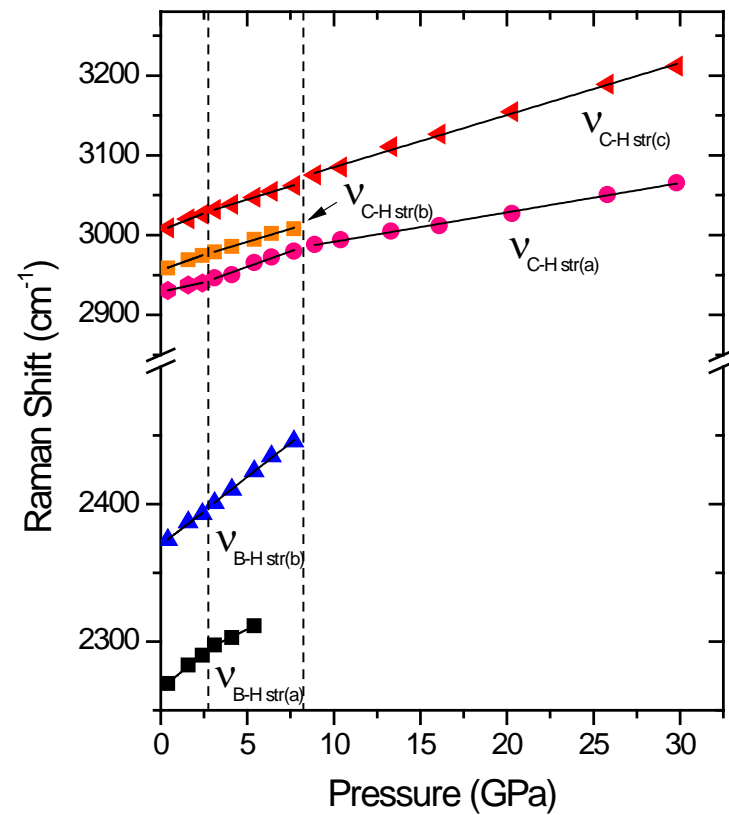
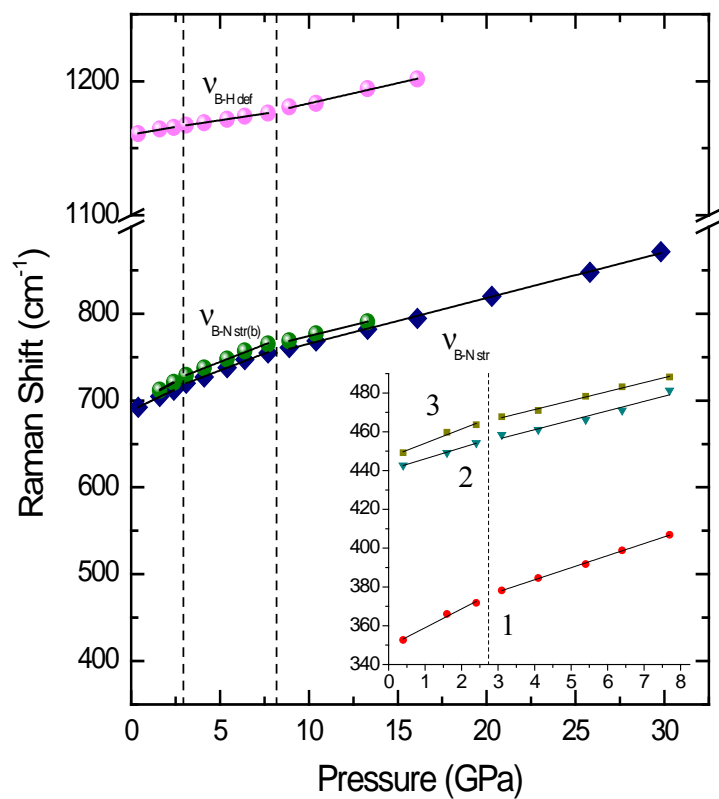


Figure 3.5 Pressure dependence of selected Raman modes of BTMA on compression. Different symbols represent Raman modes with different origins with assignments labeled (see text). The solid lines crossing the solid symbols are based on linear regressions. The vertical dashed lines indicate the proposed phase boundaries.

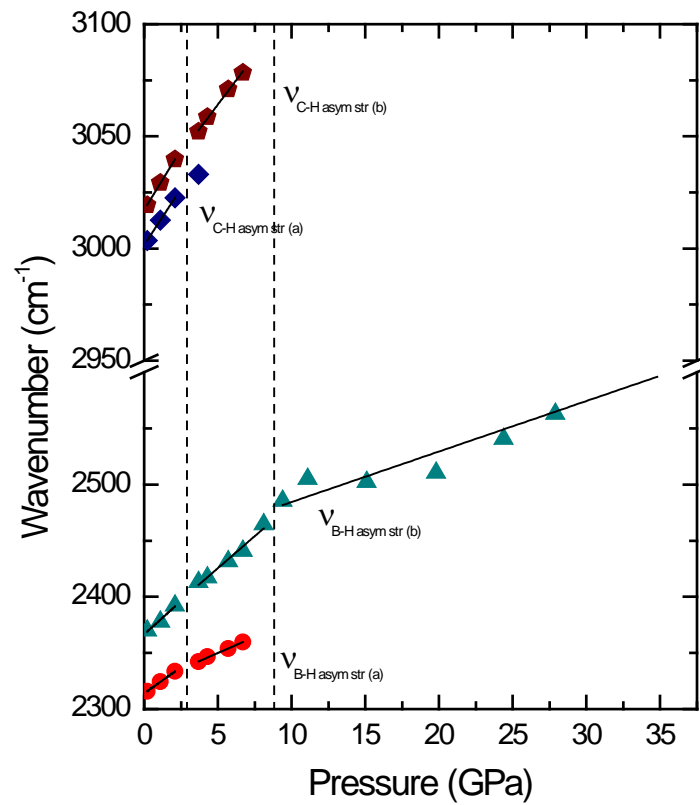
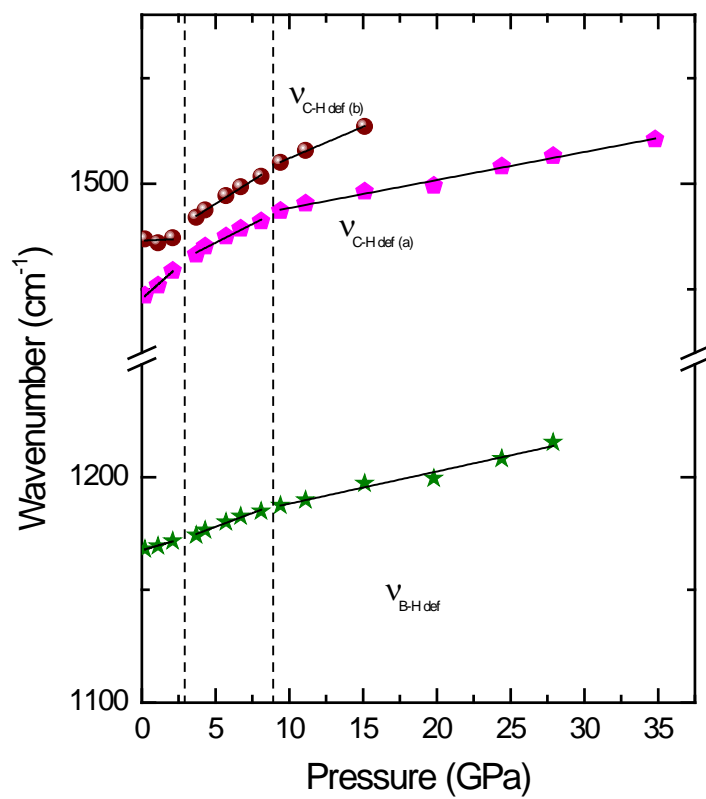


Figure 3.6 Pressure dependence of selected IR modes of BTMA on compression. Different symbols represent Raman modes with different origins with assignments labeled (see text). The solid lines crossing the solid symbols are based on linear regressions. The vertical dashed lines indicate the proposed phase boundaries.

Table 3.2 Pressure dependence of the selected Raman modes of BTMA on compression

Optical Mode	Frequency (cm ⁻¹)	dν/dP (cm ⁻¹ ·GPa ⁻¹)		
		Phase I (<3.1 GPa)	Phase II (3.1-8.9 GPa)	Phase III (>8.9 GPa)
V ₁	352.4	9.7	6.2	-
V ₂	442.2	5.7	4.9	-
V ₃	448.8	7.3	4.6	-
V B-N str	691.7	9.8	7.8	5.3
V B-N str (b)	729.2	11.2	8.0	5.0
V B-H def	1160.5	2.3	2.0	3.0
V B-H str (a)	2269.5	10.4	6.1	-
V B-H str (b)	2374.0	9.6	9.9	-
V C-H str (a)	2930.0	4.8	7.8	3.7
V C-H str (b)	2958.4	7.8	6.6	-
V C-H asym str (a)	3008.5	8.6	6.7	6.5

Table 3.3 Pressure dependence of the selected IR modes of BTMA on compression

Optical Mode	Frequency (cm ⁻¹)	dν/dP (cm ⁻¹ ·GPa ⁻¹)		
		Phase I (0-3.7 GPa)	Phase II (3.7-9.4 GPa)	Phase III (>9.4 GPa)
V B-H def	1168.6	1.9	2.4	1.4
V C-H def (a)	1446.5	6.2	3.5	1.3
V C-H def (b)	1474.3	0.3	4.4	3.0
V B-H asym str (a)	2315.8	9.3	5.8	-
V B-H asym str (b)	2370.8	11.8	11.4	4.5
V C-H asym str (a)	3003.8	10.0	-	-
V C-H asym str (b)	3019.6	10.8	8.7	-

3.3.5 Raman and IR spectra on decompression.

In order to study the reversibility of pressure-induced phase transitions, Raman and IR spectra were collected on decompression all the way down to near-ambient pressure. Selected spectra are shown in Figures 3.7 and 3.8. The Raman spectra of compressed

sample after pressure release were highly similar to the initial ones, with most of the peaks being recovered under ambient pressure. A small shift of the Raman modes compared to the initial modes could be attributed to hysteresis effect. Similarly, in the IR spectra, we could observe the complete back transformations. Again, the hysteresis effect and the difference of sample thickness in compression/decompression cycle possibly led to slight changes of positions and intensities in the IR modes.

According to the recovered Raman and IR spectra, we can conclude that the pressure-induced phase transitions are reversible.

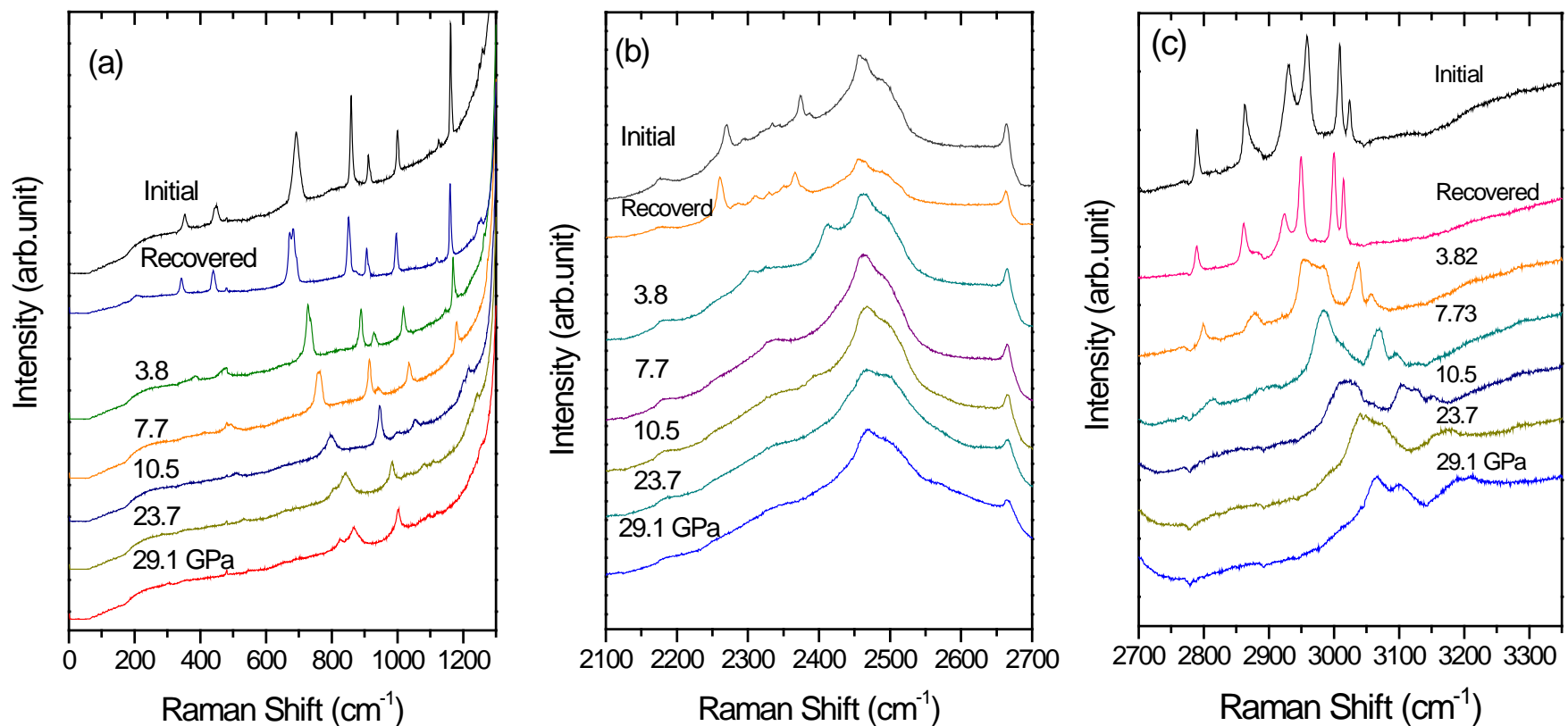


Figure 3.7 Selected Raman spectra of BTMA collected at room temperature on decompression in the spectral region of 0-1300 cm⁻¹ (A), 2100-2700 cm⁻¹ (B) and 2700-3350 cm⁻¹ (C). The pressures in GPa are labeled for each spectrum. The initial near-ambient-pressure spectra before compression (top) is included to compare with the spectra of recovered BTMA.

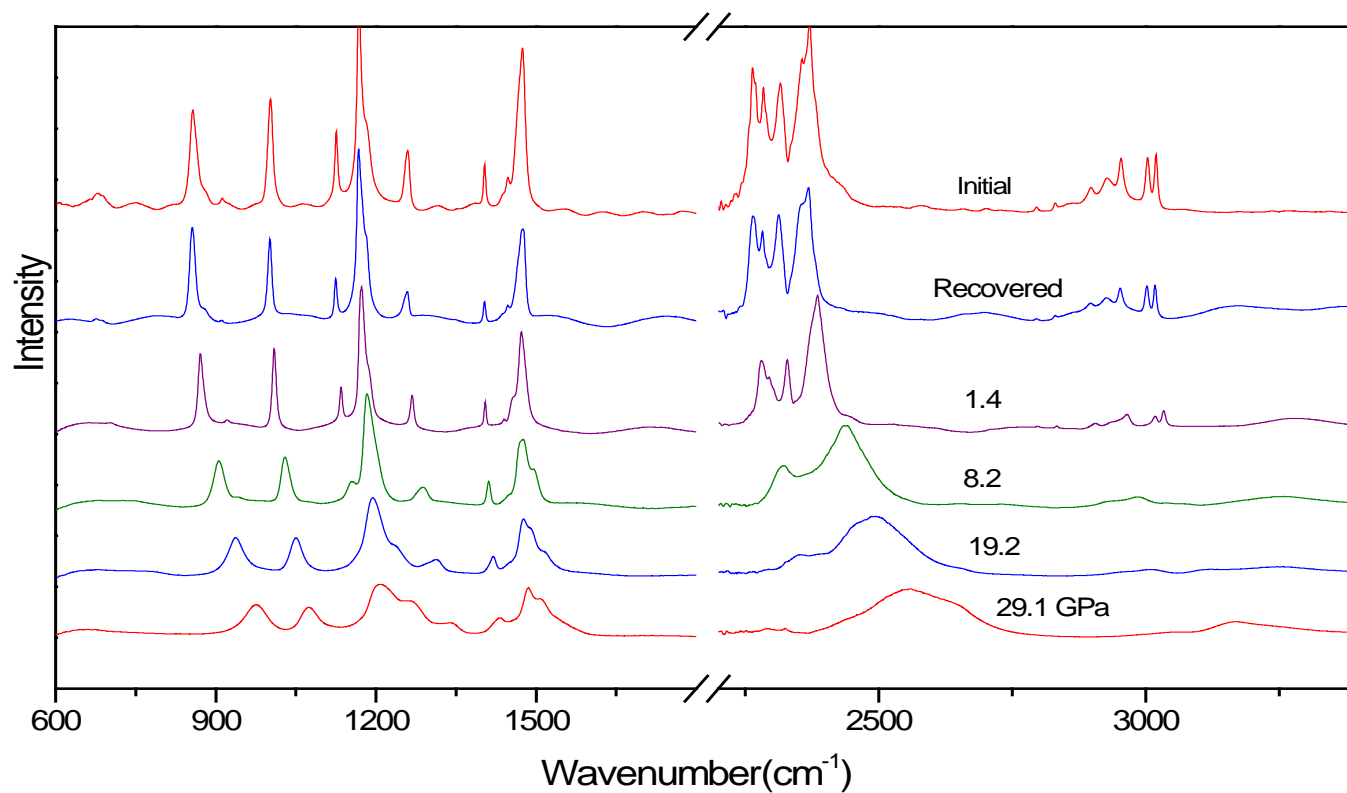


Figure 3.8 Selected IR spectra of BTMA collected at room temperature on decompression in the spectral region of 600-3400 cm^{-1} . The pressures in GPa are labeled for each spectrum. The assignments are labeled for selected IR modes (see text). The initial near-ambient-pressure spectra prior to compression (top) are included as a comparison with the spectra of recovered BTMA.

3.3.6 Discussion

Three pressure regions were successfully characterized by the aforementioned spectroscopic study. Naturally, the subsequent question will be what the possible high-pressure structures and the origins of phase transitions are. Unfortunately, as far as we know, no *in situ* high pressure X-ray diffraction has been reported. In our group's previous study of NH_3BH_3 , the factor group analysis was adopted to get a clue of the structural information. However, in this case of BTMA, factor group analysis seems unavailable to provide valuable information due to the structural complexity of BTMA. Therefore, a practical method is to carefully analyze the combined Raman and IR spectra, especially in the lattice region, which may reveal important information for understanding the high pressure structure of BTMA.

The lattice region of the IR spectra was lacking due to the Mid-IR setup in our lab while 4 lattice modes were identified in the Raman spectra. In the first pressure region (0.4-3.1 GPa), all the Raman and IR modes, especially the lattice modes, gradually shifted to higher frequencies without obvious changes. Therefore, phase I could be interpreted as the extension of rhombohedral crystals with space group $R\bar{3}m$ under ambient condition. Upon compression to the first phase boundary (3 GPa), the intensity of ν_3 was enhanced. Moreover, the splitting of Raman $\nu_{\text{B-N str}}$, IR $\nu_{\text{C-H def}}$ and $\nu_{\text{B-H str}}$ could be observed. All these changes strongly indicated enhanced intermolecular interactions or lower unit cell

symmetry. More detailed structural information is needed to reveal by *in situ* high-pressure X-ray diffraction.

In the next pressure region (3-9 GPa), BTMA experienced apparent structural modification. The lattice modes became further weakened. Moreover, ν_2 and ν_3 underwent enhanced separation. In the C-H stretching region, new modes were detected in both Raman and IR spectra. When the pressure went beyond 9 GPa, BTMA transformed into an amorphous phase via structural disorder which was evidenced by the gradual broadening and reduced intensities of Raman and IR modes, especially the depletion of lattice modes. In the previous high pressure studies of NH_3BH_3 , N-H stretching modes displayed negative shift correlation with pressure due to dihydrogen bonding. However, in the case of BTMA, the positive pressure-induced shifts of all modes from 0.4 to 35 GPa were in agreement with bond stiffening, which ruled out the possible existence of dihydrogen bonding between BTMA molecules. This is likely due to the total methyl substitution of the NH_3 group in $\text{N}(\text{CH}_3)_3\text{BH}_3$ and CH_3 is not capable of forming dihydrogen bonds with the BH_3 group.

3.4 Conclusion

By means of *in situ* Raman and IR spectroscopy, we investigated the pressure behavior of BTMA up to 30 and 35 GPa, respectively. Two phase transitions were characterized by abundant profile changes observed at around 3 and 9 GPa. After decompression, the

characteristic Raman and IR modes were recovered under ambient pressure, which indicated that the pressure-induced phase transitions were reversible. Raman and IR spectral analysis revealed that phase I maintained the parent structure-rhombohedral up to 3 GPa. Further compression may cause BTMA to experience structural transformation. High pressure X-ray diffraction and theoretical calculations are still needed to identify the detailed structural information under high pressure.

3.5 References

- (1) Hughes, C. C.; Scharn, D.; Mulzer, J.; Trauner, D. *Org. Lett.* **2002**, *4*, 4109.
- (2) Luo, J. H.; Kang, X. D.; Wang, P. *J. Phys. Chem. C* **2010**, *114*, 10606.
- (3) Peng, Y.; Ben, T.; Yang, D. J.; Zhao, H. J.; Qiu, S. L.; Yao, X. D. *J. Phys. Chem. C* **2012**, *116*, 25694.
- (4) Tang, Z.; Chen, X.; Chen, H.; Wu, L.; Yu, X. *Angew. Chem. Int. Ed.* **2013**, *52*, 5832.
- (5) Wright, W. R. H.; Berkeley, E. R.; Alden, L. R.; Baker, R. T.; Sneddon, L. G. *Chem. Commun.* **2011**, *47*, 3177.
- (6) Yoon, C. W.; Sneddon, L. G. *J. Am. Chem. Soc.* **2006**, *128*, 13992.
- (7) Sepehri, S.; Feaver, A.; Shaw, W. J.; Howard, C. J.; Zhang, Q.; Autrey, T.; Cao, G. *J. Phys. Chem. B* **2007**, *111*, 14285.
- (8) Himmelberger, D. W.; Yoon, C. W.; Bluhm, M. E.; Carroll, P. J.; Sneddon, L. G. *J. Am. Chem. Soc.* **2009**, *131*, 14101.
- (9) Paolone, A.; Teocoli, F.; Sanna, S.; Palumbo, O.; Autrey, T. *J. Phys. Chem. C* **2013**, *117*, 729.

- (10) Sams, R. L.; Xantheas, S. S.; Blake, T. A. *J. Phys. Chem. A* **2012**, *116*, 3124.
- (11) Satyapal, S.; Petrovic, J.; Read, C.; Thomas, G.; Ordaz, G. *Catal. Today* **2007**, *120*, 246.
- (12) Song, Y. *Phys. Chem. Chem. Phys.* **2013**, in press
- (13) George, L.; Drozd, V.; Saxena, S. K.; Bardaji, E. G.; Fichtner, M. *J. Phys. Chem. C* **2009**, *113*, 15087.
- (14) Liu, A.; Xie, S. T.; Dabiran-Zohoory, S.; Song, Y. *J. Phys. Chem. C* **2010**, *114*, 11635.
- (15) Liu, A.; Song, Y. *J. Phys. Chem. B* **2011**, *115*, 7.
- (16) Song, Y.; Murli, C.; Liu, Z. X. *J. Phys. Chem.* **2009**, *131*.
- (17) Liu, A.; Song, Y. *J. Phys. Chem. C* **2012**, *116*, 2123.
- (18) Moser, D.; Baldissin, G.; Bull, D. J.; Riley, D. J.; Morrison, I.; Ross, D. K.; Oates, W. A.; Noreus, D. *J. Phys-Condens Mat.* **2011**, *23*.
- (19) Bortz, M.; Bertheville, B.; Bottger, G.; Yvon, K. *J. Alloy Compd.* **1999**, *287*, L4.
- (20) Lin, Y.; Ma, H.; Matthews, C. W.; Kolb, B.; Sinogeikin, S.; Thonhauser, T.; Mao, W. L. *J. Phys. Chem. C* **2012**, *116*, 2172.
- (21) Chen, J. H.; Couvy, H.; Liu, H. Z.; Drozd, V.; Daemen, L. L.; Zhao, Y. S.; Kao, C. *Int. J. Hydrogen Energy* **2010**, *35*, 11064.
- (22) Filinchuk, Y.; Nevidomskyy, A. H.; Chernyshov, D.; Dmitriev, V. *Phys. Rev. B* **2009**, *79*.
- (23) Xie, S.; Song, Y.; Liu, Z. *Can. J. Chem.* **2009**, *87*, 1235.
- (24) Nixon, T. D.; Whittlesey, M. K.; Williams, J. M. J. *Tetrahedron Lett.* **2011**, *52*, 6652.
- (25) Hugel, T.; Hartl, M.; Lentz, D. *Chem.-Eur. J.* **2011**, *17*, 10184.
- (26) Dalton, D. A.; Somayazulu, M.; Goncharov, A. F.; Hemley, R. J. *J. Phys. Chem. A* **2011**, *115*, 11033.
- (27) Aldridge, S.; Downs, A. J.; Tang, C. Y.; Parsons, S.; Clarke, M. C.; Johnstone, R.

- D. L.; Robertson, H. E.; Rankin, D. W. H.; Wann, D. A. *J. Am. Chem. Soc.* **2009**, *131*, 2231.
- (28) Singh, P. C.; Patwari, G. N. *Chem. Phys. Lett.* **2006**, *419*, 5.
- (29) Patwari, G. N.; Ebata, T.; Mikami, N. *J. Phys. Chem. A* **2001**, *105*, 10753.
- (30) Odom, J. D.; Barnes, J. A.; Hudgens, B. A.; Durig, J. R. *J. Phys. Chem.* **1974**, *78*, 1503.
- (31) Kuppenko, I.; Dubrovinsky, L.; Dmitriev, V.; Dubrovinskaia, N. *J. Chem. Phys.* **2012**, *137*, 074506.

Chapter 4. *In-situ* high pressure study of dimethylamine borane by Raman and IR spectroscopy

4.1 Introduction

As potential hydrogen storage materials, amine-borane complexes received have extensive investigations in recent years due to the high gravimetric content of hydrogen in these compounds.¹⁻⁵ In particular, ammonia borane (NH_3BH_3), which contains 19.5 wt% H exceeding the target (9 wt%)⁶ set by the U.S. Department of Energy for on-board hydrogen storage systems is of interest to many researchers.^{3,7-10}

However, as discussed in Chapter 3, NH_3BH_3 has its intrinsic disadvantages. One of such problems is the high dehydrogenation temperature required for solid-state decomposition. Moreover, the borazine released in the decomposition process may be damaging to the fuel cell.¹ Consequently, in recent years, more and more research endeavors have been directed to ammonia borane derivatives.¹¹⁻¹⁷

Dimethylamine borane (DMAB), a derivative of NH_3BH_3 , is also regarded as a potential hydrogen storage material. There has been growing research focused on DMAB, including the investigation of dehydrogenation mechanisms and the search for suitable catalysts for releasing hydrogen from DMAB.¹⁸⁻²¹ However, compared to NH_3BH_3 which has been extensively investigated under high pressure, DMAB has not been studied in detail and as a

result, there is little known about its structures in a broad temperature or pressure range that is important for hydrogen storage applications.

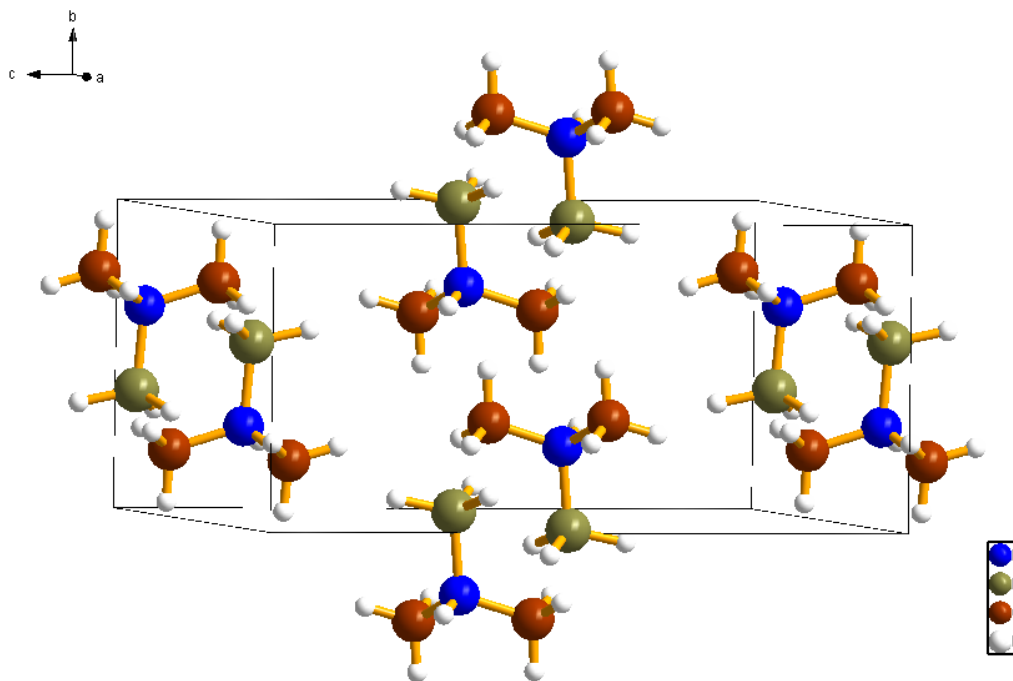


Figure 4.1. Ambient-pressure crystal structure of DMAB in space group $P2_1/c$. The coordinate system is indicated to show the orientations of the unit cell.

Under ambient conditions, DMAB crystallizes into a monoclinic cell with space group $P2_1/c$ (C_{2h}^5) and cell parameters $a=7.045$ Å, $b=5.837$ Å, $c=12.234$ Å and $Z=4$.²² The unit cell structure of DMAB is shown in Figure 4.1. Similar to NH_3BH_3 , DMAB displays obvious intermolecular $N-H\cdots H-B$ ‘dihydrogen bonds’ with short $H\cdots H$ distance (around 2 Å) which are labeled as B in Figure 4.2. Unlike the conventional hydrogen bonds, dihydrogen bonds are formed between $D-H^{\delta+}$ and $^{\delta-}H-E$, where $D-H$ is a typical proton donor such as an NH or OH group, and $E-H$ is either $B-H$ or $M-H$ (M =transition metal). With a strength around $3-7$ kcal·mol⁻¹, lying in the range of traditional hydrogen bonds,

such interactions can be observed in metal hydrides and boron hydrides.^{23,24}

As shown in Figure 4.2, molecules are linked in a head-to-tail manner via hydrogen bonding. Each chain is surrounded by neighboring chains experiencing interchain contacts.²²

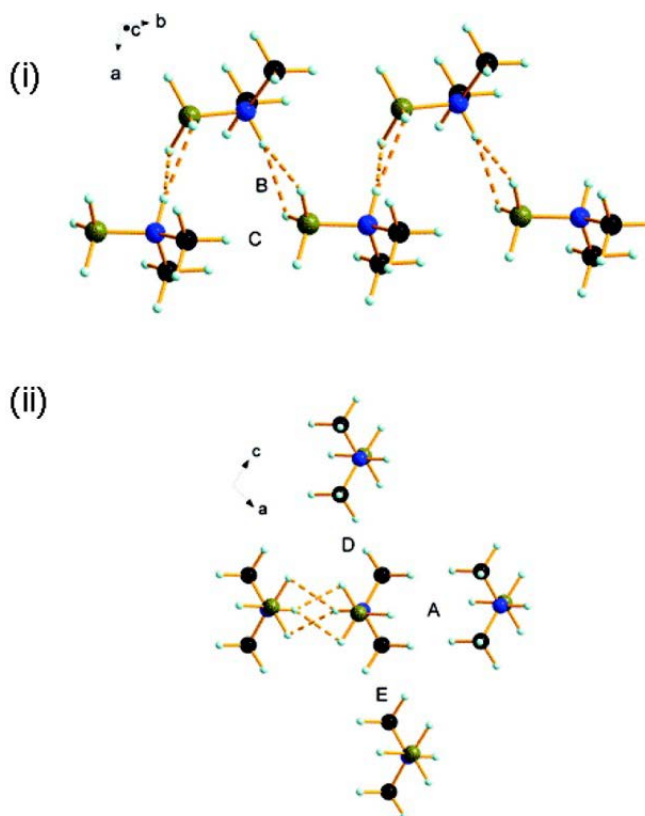


Figure 4.2. (i) Chains formed by H...H and electrostatic interactions in the crystal structure of DMAB. (ii) The most significant interchain interactions. (Adapted from Ref. 22)

In this study, we used vibrational spectroscopy to obtain the first *in situ* high-pressure Raman and IR spectra of DMAB up to 20 GPa in diamond anvil cells (DACs). Interesting pressure-induced phase transitions during the compression process were observed. These findings can contribute to the development of DMAB as hydrogen storage materials. In

addition, it may provide us a better understanding of the structure and related properties of ammonia borane derivatives in the high pressure region and shed further light on exploring improved ammonia borane based hydrogen storage materials.

4.2 Experimental section

4.2.1 Sample preparation

Dimethylammonia borane (97% purity) were purchased from Alfa-Aesar and used without further purification.

A symmetrical DAC with two type-I diamonds with 400 μm culets was used for the high-pressure Raman measurements, while a pair of type-II diamonds with a culet size of 300 μm was used for the IR measurements. Sample loading was conducted in a MBraun LAB Master 130 glovebox filled with N_2 atmosphere (< 10 ppm O_2 and H_2O). No fluid pressure-transmitting medium was used to accommodate the hygroscopicity of the material. A few ruby (Cr^{3+} doped $\alpha\text{-Al}_2\text{O}_3$) chips used as a the pressure calibrant were carefully placed inside the gasket chamber before the sample loading. The pressure was determined by using the R_1 ruby fluorescence line shift with an accuracy of ± 0.05 GPa under quasi-hydrostatic conditions.²⁰ For IR measurements, spectral quality KBr powders were also loaded into the DAC to dilute the sample. In the entire compression process, no significant pressure gradient or non-hydrostatic effect was indicated by ruby fluorescence spectra obtained on different ruby chips across the sample chamber.

4.2.2 High pressure Raman measurements

A customized Raman micro-spectroscopy system was used to collect the Raman spectra. The instrumental set up has been discussed in Chapter 2 and specific experimental parameters are described as follows. A green laser with wavelength 532.10 nm was used as the excitation source. The laser was focused to $< 5 \mu\text{m}$ on the sample by a 20 \times Mitutoyo objective. A 1200 lines/mm grating was used to disperse the scattered light, achieving a 0.1 cm^{-1} resolution. To avoid the strong first-order Raman mode of diamond at 1334 cm^{-1} , the spectra were collected in ranges of 0-1300 cm^{-1} and 1350-3400 cm^{-1} in several collection windows. A collection time of 30 s was employed for each spectrum, and the average laser power on the sample was kept at ~ 30 mW. All Raman measurements were conducted at room temperature and pressures of up to ~ 18 GPa, and were reproduced several times.

4.2.3 High pressure IR measurements

A customized IR micro-spectroscopy system was used for all room-temperature IR absorption measurements and the detailed instrumentations have been described in Chapter 2. All IR measurements were undertaken in absorption (or transmission) mode. A resolution of 4 cm^{-1} and 512 scans were applied for each spectrum measurement achieving an excellent signal-to-noise ratio. The absorption of diamond anvils loaded with KBr but without any sample was used as reference spectrum, and was later divided as background from each sample spectrum to obtain the absorbance.

4.3 Results and discussion

4.3.1 Ambient-Pressure Raman and IR spectra.

Raman and IR spectra of DMAB were collected under ambient pressure as a starting point and are shown in Figure 4.3 in comparison with the Raman spectrum of NH_3BH_3 . At ambient pressure and room temperature, DMAB crystallizes into a monoclinic phase with $P2_1/c$ space group with 4 molecules per unit cell. DMAB has a C_s molecular symmetry and a C_{2h}^5 factor group symmetry. The vibrational degrees of freedom for DMAB can be calculated as follows: $3n (Z^B) - 3 = 165$, where $n = 14$ and $Z^B = 4$. Factor group analysis indicates that there are 96 Raman active modes and 84 IR active modes in total, which are mutually exclusive. Obviously, the observed modes are just a subset of the total predicted modes. The use of a notch filter used in the Raman measurements, the spectral limit of $>400 \text{ cm}^{-1}$ imposed by our IR instrument capability and the incomplete factor group splitting may partly contribute to the absence of other modes.

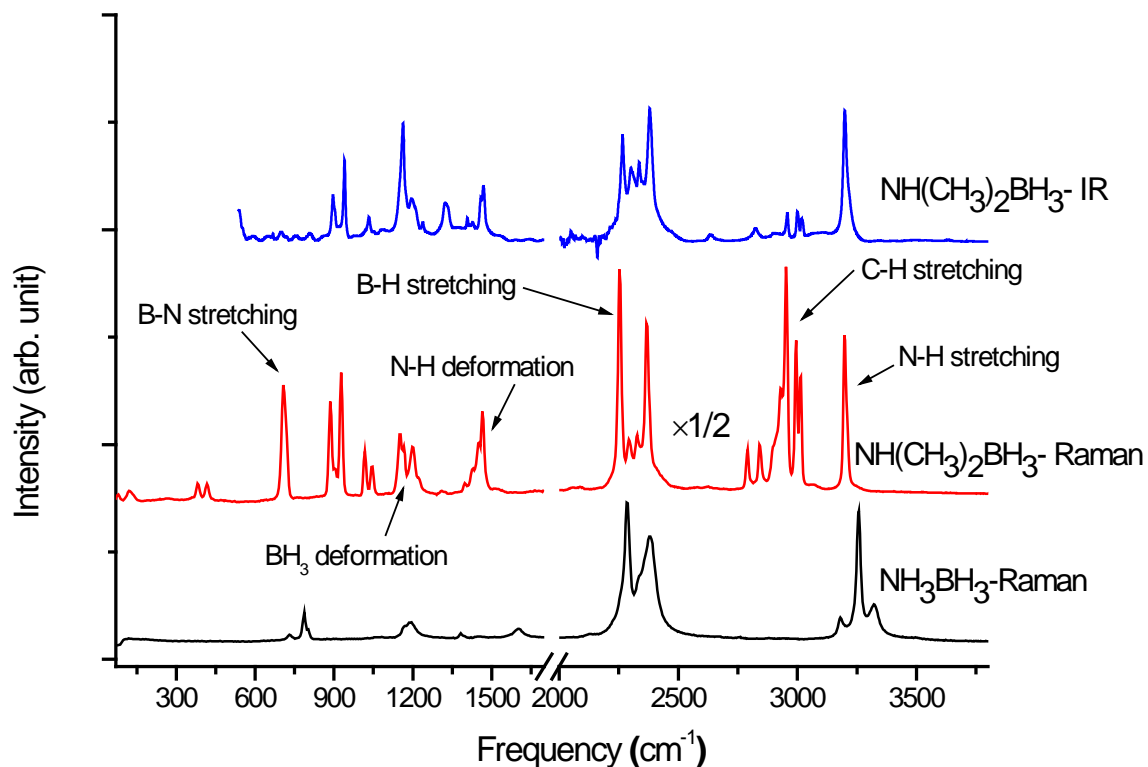


Figure 4.3. Raman (middle) and IR spectra (top) of DMAB in the spectral region 70-3800 cm^{-1} both collected at near ambient pressure and room temperature in comparison with Raman spectrum of NH_3BH_3 (bottom). The omitted spectral regions are due to the lack of spectroscopic features.

The peak assignments of DMAB have not yet been thoroughly investigated. However, in consideration of the structural similarity between DMAB and NH_3BH_3 , some important modes can still be assigned. The tentative assignment of selective Raman and IR modes of DMAB are listed in Table 4.1 in comparison with those of NH_3BH_3 . In the Raman spectra, we could observe 5 lattice modes at 69, 89, 136, 393, 426 cm^{-1} in the lattice region, which were labeled as 1, 2, 3, 4 and 5 respectively (Figure 4.4a) and other assigned modes were labeled as $\nu_{\text{B-H def}}$, $\nu_{\text{N-H def}}$, $\nu_{\text{B-H str}}$ and $\nu_{\text{N-H str}}$ (“str” is short for stretching and “def” stands for deformation) according to their mode origins.

From Table 4.1, we could conclude that the frequencies of B-H stretching modes are close to those of NH_3BH_3 while the frequencies of N-H stretching and deformation modes and B-N stretching modes are quite far away. This is possibly due to the methyl group substitution of the NH_3 group.

Table 4.1 Partial assignments and vibrational frequencies (cm^{-1}) of DMAB at ambient pressure

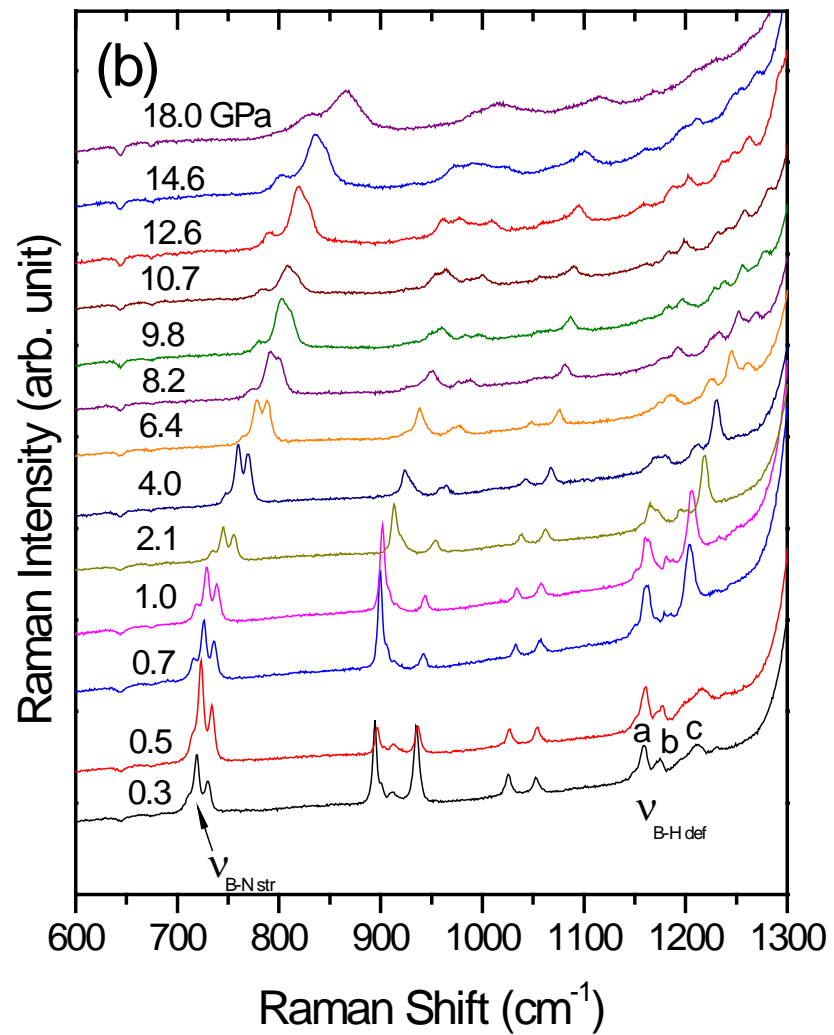
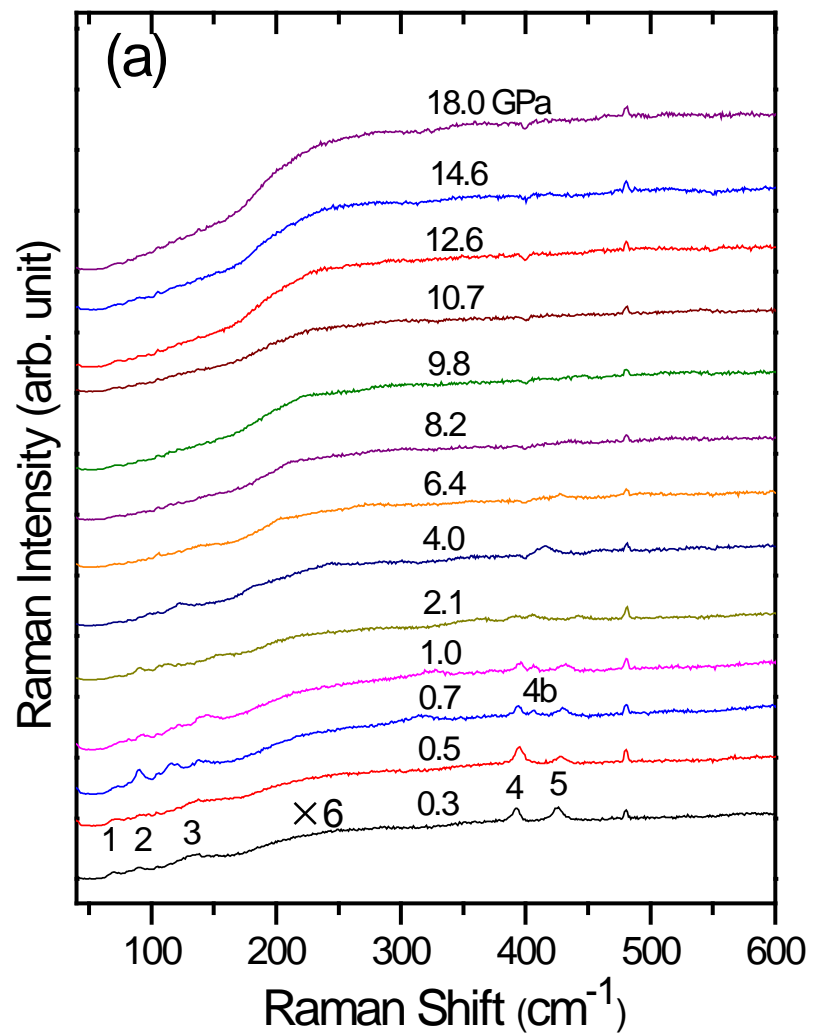
Description	DMAB		NH_3BH_3 ²⁵	
	Raman	IR	Raman	IR
asym. N-H stretch	3209	-	3316	3386
sym. N-H stretch	3198	3198	3250	3337
asym. B-H stretch	2376	2380	2328	2415
sym. B-H stretch	2260	2266	2279	2340
B-H deformation	1199	1197	1189	1186
	1151	1162	1155	1175
N-H deformation	1464	1468	1357	1343
B-N stretch	707	-	800	987
		-	784	968

4.3.2 Raman spectra on compression

Starting from ambient pressure, Raman spectra of DMAB were collected upon compression to 17.9 GPa with selected spectra depicted in Figure 4.4. In Figure 4.4 (a), the intensities of lattice modes 1, 2 and 3 were significantly enhanced when the sample was compressed to ~ 0.7 GPa. Concurrently, lattice mode 4 split into a doublet with the new peak labeled as 4b. The labels follow the convention that the new components are assigned in the order of their appearance (e.g., ν_a , ν_b , ν_c , etc.). All these obvious changes in the lattice region collectively suggested a phase transition together with a modification of the crystal

structure of DMAB. The phase transition can be further identified by the change in B-H deformation region in Figure 4.4 (b), where $\nu_{\text{B-H def (b)}}$ was clearly resolved. The similar Raman spectra from 0.7 to 9.8 GPa suggested the stability of the new phase in this pressure range. When the pressure went beyond 9.8 GPa, the peaks between 950-1000 cm^{-1} further split while all the lattice modes became barely visible. All these evidences were indicative of a new round of phase transition. As the pressure increased to 17.9 GPa, all the modes significantly broadened, being a strong indication of a transformation into an amorphous phase.

In Figure 4.4 (c), two peaks in the B-H stretching region were labeled as $\nu_{\text{B-H str (a)}}$ (2260 cm^{-1}) and $\nu_{\text{B-H str (b)}}$ (2376 cm^{-1}). The peak at 2458 cm^{-1} is the second order Raman mode of diamond. No obvious changes were observed in this region when the sample was compressed except for the broadening and blue shifts of the peaks. In Figure 4.4 (d), the evolution of $\nu_{\text{C-H str}}$ (2958 cm^{-1}) into two reduced components, and the merging of two peaks (2997 and 3001 cm^{-1}) in the C-H stretching region, indicated a phase transition at 0.7 GPa, which was consistent with the conclusion above. N-H stretching modes labeled as $\nu_{\text{N-H str (a)}}$ and $\nu_{\text{N-H str (b)}}$ displayed obvious red shifts upon compression, in accordance with the observation in the high pressure study of NH_3BH_3 .^{9, 25} This phenomenon could be explained by the weakening of the N-H bond and the strengthening of the dihydrogen bond $\text{N-H}\cdots\text{H-B}$ by compression.⁹ However, it is noteworthy that when the pressure was increased beyond 9.8 GPa, the trend reversed from red shift to blue shift. This kind of changing cycle was not observed in the study of NH_3BH_3 .



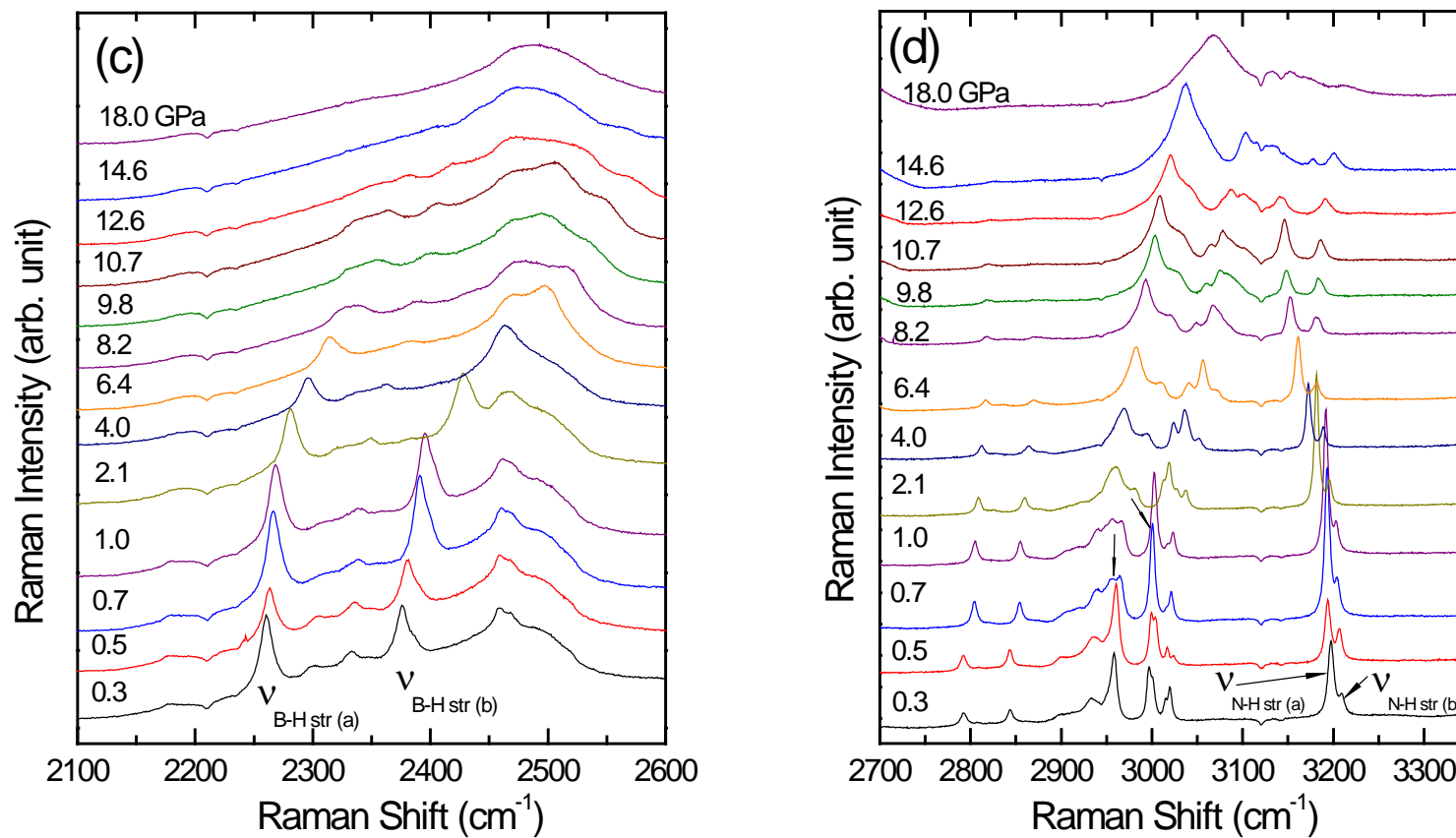


Figure 4.4 Selected Raman spectra of DMAB collected at room temperature on compression in the region of 40-600 cm⁻¹, lattice region with enhanced intensity (A), 600-1300 (B), 2100-2600 cm⁻¹ (C) and 2700-3350 cm⁻¹ (D) at pressures of 0.28-17.9 GPa. The relative intensities are normalized and thus are directly comparable. The pressures in GPa are labeled for each spectrum. The assignments are labeled for selected Raman modes (see text). The omitted spectral regions are due to the lack of spectroscopic features.

4.3.3 IR spectra on compression

Mid-IR spectra of DMAB were collected on compression at 20.5 GPa. Selected absorption spectra in the region of 650-3600 cm^{-1} are depicted in Figure 4.5. Upon compression to 0.8 GPa from ambient pressure, a phase transition can be clearly identified by various changes of IR modes. First, the split of $\nu_{\text{B-H def (a)}}$, in addition to the sharpness of the shoulder peak of $\nu_{\text{B-H def (a)}}$ at 1197 cm^{-1} provided substantial evidence. In the meantime, the N-H stretching mode $\nu_{\text{N-H str (a)}}$ evolved into two components. The most dramatic changes were observed in the B-H stretching region, where the two peaks $\nu_{\text{B-H str (b)}}$ and $\nu_{\text{B-H str (c)}}$ developed into four components with enhanced intensities. All these observations suggested a phase transition at ~ 0.8 GPa which agreed with the result we obtained in Raman spectra at similar pressure.

Beyond 9.7 GPa, all the modes gradually broadened and faded away. Most interestingly, the pressure dependence of the $\nu_{\text{N-H str (b)}}$ reversed at around 9.7 GPa and after that $\nu_{\text{N-H str (b)}}$ kept shifting to higher frequency till 20.5 GPa, the highest pressure reached in this study. This uncommon observation is consistent with what happened at around 9.8 GPa in the Raman spectra. All of these observations collectively indicated a new phase transition.

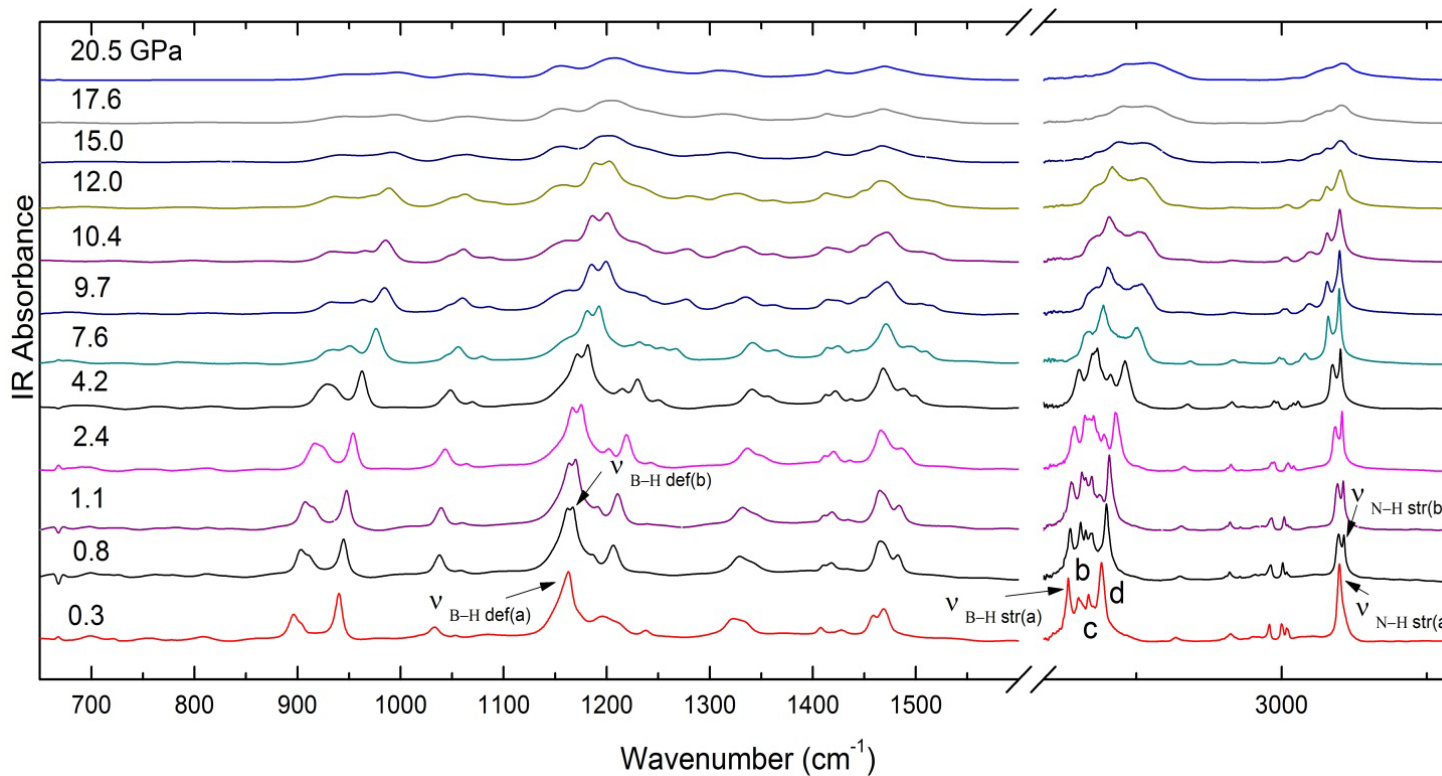


Figure 4.5 Selected IR spectra of DMAB collected at room temperature on compression in the spectral region of 650-3600 cm^{-1} in the pressure region of 0.3-20.5 GPa. The pressures in GPa are labeled for each spectrum respectively. The assignments are labeled for selected IR modes.

4.3.4 Pressure effects on Raman and IR modes

The possible phase transitions suggested by changes in the Raman and IR spectra were examined by plotting the characteristic modes as a function of pressure as depicted in Figure 4.6 and 4.7. Analyzed by least-square fitting of the experimental data, the calculated pressure coefficients for the assigned modes are listed in Table 4.2 and 4.3. Supplementary to the compelling spectroscopic evidence, the changes in pressure coefficients can further indicate the proposed phase boundaries.

In the Raman spectra, the pressure coefficient of the monitored modes displayed apparent changes between 0-0.7 GPa and 0.7-10.7 GPa. For instance, dv/dP of $\nu_{\text{B-H def (b)}}$ is $21.99 \text{ cm}^{-1}\cdot\text{GPa}^{-1}$ in the lower pressure region while it decreased significantly to $6.64 \text{ cm}^{-1}\cdot\text{GPa}^{-1}$ in the high pressure region. The smaller pressure dependence indicated lower compressibility of the new phase. The first red shift and subsequent blue shift of the N-H stretching modes could be clearly observed. In phase II, $\nu_{\text{N-H str (b)}}$ has a negative pressure coefficient of $-3.29 \text{ cm}^{-1}\cdot\text{GPa}^{-1}$. However, the pressure coefficient increased significantly to $3.60 \text{ cm}^{-1}\cdot\text{GPa}^{-1}$ in phase III.

Similar to the Raman spectra, in the IR spectra all the IR modes displayed blue shifts due to bond stiffening under compression with exception that the N-H stretching modes displayed red shifts in the pressure region of 0-9 GPa. The negative slopes (e.g., -2.15 and $-4.63 \text{ cm}^{-1}\cdot\text{GPa}^{-1}$ for $\nu_{\text{N-H str (a)}}$ and $\nu_{\text{N-H str (b)}}$) could be explained by a reason similar to that in the case of NH_3BH_3 . In contrast, the B-H stretching modes (e.g., $\nu_{\text{N-H str (a)}}$, $\nu_{\text{N-H str (b)}}$, $\nu_{\text{N-H str (c)}}$ and $\nu_{\text{N-H str (d)}}$ in IR spectra) exhibited blue shifts in all pressure regions (e.g., 15.03 and $3.68 \text{ cm}^{-1}\cdot\text{GPa}^{-1}$ in 0.8-10 GPa and 10-20 GPa respectively for $\nu_{\text{B-H str (d)}}$) denoting

remarkable strengthening of B-H bonding with decreased bond length. At around 9.8 GPa, the pressure coefficient of N-H stretching modes turned from negative to positive, strongly indicating that a phase transition took place at this pressure point. Moreover, the sharp changes in the pressure coefficient of $\nu_{\text{B-H str (d)}}$ (from 15.03 to 3.08 $\text{cm}^{-1}\cdot\text{GPa}^{-1}$) and the disappearance of $\nu_{\text{B-H str (a)}}$ and $\nu_{\text{B-H str (b)}}$ modes further identified the proposed phase boundary.

Overall, the pressure dependence of the assigned Raman and IR modes collectively suggested several pressure regions in which different phases exist. These pressure regions include: 0-0.7GPa, 0.7-10 GPa and > 10 GPa.

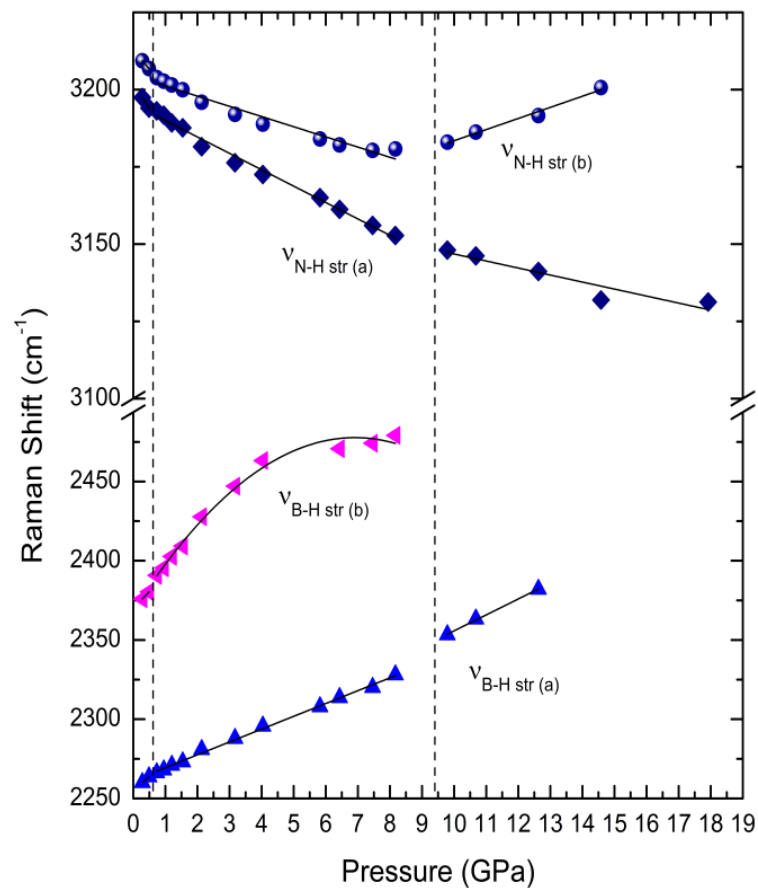
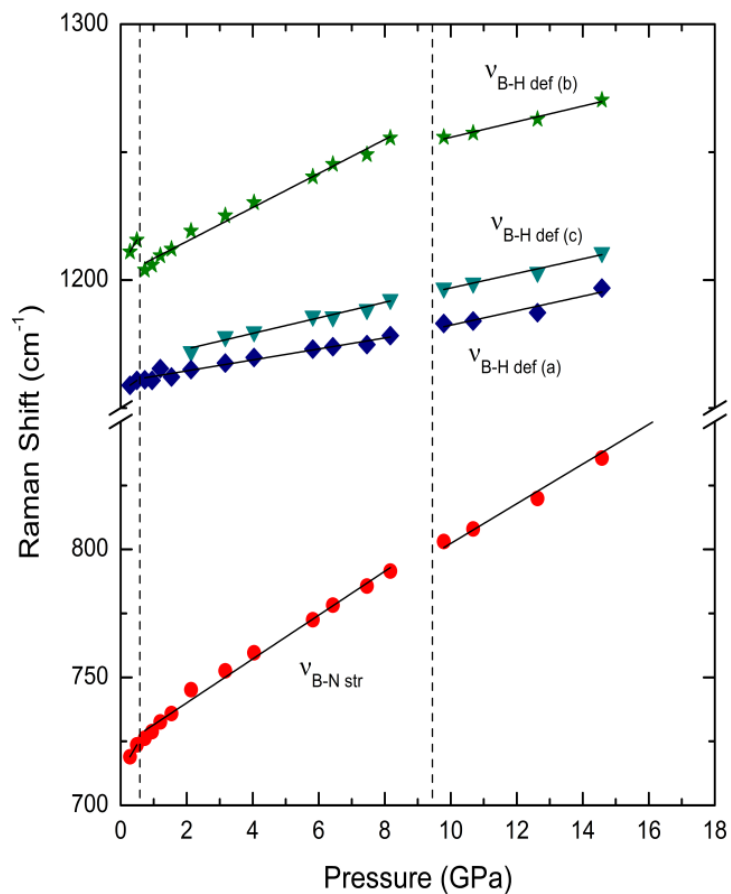


Figure 4.6 Pressure dependence of selected Raman modes of DMAB on compression. Different symbols represent Raman modes with different origins with assignments labeled (see text). The solid lines crossing the solid symbols are based on linear regressions except for $\nu_{\text{B-H def (b)}}$ mode in the pressure region of 0.7-10.0 GPa. The vertical dashed lines indicate the proposed phase boundaries.

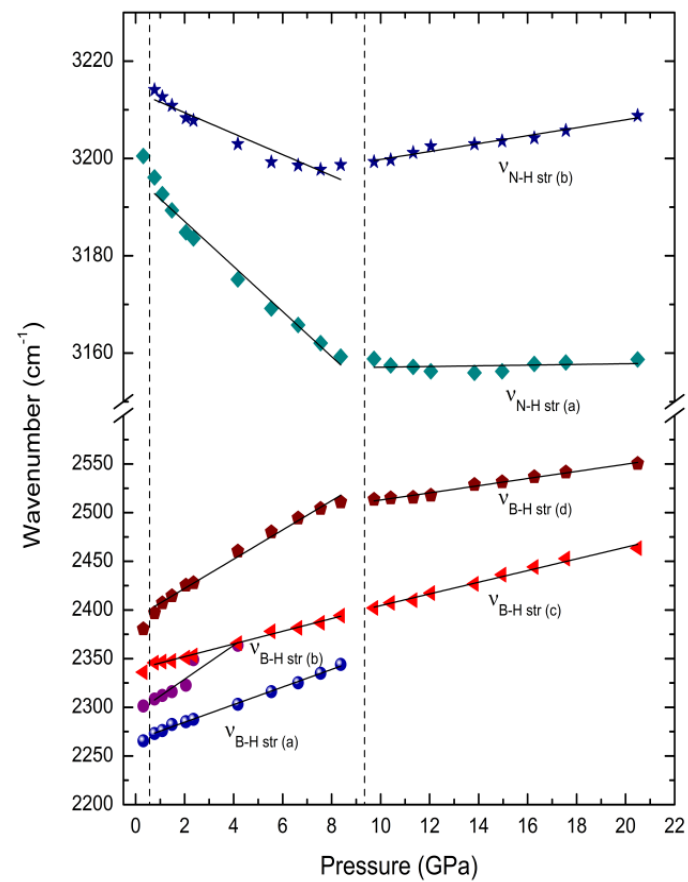
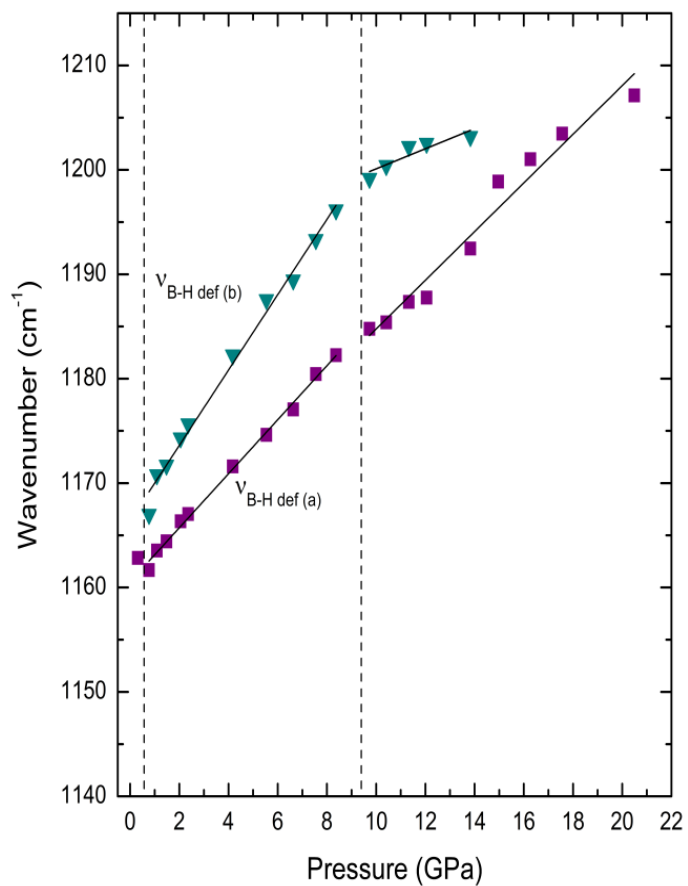


Figure 4.7 Pressure dependence of selected IR modes of DMAB on compression. Different symbols represent IR modes of different origins with assignments labeled (see text). The solid lines crossing the solid symbols are based on linear regressions except for $\nu_{\text{B-H def (c)}}$ mode. The vertical dashed lines indicate the proposed phase boundaries.

Table 4.2 Pressure dependence of the selected Raman modes of DMAB on compression

Optical Mode	Frequency (cm ⁻¹)	d ν /dP (cm ⁻¹ ·GPa ⁻¹)		
		Phase I (<0.8 GPa)	Phase II (0.8-10.0 GPa)	Phase III (>10.0 GPa)
V B-H def (a)	1158.9	9.1	2.1	2.8
V B-H def (b)	1211.2	22.0	6.6	3.0
V B-H def (c)	1172.3	-	3.0	2.8
V B-H str (a)	2260	17.2	8.1	10.0
V B-H str (b)	2375.9	20.9	11.6	-
V N-H str (a)	3197.5	-16.4	-5.3	-2.3
V N-H str (b)	3209.3	-11.8	-3.3	3.6
V B-N str	719	22.0	8.6	7.6

Table 4.3 Pressure dependence of the selected IR modes of DMAB on compression

Optical Mode	Frequency (cm ⁻¹)	d ν /dP (cm ⁻¹ ·GPa ⁻¹)		
		Phase I (<0.7 GPa)	Phase II (0.7-10.0 GPa)	Phase III (>10.0 GPa)
V B-H def (a)	1162.8	-	2.6	2.3
V B-H def (b)	1167	-	3.6	1.0
V B-H str (a)	2265.5	-	9.0	-
V B-H str (b)	2301.3	-	17.4	-
V B-H str (c)	2336	-	6.5	6.0
V B-H str (d)	2380.5	-	15.0	3.7
V N-H str (a)	3214.1	-	-2.1	0.8
V N-H str (b)	3200.5	-	-4.6	0.1

4.3.5 Raman and IR spectra on decompression

To get a better understanding of the reversibility of the pressure-induced phase transition

of DMAB, we conducted Raman and IR measurements on decompression with selected spectra shown in Figures 4.8 and 4.9. In the Raman spectra, the back transformations could be observed. Obviously, the recovered Raman modes were almost identical to the initial ones with only a little shift. Similar to the observations in the Raman spectra, when the near-ambient-pressure was reached, most of the IR peaks recovered except for some peaks in the B-H deformation and B-H stretching regions. The different shapes and intensities of the IR modes could likely be attributed to the difference of sample thickness in compression/decompression cycle and hysteresis effect. All the observations above collectively suggested that the pressure-induced phase transitions were reversible.

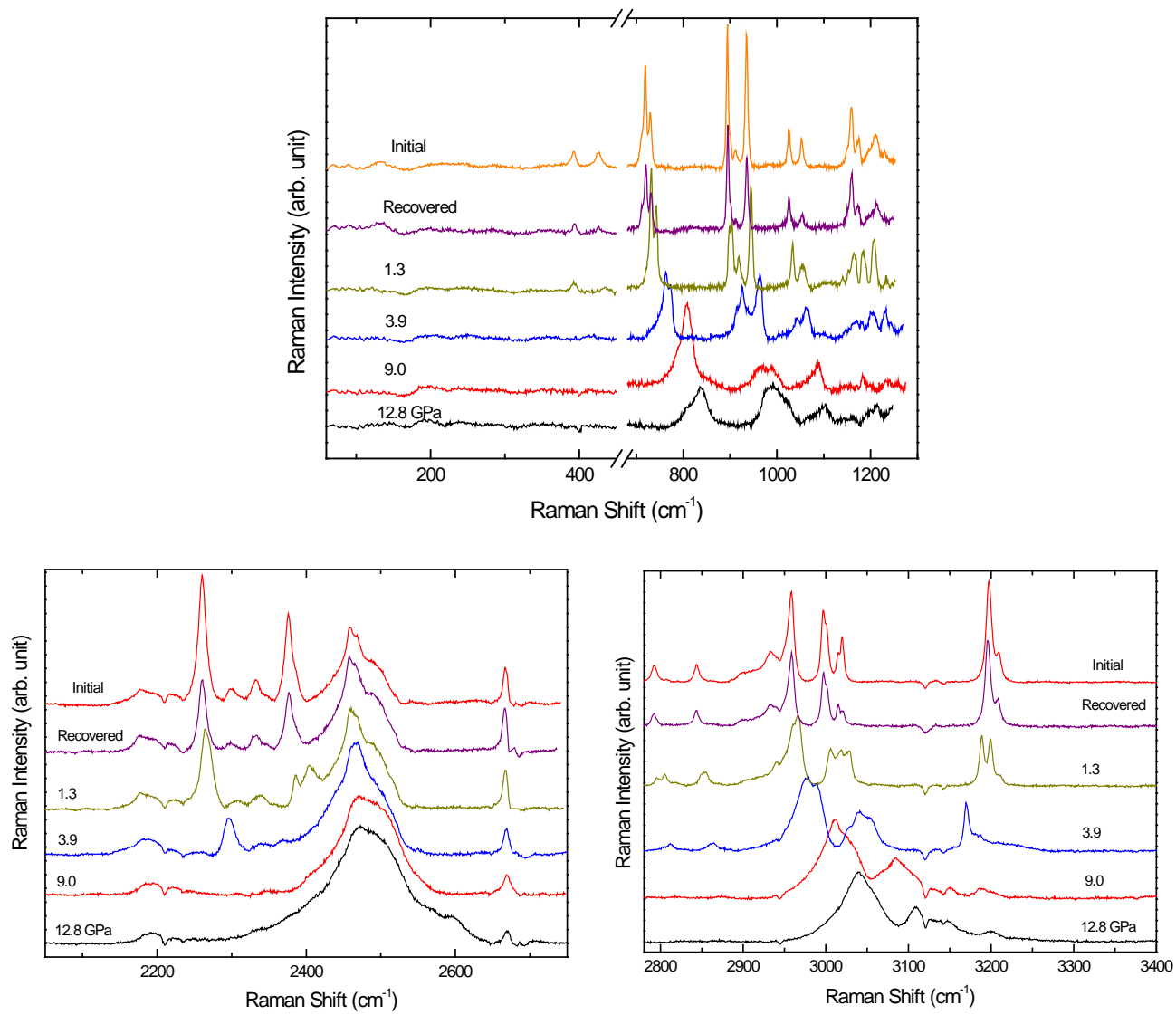


Figure 4.8 Selected Raman spectra of DMAB collected at room temperature on decompression in the spectral region of $10\text{-}1300\text{ cm}^{-1}$, $1600\text{-}2100\text{ cm}^{-1}$ and $2700\text{-}3400\text{ cm}^{-1}$. The pressures in GPa are labeled for each spectrum. The initial near-ambient-pressure spectra before compression (top) is included to compare with the spectra of recovered DMAB.

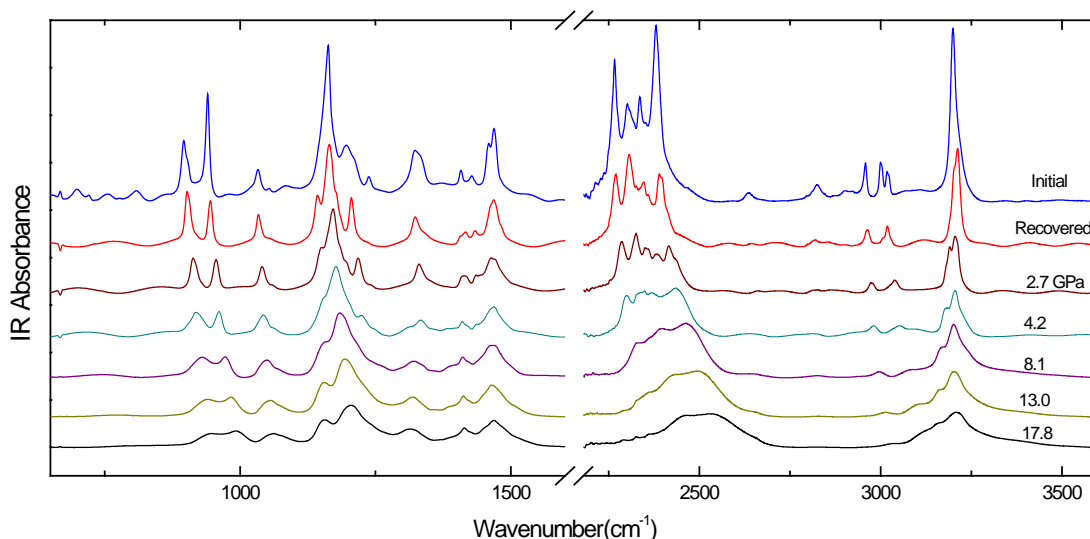


Figure 4.9 Selected IR spectra of DMAB collected at room temperature on decompression in the spectral region of $650\text{-}3600\text{ cm}^{-1}$. The pressures in GPa are labeled for each spectrum. The assignments are labeled for selected IR modes (see text). The initial near-ambient-pressure spectra prior to compression (top) are included as a comparison with the spectra of recovered DMAB.

4.3.6 Discussion

Two phase boundaries were suggested by our IR and Raman measurements at 0.7 and 10 GPa. It is of fundamental interest to investigate the corresponding structures and origins of phase transitions. Recently, Lin *et al.*²⁶ used a combination of synchrotron powder X-ray diffraction (XRD) and density functional theory (DFT) to study NH_3BH_3 under high pressure. In their study, the transformation from an $I4mm$ structure at ambient pressure to $\text{Cmc}2_1$ at 1.6 GPa was confirmed. The subsequent second-order isostructural phase transition at 5 GPa and further development into a monoclinic $\text{P}2_1$ phase at 12.9 GPa were also observed. To our knowledge, no *in situ* high-pressure X-ray diffraction study of DMAB has been reported so far. However, combining the spectroscopic measurements and

factor group analysis, we can still gain significant insight into the pressure behavior of DMAB.

As shown in Figure 4.1, the monoclinic structure ($P2_1/c$) with four molecular units per unit cell has the following lattice modes:

$$\Gamma_{\text{lattice vib.}}^{\text{DMAB}} = 6 A_g + 5 A_u \quad (4.1)$$

$$\Gamma_{\text{lattice lib.}}^{\text{DMAB}} = 6 A_g + 6 A_u \quad (4.2)$$

where Γ_{vib} and Γ_{lib} are irreducible representations for lattice vibration and lattice libration, respectively. A_g is Raman active while A_u is IR active. In all, 12 Raman active modes and 11 IR active modes are predicted. However, only 5 Raman lattice modes were detected in our experiment. The lack of other lattice modes is likely due to the notch filter used in our Raman system and Mid-IR setup, we were not able to thoroughly detect the signals under 100 cm^{-1} and 400 cm^{-1} , respectively. Although there is no contradiction between our observations and the predicted results, *in situ* high-pressure X-ray diffraction measurements are still needed to confirm the structure in the 0-0.7 GPa pressure region.

In the next pressure region (0.7-10 GPa), the Raman and IR spectra are quite different from those at low pressure. First, the Raman lattice modes shifted significantly with the appearance of a new mode at 407 cm^{-1} . In addition, the splitting of internal modes and apparent changes in pressure coefficients could be observed. All these observations strongly suggested a modification of the crystal lattice. Unfortunately, it is always the case that the observed Raman and IR modes are a subset of the predicted ones, which makes it extremely difficult to use factor group analysis to predict the possible structure. Again, *in situ* high-pressure X-ray diffraction measurements are needed to determine the crystal structure.

In the 10-20 GPa pressure region, the pressure coefficient of the N-H stretching modes changed from negative to positive, which is an evidence of phase transition. Lin *et al.*²⁶ suggested that the phase transition of NH_3BH_3 at 12.9 GPa was caused by the reorganization of the dihydrogen bonding network and the change in the rotational dynamics of the NH_3 and BH_3 groups. This reason could also be applied to explain the phase transition of its derivative-DMAB. The peaks in this region significantly broadened with reduced intensities. In particular, the lattice modes became extremely weak and almost indiscernible. All these phenomena collectively suggested that DMAB was turning into a possibly disordered or ultimately amorphous structure.

In order to gain a comprehensive understanding of structural and bonding properties of ammonia borane derivatives, the previous high pressure studies on methylamine-borane molecules were summarized in Table 4.4.^{25,26} In this table, it could be easily noticed that the pressure-induced phase transitions of ammonia borane and its derivatives were reversible. Dihydrogen bonding could be observed in ammonia borane^{25,27,31} and DMAB while it is absent in BTMA. This phenomenon can be attributed to the substitution of hydrogen with methyl group of hydrogen in the N-H group. The C-H group is not efficient as a proton donor as N-H group²⁹ and therefore the C-H \cdots H-B interaction was not formed. A careful analysis of Table 4.4 revealed that the first phase boundary of NH_3BH_3 and $\text{NH}(\text{CH}_3)_2\text{BH}_3$ is obviously lower than that of $\text{N}(\text{CH}_3)_3\text{BH}_3$. A possible explanation is that the dihydrogen bonding network is sensitive to the external pressure environment, which gives rise to the changes of orientation and rotational dynamics of NH and BH groups and hence phase transitions. Further experimental and theoretical investigations are needed to justify our interpretation.

Table 4.4 Summary of the high pressure studies on methylamine-borane molecules, $\text{Me}_n\text{H}_{3-n}\text{N}\cdot\text{BH}_3$

Material	Characterization method	Pressure range (GPa)	Phase transition pressure (GPa)	Dihydrogen bonding	Reversibility
NH_3BH_3	Raman/IR/XRD	0-20	1.5, 5, 12.9	Yes	Yes
$\text{NH}(\text{CH}_3)_2\text{BH}_3$	Raman/IR	0-20	0.7, 10	Yes	Yes
$\text{N}(\text{CH}_3)_3\text{BH}_3$	Raman/IR	0-35	3, 9	No	Yes

4.4 Conclusion

Taking advantage of *in situ* Raman and IR spectroscopy, we studied the pressure behavior of DMAB under high pressure up to 18 and 20 GPa respectively. DMAB was found to experience phase transitions at around 0.7 and 10 GPa from the parent phase $P2_1/c$. The phase transitions were evidenced by changes in spectral profiles and pressure dependence of fundamental optical modes. Spectroscopic measurements during decompression revealed the reversibility of pressure-induced phase transitions based on the observations that most of fundamental modes recovered under near-ambient pressure. Analysis of combined Raman and IR spectroscopy suggested that DMAB maintains a monoclinic structure with $P2_1/c$ space group under 0.8 GPa. Under further compression, DMAB underwent a structural transformation characterized by obvious changes in spectra, especially the appearance of new modes in the lattice region in the Raman spectra. At around 10 GPa, DMAB may undergo another phase transition that was supported by the changes of pressure dependence coefficient of the N-H stretching modes from negative to positive. We believed that the phase transition is due to the reorganization of the dihydrogen bonding network and the change in the rotational dynamics of the NH_3 and BH_3 groups. Further experiments such as *in situ* X-ray diffraction measurements and theoretical calculations are needed to confirm our interpretation.

4.5 References

- (1) Sewell, L. J.; Huertos, M. A.; Dickinson, M. E.; Weller, A. S.; Lloyd-Jones, G. C. *Inorg. Chem.* **2013**, *52*, 4509.
- (2) Najiba, S.; Chen, J. *Proc. Natl. Acad. Sci. U.S. A.* **2012**, *109*, 19140.
- (3) Peng, Y.; Ben, T.; Yang, D.; Zhao, H.; Qiu, S.; Yao, X. *J. Phys. Chem. C* **2012**, *116*, 25694.
- (4) Leardini, F.; Ares, J. R.; Bodega, J.; Valero-Pedraza, M. J.; Banares, M. A.; Fernandez, J. F.; Sanchez, C. *J. Phys. Chem. C* **2012**, *116*, 24430.
- (5) Luo, J.; Wu, H.; Zhou, W.; Kang, X.; Wang, P. *Int. J. Hydrogen Energy* **2013**, *38*, 197.
- (6) Satyapal, S.; Petrovic, J.; Read, C.; Thomas, G.; Ordaz, G. *Catal. Today* **2007**, *120*, 246.
- (7) Tang, Z.; Chen, X.; Chen, H.; Wu, L.; Yu, X. *Angew. Chem. Int. Ed.* **2013**, *52*, 5832.
- (8) Fernandes, R.; Patel, N.; Paris, A.; Calliari, L.; Miotello, A. *Int. J. Hydrogen Energy* **2013**, *38*, 3313.
- (9) Paolone, A.; Teocoli, F.; Sanna, S.; Palumbo, O.; Autrey, T. *J. Phys. Chem. C* **2013**, *117*, 729.
- (10) Srinivas, G.; Travis, W.; Ford, J.; Wu, H.; Guo, Z.-X.; Yildirim, T. *J. Mater. Chem. A* **2013**, *1*, 4167.
- (11) Sewell, L. J.; Huertos, M. A.; Dickinson, M. E.; Weller, A. S.; Lloyd-Jones, G. C. *Inorg. Chem.* **2013**, *52*, 4509.
- (12) Caliskan, S.; Zahmakiran, M.; Durap, F.; Ozkar, S. *Dalton Trans.* **2012**, *41*, 4976.

- (13) Tang, C. Y.; Phillips, N.; Bates, J. I.; Thompson, A. L.; Gutmann, M. J.; Aldridge, S. *Chem. Commun.* **2012**, *48*, 8096.
- (14) Sandra, F. P. R.; Demirci, U. B.; Chiriac, R.; Moury, R.; Miele, P. *Int. J. Hydrogen Energy* **2011**, *36*, 7423.
- (15) Luo, J.; Wu, H.; Zhou, W.; Kang, X.; Wang, P. *Int. J. Hydrogen Energy* **2013**, *38*, 197.
- (16) Najiba, S.; Chen, J. *Proc. Natl. Acad. Sci. U.S. A.* **2012**, *109*, 19140.
- (17) Xia, G.; Tan, Y.; Chen, X.; Guo, Z.; Liu, H.; Yu, X. *J. Mater. Chem. A* **2013**, *1*, 1810.
- (18) Nixon, T. D.; Whittlesey, M. K.; Williams, J. M. J., *Tetrahedron Lett.* **2011**, *52* (49), 6652.
- (19) Beweries, T.; Hansen, S.; Kessler, M.; Klahn, M.; Rosenthal, U., *Dalton Trans.* **2011**, *40* (30), 7689.
- (20) Tang, C. Y.; Phillips, N.; Bates, J. I.; Thompson, A. L.; Gutmann, M. J.; Aldridge, S., *Chem. Commun.* **2012**, *48* (65), 8096.
- (21) Sloan, M. E.; Staubitz, A.; Clark, T. J.; Russell, C. A.; Lloyd-Jones, G. C.; Manners, I., *J. Am. Chem. Soc.* **2010**, *132* (11), 3831.
- (22) Aldridge, S.; Downs, A. J.; Tang, C. Y.; Parsons, S.; Clarke, M. C.; Johnstone, R. D. L.; Robertson, H. E.; Rankin, D. W. H.; Wann, D. A., *J. Am. Chem. Soc.* **2009**, *131* (6), 2231.
- (23) Morrison, C. A.; Siddick, M. M. *Angew. Chem. Int. Ed.* **2004**, *43*, 4780.
- (24) Crabtree, R. H.; Siegbahn, P. E. M.; Eisenstein, O.; Rheingold, A. L. *Accounts.Chem. Res.* **1996**, *29*, 348.
- (25) Xie, S. T.; Song, Y.; Liu, Z. X., *Can. J. Chem.* **2009**, *87* (9), 1235.

- (26) Lin, Y.; Ma, H.; Matthews, C. W.; Kolb, B.; Sinogeikin, S.; Thonhauser, T.; Mao, W. L. *J. Phys. Chem. C* **2012**, *116*, 2172.
- (27) Kuppenko, I.; Dubrovinsky, L.; Dmitriev, V.; Dubrovinskaia, N. *J. Chem. Phys.* **2012**, 137.
- (28) Wang, L.; Bao, K.; Meng, X.; Wang, X.; Jiang, T.; Cui, T.; Liu, B.; Zou, G. *J. Chem. Phys.* **2011**, 134.
- (29) Crabtree, R. H.; Siegbahn, P. E. M.; Eisenstein, O.; Rheingold, A. L. *Accounts Chem. Res.* **1996**, *29*, 348.

Chapter 5. Ball milling synthesis and *in-situ* high pressure study of sodium amidoborane

5.1 Introduction

As previously described, ammonia borane (NH_3BH_3) is considered to be one of the most promising candidates for effective hydrogen storage.¹⁻⁵ NH_3BH_3 has many unparalleled advantages such as high hydrogen content (19.6 wt%) and chemical stability. However, its practical application is still limited by two intrinsic drawbacks, namely the high decomposition temperature and the release of toxic borazine in the decomposition process.^{6,7}

Recently, considerable effort has been devoted to lowering the dehydrogenation temperature, to inhibit borazine release and to enhance hydrogen release rate.⁸⁻¹⁴ For example, chemical compositional modification, in which one of the protonic hydrogen atoms of N-H in NH_3BH_3 is replaced by an alkali element such as Li and Na,¹⁵⁻²² is found to be effective. The rationale behind this strategy is to change the polarity and intermolecular interactions (especially the dihydrogen bonding) and thus to improve the dehydrogenation property.¹⁵ As a successful example, NaNH_2BH_3 releases ~7.4 wt% hydrogen at around 91 °C, significantly lower than the onset dehydrogenation temperature of NH_3BH_3 at 108 °C.²³ Moreover, no toxic borazine is detected during the decomposition process.^{15,20}

NaNH_2BH_3 (NaAB) crystallizes in the orthorhombic space group *Pbca*. The lattice

constants for NaNH_2BH_3 are $a = 7.46931(7) \text{ \AA}$, $b = 14.65483(16) \text{ \AA}$, $c = 5.65280(8) \text{ \AA}$, $V = 618.764(20) \text{ \AA}^3$.¹⁵ $[\text{NH}_2\text{BH}_3]^\delta$ groups form tetrahedral coordination with the Na^+ cation center with a Na-N distance of 2.35 \AA .^{16,24} The crystal structure of NaAB is shown in Figure 5.1.

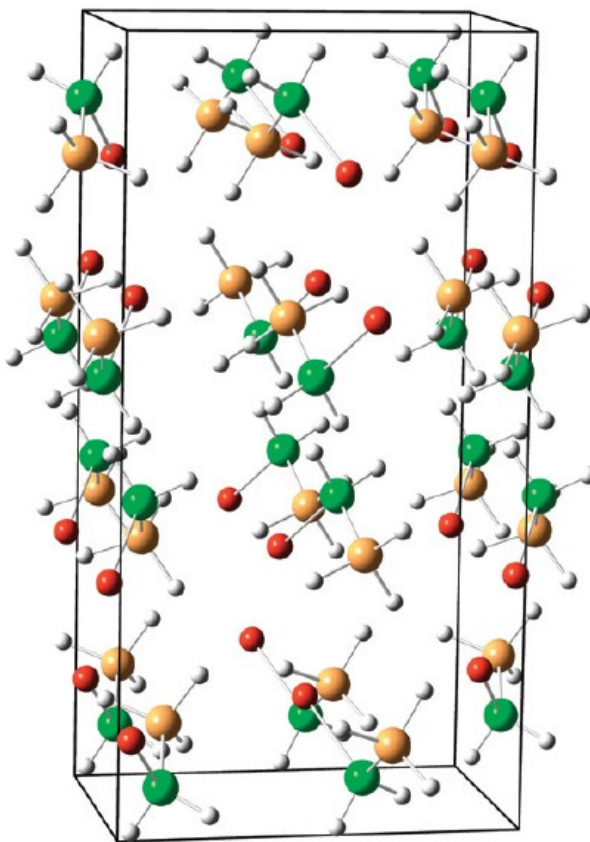


Figure 5.1. Ambient-pressure crystal structure of NaAB in space group *Pbca* determined from high-resolution X-ray power diffraction data at room temperature. Boron is represented by orange spheres, nitrogen by green spheres, hydrogen by white sphere and sodium by red spheres. This figure was adapted from reference 15,

NaAB can be synthesized via two approaches, namely traditional wet-chemistry synthesis²⁰ and solid-state mechanical milling.^{15,25} The procedure of wet-chemistry synthesis is slightly complicated since special treatment is needed to remove solvent from

the amidoborane product due to strong coordination between cations and solvent molecules. In contrast, the mechanical synthesis of NaAB is rather time-saving and straightforward without any worry about solvent removal. For this reason, the ball milling synthesis was adopted in our study. In a typical ball milling synthetic approach, ammonia borane and sodium hydride are used as reacting reagents. The driving force for this reaction is believed to be the high chemical potential of the combination of $H^{\delta+}$ in NH_3 and $H^{\delta-}$ in NaH to form H_2 .¹⁵

High pressure study of hydrogen storage materials can reveal unique structural information such as phase stability, hydrogen bonding, and even produce new structures with possible enhanced performance for hydrogen storage, which in turn provides guidelines for future design and improvement.²⁶⁻³¹ For instance, NH_3BH_3 has been intensively studied under high pressure conditions by Raman,^{30,31} IR spectroscopy,^{32,33} X-ray diffraction³⁴ and neutron diffraction.³⁵ More recently, a high pressure study of $LiNH_2BH_3$ using Raman spectroscopy was conducted by Najiba³⁶ and two phase transitions were identified.

In this study, using vibrational spectroscopy, we present the first *in situ* high-pressure Raman and IR spectra of NaAB up to 14 GPa in diamond anvil cells (DACs). NaAB showed interesting pressure-induced phase transitions in this pressure region. These findings will provide deeper a understanding of the properties of NaAB in a broad pressure region as well as ideas for future hydrogen storage development.

5.2 Experimental section

5.2.1 Sample synthesis

NaH (95% purity) and NH_3BH_3 (97% purity) were purchased from Sigma Aldrich and used without further purification. Ammonia borane and sodium hydride were mixed together with 1:1 molar ratio. The mixtures, as well as 6 steel milling balls (ball-to-sample weight ratio is 180 : 1), were transferred into the containers and the containers were sealed. All the operations above were conducted in a N_2 -filled MBraun LAB Master 130 glovebox with hydrogen and water content of < 10 ppm. The containers were then placed on a Retsch PM200 planetary mill and rotated for 60 minutes with a milling speed of 250 r.p.m. The reaction is shown below:



The prepared product was then characterized using an Inel CPS X-ray powder diffractometer with the $\text{Cu K}\alpha$ radiation. The obtained X-ray pattern was compared with that in Ref. 25 and they were found to be identical.

5.2.2 Sample preparation

A symmetrical DAC with two type-I diamonds with 400 μm culets was used for the high-pressure Raman measurements, while a pair of type-II diamonds with a culet size of 300 μm was used for the IR measurements. The sample loading was conducted in an

MBraun LAB Master 130 glovebox filled with N₂ atmosphere (< 10 ppm O₂ and H₂O). No fluid pressure-transmitting medium was used to accommodate the hygroscopicity of the material. A few ruby (Cr³⁺ doped α -Al₂O₃) chips as the pressure calibrant were carefully placed inside the gasket chamber before the sample loading. The pressure was determined by using the R₁ ruby fluorescence line shift with an accuracy of ± 0.05 GPa under quasi-hydrostatic conditions.²⁰ For IR measurements, spectral quality KBr powders were also loaded into the DAC to dilute the sample. In the entire compression process, no significant pressure gradient or non-hydrostatic effect was indicated by ruby fluorescence spectra obtained on different ruby chips across the sample chamber.

5.2.3 High pressure Raman measurements

A customized Raman micro-spectroscopy system was used to collect the Raman spectra. Detailed information regarding the instrumental set up can be found in Chapter 2 and specific experimental parameters are described as follows. The laser with 532.10 nm wavelength was focused on the sample by a 20 \times Mitutoyo objective to act as the excitation source. 0.1 cm⁻¹ resolution was achieved by using a 1200 lines/mm grating to disperse the scattered light. To avoid the strong first-order Raman mode of diamond at 1334 cm⁻¹, the spectra were collected in ranges of 50-1330 cm⁻¹ and 1350-3400 cm⁻¹ in several collection windows. A collection time of 30 s was employed for each spectrum, and the average laser power on the sample was kept at ~ 30 mW. All Raman measurements were conducted at

room temperature and pressures of up to ~ 14 GPa and were reproduced several times.

5.2.4 High pressure IR measurements

A customized IR micro-spectroscopy system was used for all room-temperature IR absorption measurements and the detailed instrumentations have been described in Chapter 2. All the IR measurements were undertaken in absorption (or transmission) mode. A resolution of 4 cm^{-1} and 512 scans were applied for each spectrum measurement achieving an excellent signal-to-noise ratio. The absorption of diamond anvils loaded with KBr but without any sample was used as reference spectrum, and was later divided as background from each sample spectrum to obtain the absorbance.

5.3 Results and discussion

5.3.1 Ambient pressure Raman and IR spectra

The Raman and IR spectra of NaNH_2BH_3 were collected at ambient conditions and are shown in Figure 5.2. The peak assignments of NaAB have not yet been thoroughly studied. However, in reference to the peak assignments of NH_3BH_3 and LiNH_2BH_3 , some important modes can still be assigned.^{33,36} The tentative assignment results are listed in Table 5.1 in comparison with those of NH_3BH_3 . In the Raman spectra, 5 lattice modes at 123, 148, 201, 227, 282 cm^{-1} in the lattice region were labeled as 1, 2, 3, 4 and 5 respectively (Figure 5.3a) and other assigned modes were labeled by their molecular nature: $\nu_{\text{B-H def}}$, $\nu_{\text{N-H def}}$, $\nu_{\text{B-H str}}$ and

$\nu_{\text{N-H str}}$ (“str” is short for stretching and “def” stands for deformation).

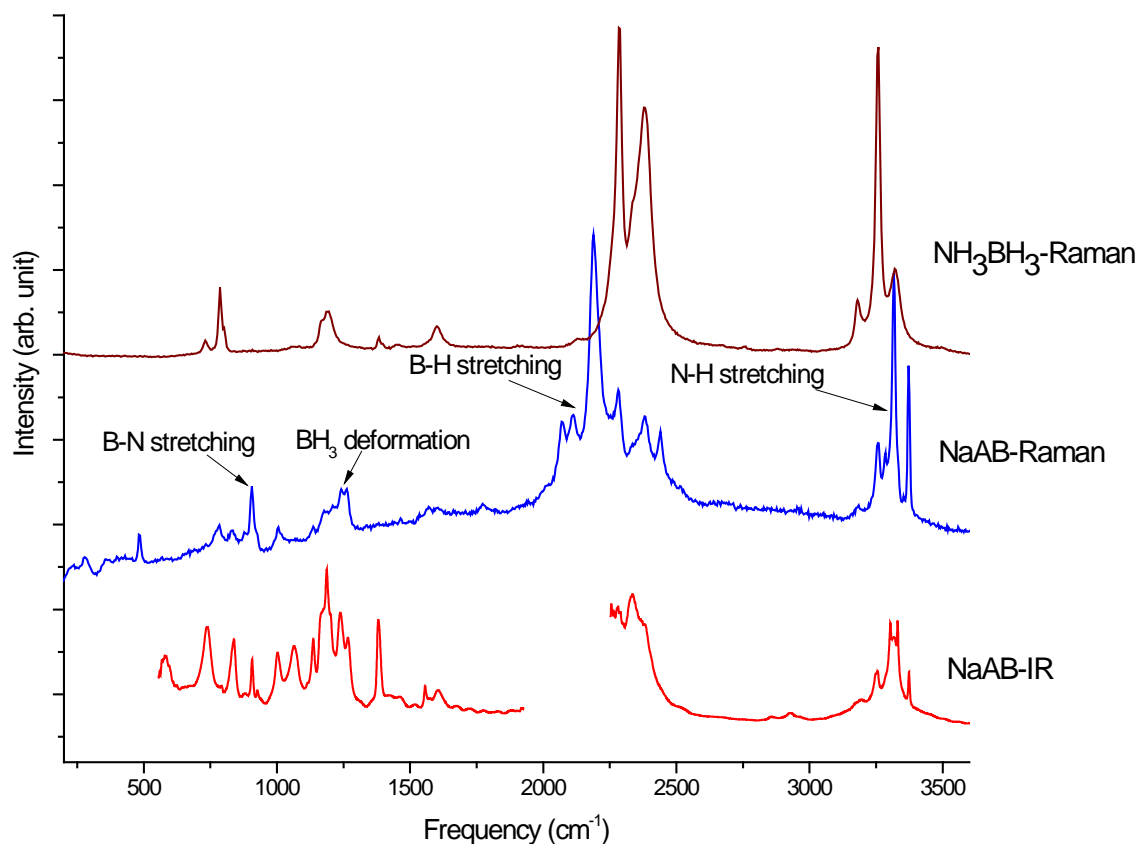


Figure 5.2 Raman (middle) and IR spectra (bottom) of NaAB in the spectral region 70-3600 cm^{-1} in comparison with the Raman spectrum of NH_3BH_3 (top). The omitted spectral region in the middle of IR spectra of NaAB is due to the strong absorbance of diamond.

In Table 5.1, compared with NH_3BH_3 , the B-H stretching mode appeared at lower wavenumber, which is in agreement with the previous study of LiNH_2BH_3 .³⁶ This change indicated NaAB has weaker B-H bond than ammonia borane does. In contrast, both N-H and B-N stretching modes of NaAB displayed higher frequencies than in NH_3BH_3 , suggesting that the strength of such bonds was stronger in NaAB. It should be mentioned that two peaks (3257.1 cm^{-1} and 3183.3 cm^{-1}) in the N-H stretching region possibly originated from the unreacted NH_3BH_3 in the ball milling synthesis.

Table 5.1 Partial assignments and vibrational frequencies (cm⁻¹) of NaAB at ambient pressure

Description	NaAB		NH ₃ BH ₃ ³³	
	Raman	IR	Raman	IR
asym. N-H stretch	3372	3374	3316	3386
sym. N-H stretch	3316	3301	3250	3337
asym. B-H stretch	2189	-	2328	2415
sym. B-H stretch	2112	-	2279	2340
B-H deformation	1262	1266	1189	1186
B-N stretch	905	905	800	987
	-	-	784	968
N-H deformation	-	1379	1357	1343

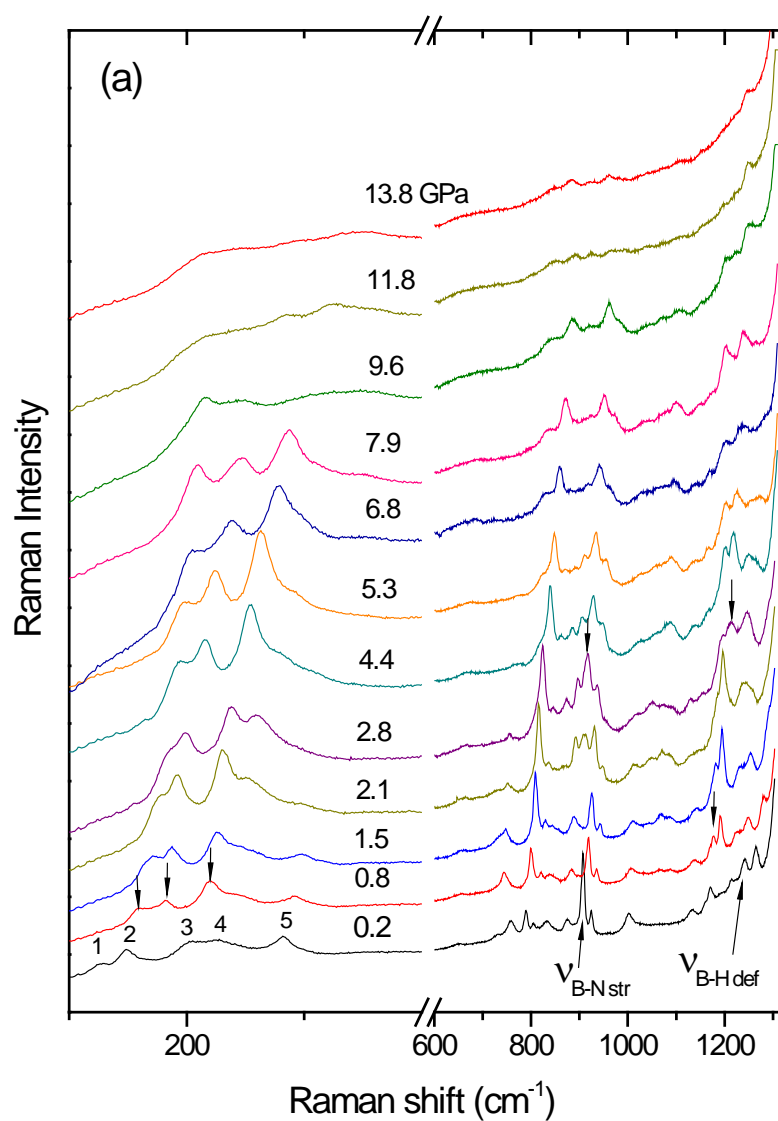
5.3.2 Raman spectra on compression

The Raman spectra of NaAB were collected at pressures from ambient to 13.8 GPa with representative spectra depicted in Figure 5.3. The region associated with lattice modes showed dramatic changes at 0.8 GPa, including obvious blue shifts of modes 1 and 2, as well as increased intensity of mode 3. In the BH_3 deformation region, the peak at 1191.1cm^{-1} split into two components while the peak at 1229.2cm^{-1} markedly faded away. All these significant profile changes, especially the changes in the lattice region, provide substantial evidence of a phase transition at this pressure. The high similarity of the spectra in the range from 0.8 GPa to 2.8 GPa suggest the stability of the new phase in this pressure region.

When the pressure was increased to 2.8 GPa, remarkable changes in the Raman spectra demonstrated another round of phase transition. First, a prominent modification was present in the B-N stretching region, where $\nu_{\text{B-N str}}$ at 916.9cm^{-1} gained considerable intensity. Similarly, $\nu_{\text{B-H str}}$, a previous broad peak at 2251.4cm^{-1} , evolved into a sharp mode. In contrast, in the N-H stretching region, $\nu_{\text{N-H str}}$ at 3393.4cm^{-1} vanished. All the changes mentioned above could be attributed to the new phase transition.

With further compression, the profile lacked prominent changes except for the gradual blue shifts and increasing band width, suggesting that the sample was heading for amorphous phase gradually. At 13.8 GPa, all the Raman modes became extremely broad

and weak. A bit to our surprise, in the entire compression process, a blue shift of the N-H stretching mode was observed. In the case of NH_3BH_3 , obvious red shifts of N-H stretching modes could be observed. The reasons for the different phenomenon will be discussed in the following section.



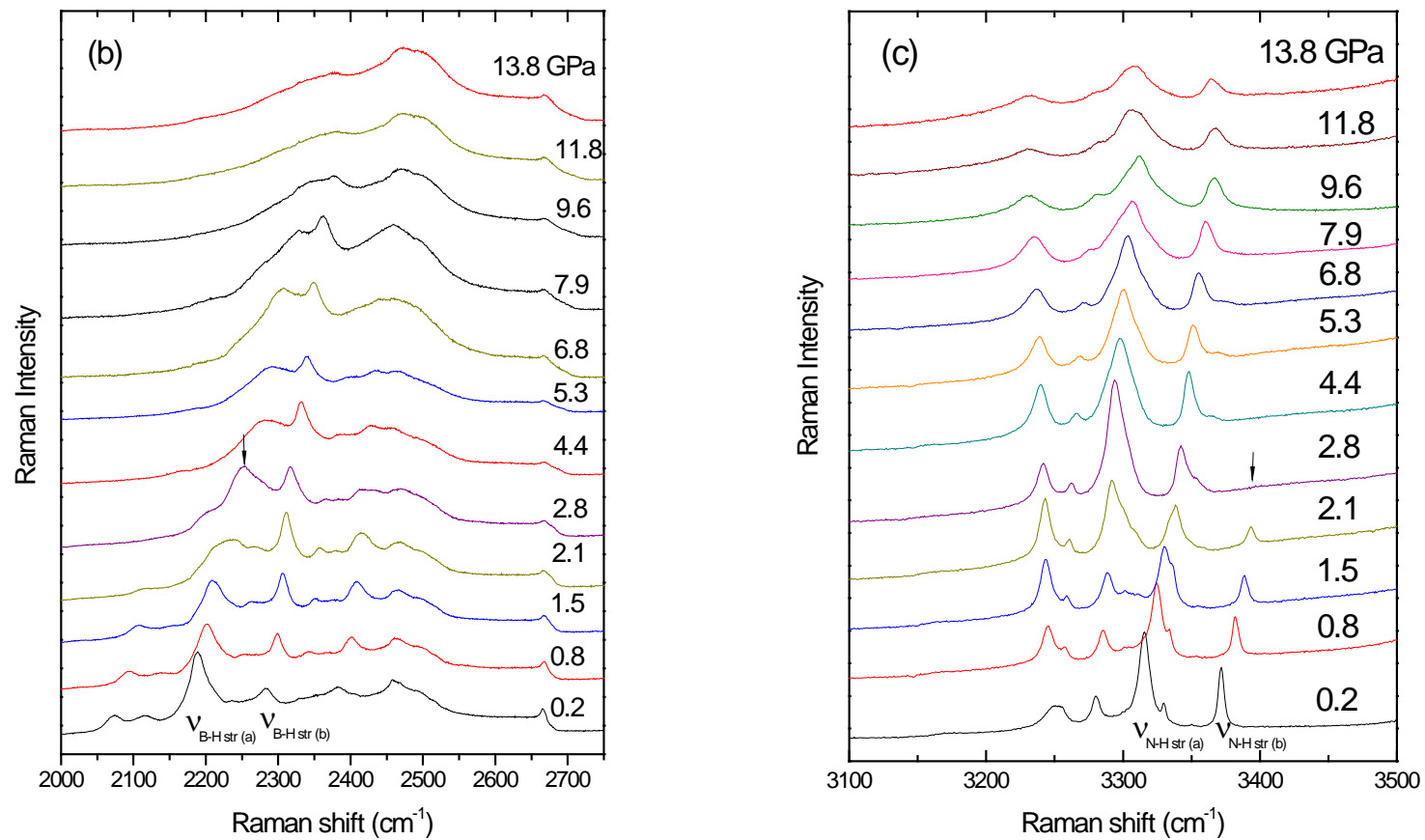


Figure 5.3 Selected Raman spectra of NaAB collected at room temperature on compression in the region of 50-1330 cm⁻¹ (A) 2000-2750 cm⁻¹ (B) and 3100-3500 cm⁻¹ (C) at pressures of 0.2-13.8 GPa. The relative intensities are normalized and thus are directly comparable. The pressures in GPa are labeled for each spectrum. The assignments are labeled for selected Raman modes (see text).

5.3.3 IR spectra on compression

IR spectra were collected as a function of pressure from 0.12 GPa to 13.6 GPa. Selected absorption spectra in the region of 600-3600 cm^{-1} are depicted in Figure 5.4. Upon compression to 0.9 GPa, N-H deformation mode at 1380.1 cm^{-1} developed into a doublet with reduced intensity, in addition to a concurrent appearance of a new peak at 2396.5 cm^{-1} in the B-H stretching region. Meanwhile, the peak at 1604.5 cm^{-1} in the N-H deformation region turned into a sharp peak from a previously broad band. All these evidences mentioned above collectively indicated a phase transition at around 0.9 GPa, in agreement with our observation in the Raman spectra.

Upon further compression, abundant changes at 3.7 GPa clearly marked the second phase transition. First, the formerly pronounced peak at 708.2 cm^{-1} abruptly vanished in contrast to the appearance of a small peak at 894.4 cm^{-1} . More significant changes could be observed in the B-H deformation region, in which the sharp peak $\nu_{\text{B-H def}}$ at 1260.7 cm^{-1} split into two weaker components labeled as $\nu_{\text{B-H def (b)}}$ and $\nu_{\text{B-H def (c)}}$ respectively. Meanwhile, the transformation of the N-H stretching mode at 3311.0 cm^{-1} from a sharp peak into a doublet further evidenced the phase transition. Further compression resulted in the broadening of IR modes. In the entire pressure region, the N-H deformation mode exhibited a red shift, for which the reason is still not clear. In contrast, the N-H stretching modes continued shift to higher frequencies, in accordance with the results of Raman spectra.

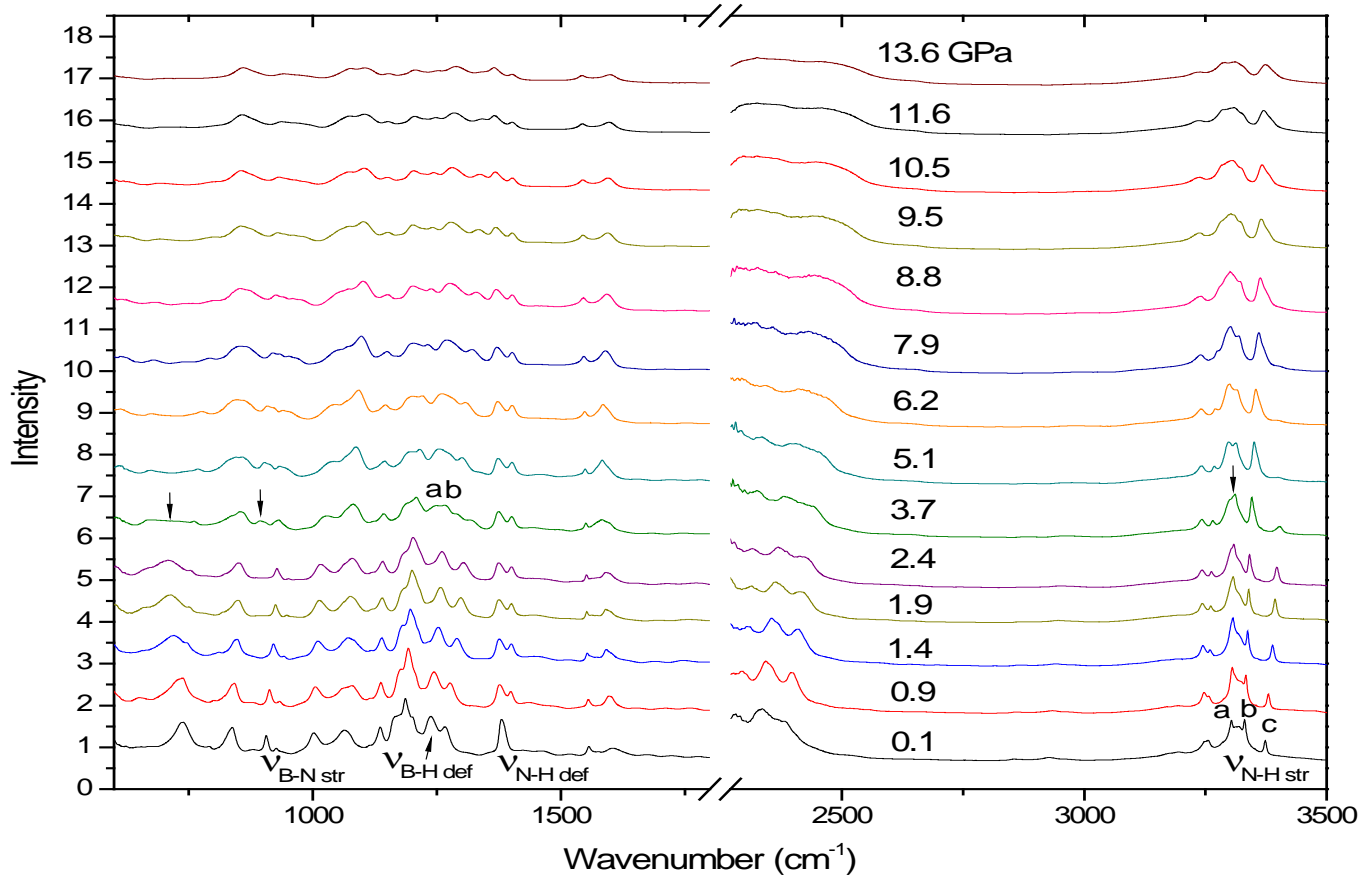


Figure 5.4 Selected IR spectra of NaAB collected at room temperature on compression in the spectral region of 600-3500 cm^{-1} in the pressure region of 0.1-13.6 GPa. The pressures in GPa are labeled for each spectrum respectively. The assignments are labeled for selected IR modes.

5.3.4 Pressure effects on Raman and IR modes

To further examine the possible phase transitions, the pressure dependence of Raman and IR modes (i.e. Raman/IR shift vs. pressure) are plotted in Figure 5.5 and 5.6. Calculated pressure coefficients for the assigned modes obtained by the linear regression of the experimental data are listed in Tables 5.2 and 5.3. The proposed phase transitions could be further proved when different coefficients were observed in different pressure regions.

Upon compression, all the Raman modes displayed pressure-induced blue shifts, consistent with a stiffening of bonds at high pressure. In Figure 5.5, the changes in pressure coefficients were clearly visualized. Overall, the selected modes exhibited lower pressure coefficients in phase III than in phase II (e.g., 10.52 and 2.24 $\text{cm}^{-1}\cdot\text{GPa}^{-1}$ in 0.8-2.8 GPa and 2.8-13.8 GPa, respectively for $\nu_{\text{N-H str (a)}}$), suggesting that phase III is less sensitive to compression. It is also noteworthy that the pressure coefficients of N-H and B-H stretching modes are positive in the three phases.

The monitored IR modes displayed similar trends to the Raman modes. As can be seen in Figure 5.6, the sharp changes in pressure dependence suggest consistent phase boundaries. The positive pressure coefficients of $\nu_{\text{N-H str (a)}}$, $\nu_{\text{N-H str (b)}}$ and $\nu_{\text{N-H str (c)}}$ agreed with the results obtained in the Raman spectra.

Overall, the pressure behavior of the selected Raman and IR modes collectively suggested three pressure regions including 0-0.8 GPa, 0.8-3 GPa and 3-14 GPa.

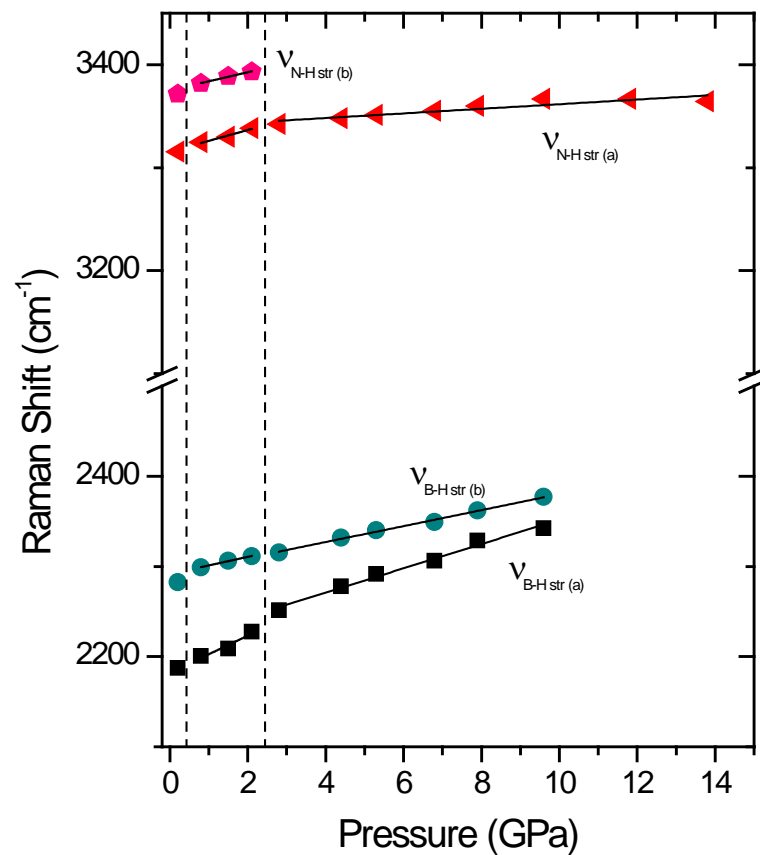
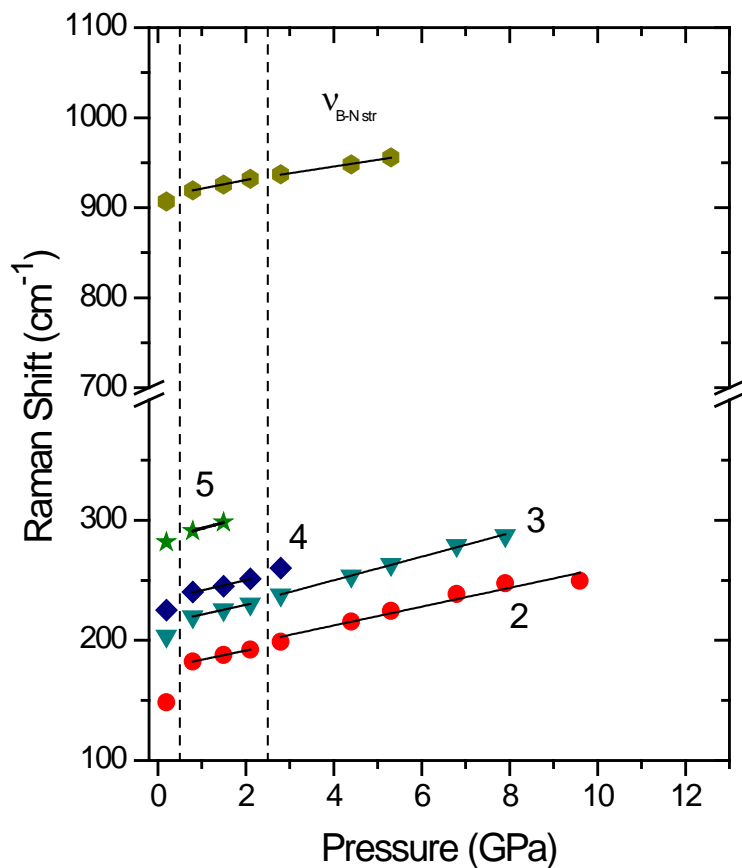


Figure 5.5 Pressure dependence of selected Raman modes of NaAB on compression. Different symbols represent Raman modes with different origins with assignments labeled (see text). The solid lines crossing the solid symbols are based on linear regressions. The vertical dashed lines indicate the proposed phase boundaries.

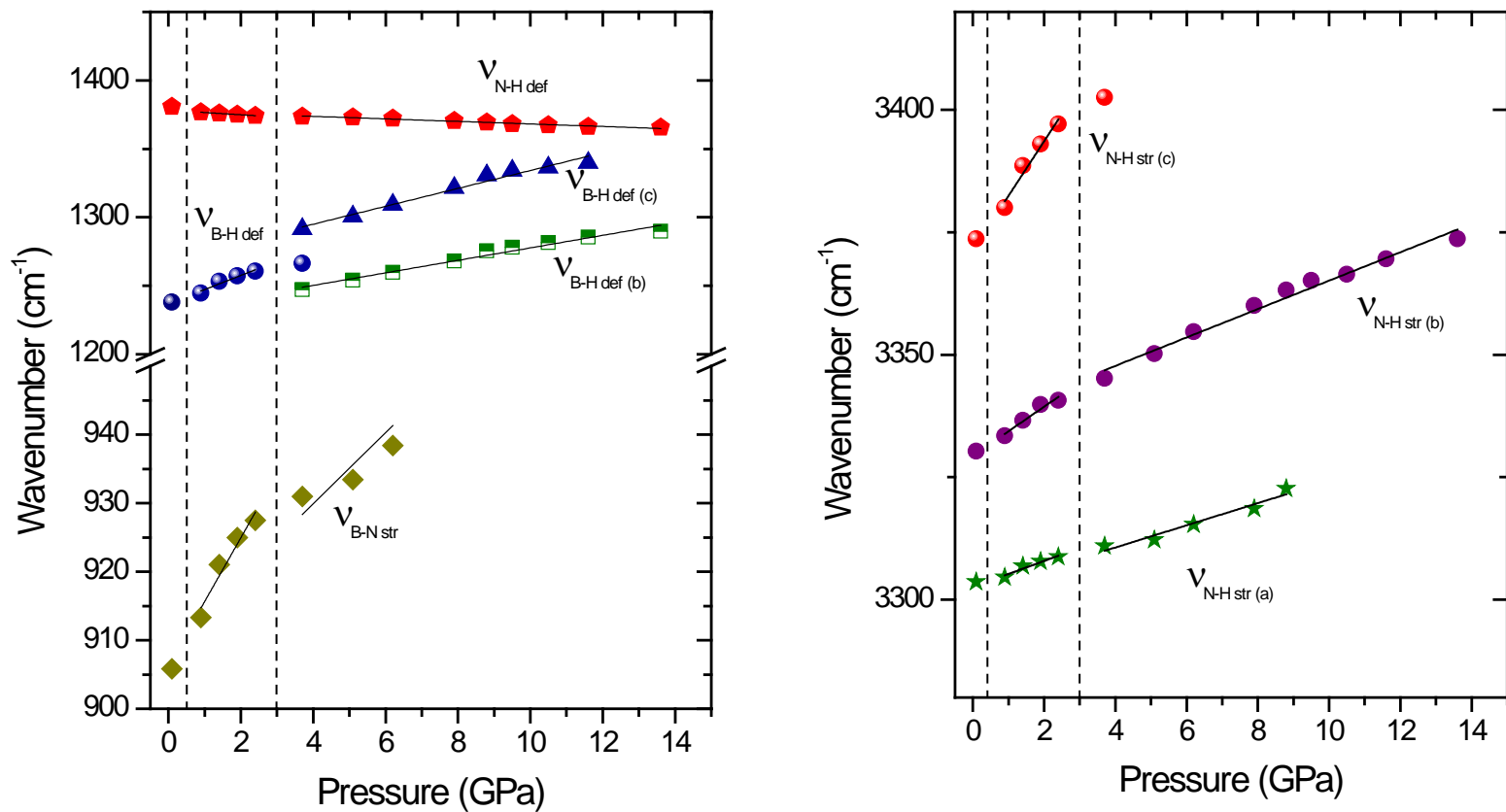


Figure 5.6 Pressure dependence of selected IR modes of NaAB on compression. Different symbols represent Raman modes with different origins with assignments labeled (see text). The solid lines crossing the solid symbols are based on linear regressions. The vertical dashed lines indicate the proposed phase boundaries.

Table 5.2 Pressure dependence of the selected Raman modes of NaAB on compression

Optical Mode	Frequency (cm ⁻¹)	dν/dP (cm ⁻¹ ·GPa ⁻¹) ^a	
		Phase II (0.8-2.8 GPa)	Phase III (>2.8 GPa)
V ₂	148.4	7.6	7.8
V ₃	203.4	8.1	9.8
V ₄	225.1	8.5	-
V ₅	281.7	9.9	-
V B-N str	906.9	9.6	7.5
V B-H str (a)	2187.4	20.6	13.5
V B-H str (b)	2282.5	9.5	8.9
V N-H str (a)	3315.4	10.5	2.2
V N-H str (b)	3371.6	8.8	-

a. The pressure coefficients of phase I was not calculated due to limited data point

Table 5.3 Pressure dependence of the selected IR modes of NaAB on compression

Optical Mode	Frequency (cm ⁻¹)	dν/dP (cm ⁻¹ ·GPa ⁻¹) ^a	
		Phase II (0.9-3.7 GPa)	Phase III (>3.7 GPa)
V B-N str	905.8	9.3	5.2
V B-H def	1238.0	10.3	-
V B-H def (b)	1247.2	-	4.6
V B-H def (c)	1291.5	-	6.5
V N-H def	1380.8	-1.6	-0.9
V N-H str (a)	2187.4	2.7	2.3
V N-H str (b)	2282.5	5.0	2.9
V N-H str (c)	2381.8	11.2	-

a. The pressure coefficients of phase I was not calculated due to limited data point

5.3.5 Raman and IR spectra on decompression

When releasing the pressure, we conducted Raman and IR measurements to study the reversibility of the pressure-induced phase transitions of NaAB. The selected Raman and IR spectra are shown in Figures 5.7 and 5.8. As shown in Figure 5.8, upon decompression, most of the Raman modes followed a back transformation in a reverse sequence to compression. When the pressure was close to ambient, the recovered Raman and IR patterns were almost identical to the initial ones except for the lower intensity and a small upshift of the peak position. The difference between the recovered Raman patterns and the initial profile is likely associated with the hysteresis effect. In the case of IR spectra, the modification of sample thickness in the compression and decompression cycle can also contribute to the difference. In conclusion, the decompression Raman and IR spectra indicated the reversibility of pressure-induced phase transition of NaAB.

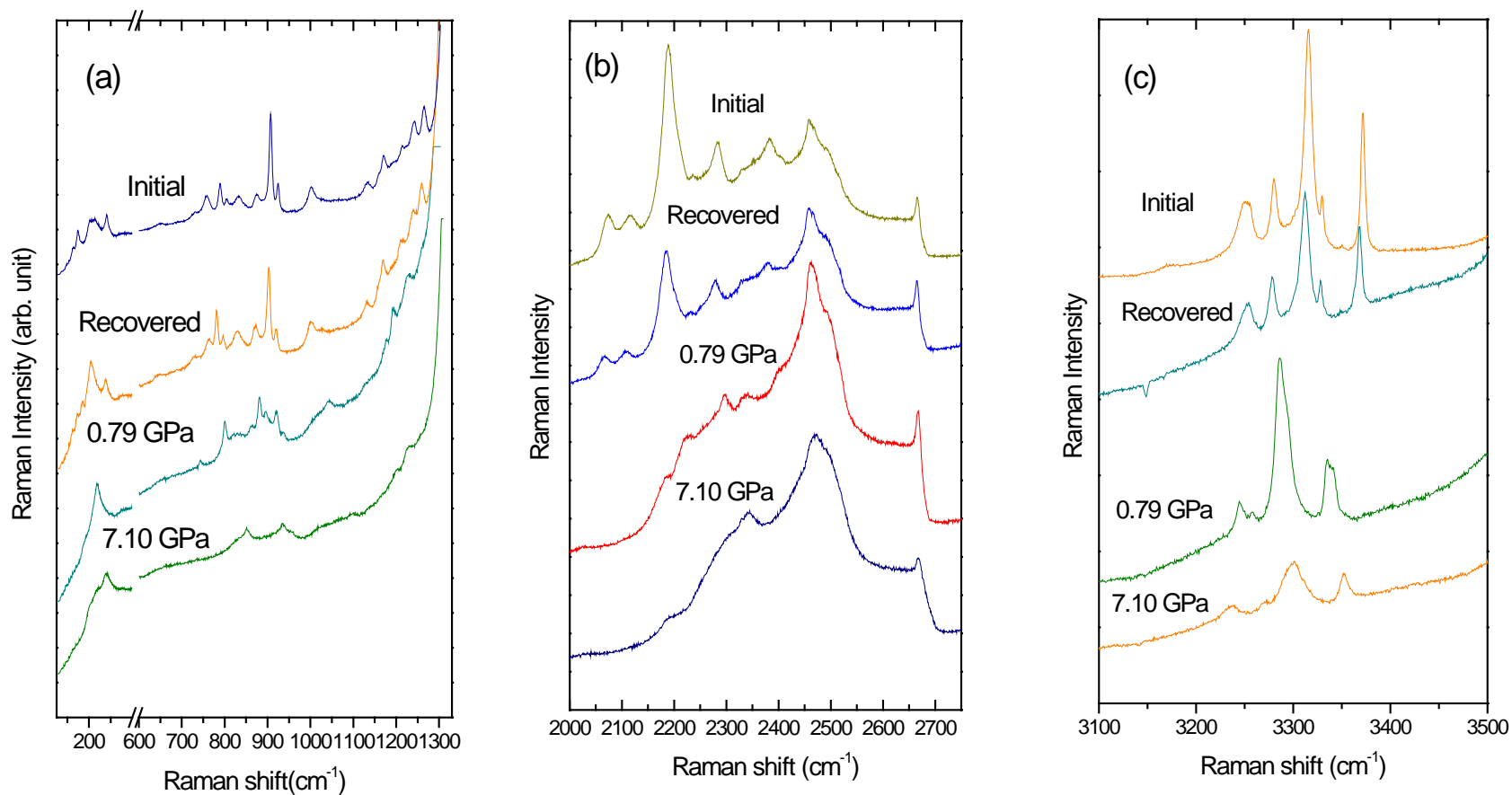


Figure 5.7 Selected Raman spectra of NaAB collected at room temperature on decompression in the spectral region of 50-1330 cm^{-1} (A), 2000-2750 cm^{-1} (B) and 3100-3500 cm^{-1} (C). The pressures in GPa are labeled for each spectrum. The initial near-ambient-pressure spectra before compression (top) are included to compare with the spectra of recovered NaAB.

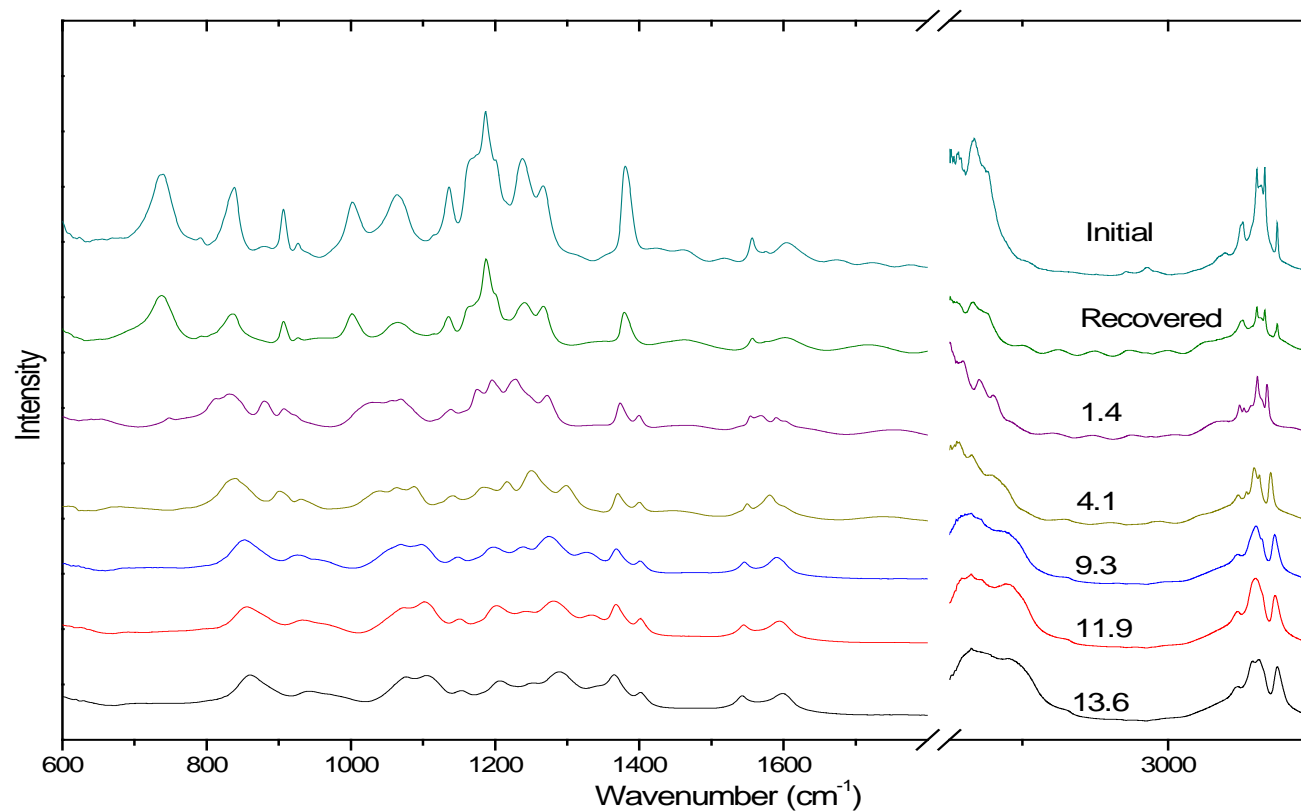


Figure 5.8 Selected IR spectra of NaAB collected at room temperature on decompression in the spectral region of 600-3400 cm^{-1} . The pressures in GPa are labeled for each spectrum. The assignments are labeled for selected IR modes (see text). The initial near-ambient-pressure spectrum prior to compression (top) is included as a comparison with the spectra of recovered NaAB.

5.3.6 Discussion

Our Raman and IR measurements of NaAB on compression up to 14 GPa suggested two pressure-induced phase transitions at 0.8 and 3.0 GPa at ambient temperature. Since the structure and bonding have fundamental influences on the hydrogen storage property, it is of particular interest to understand the new phase and bonding behaviors in different high pressure regions.

The phase in the first pressure region below 0.8 GPa could be interpreted as the extension of orthorhombic structure with space group *Pbca* at ambient pressure. After the pressure was increased to 0.8 GPa, NaAB possibly underwent significant transition in the crystal lattice, which was evidenced by remarkable changes in the Raman and IR profiles, especially the changes in the lattice region mentioned in the above section. At 3 GPa, a phase transition was associated with changes in the major stretching modes such as the evolution of the B-N and B-H stretching modes into sharp peaks in the Raman spectra and the splitting of N-H stretching modes in the IR spectra. These abundant profile changes suggested that the structural complexity increases with pressure, possibly due to enhanced interaction between molecules. The removal of degeneracy in the N-H bond caused by interaction of non-equivalent molecules is likely responsible for the splitting of N-H stretching modes. Upon further compression, the general broadening trend of the Raman and IR bands signified the conclusion that NaAB was on the way to an amorphous

structure.

In the previous high pressure study of LiAB which is isostructural to NaAB, two phase transitions were suggested at 3.9 and 12.7 GPa by Najiba.³⁶ Compared with NaAB, the two phase transitions of NaAB occurred in much lower pressure regions. In Najiba's study, no red shifts of N-H stretching modes were observed, which was consistent with our study of NaAB. In the case of NH_3BH_3 , obvious red shifts of N-H stretching modes were observed, constituting strong evidence for the existence of dihydrogen bonding. In NH_3BH_3 , the $\text{N-H}^{\delta+} \cdots \delta^- \text{H-B}$ dihydrogen bonding strengthens with the increase of pressure, at the expense of $\text{N-H}^{\delta+}$ bond strength, leading to the red shift of the N-H stretching mode. A possible explanation for the absence of dihydrogen bonding in NaAB and LiAB is that the alkali-metal elements such as Li and Na are more electron-donating, and thus N attracts more electrons from alkali metals than hydrogen atoms. In consequence, N-H tends to display covalent character instead of $\text{N-H}^{\delta+}$ while Na-N shows more ionic character. In this case, strong interaction may occur between Na and $\text{B-H}^{\delta-}$, acting as the dominant role to stabilizing the molecular structure of NaNH_2BH_3 despite the absence of dihydrogen bonding in the molecular system.

In earlier studies, many researchers believed that dihydrogen bonding might obviously lower the activation energy for hydrogen release of NH_3BH_3 .^{37,38} Through theoretical calculation, even the homopolar $\text{H} \cdots \text{H}$ interaction in LiNH_2BH_3 and NaNH_2BH_3 , e.g., $\text{B-H}^{\delta-} \cdots \delta^- \text{H-B}$ and $\text{N-H}^{\delta+} \cdots \delta^+ \text{H-N}$ were proposed by McGrady's group who further claimed that such an interaction could help mediate the release of H_2 either directly or indirectly.³⁹

Despite the fact that no hydrogen bonding is observed in the NaNH_2BH_3 and LiNH_2BH_3 molecules in high pressure studies, the onset dehydrogenation temperature of such metal amidoborane is much lower than that of NH_3BH_3 . This interesting phenomenon indicates a different dehydrogenation mechanism, which needs more in-depth research and may provide excellent opportunities to develop novel hydrogen storage materials.

5.4 Conclusion

Using *in situ* Raman and IR spectroscopy, we investigated the structure and phase transitions of sodium amidoborane (NaAB) under high pressures up to 14 GPa. Two phase transitions at around 0.8 and 3 GPa were identified. Three pressure regions were revealed by remarkable and abundant profile changes and different pressure coefficients over different phases. In the first pressure region, NaAB maintained the orthorhombic structure with space group *Pbca*. Upon further compression, NaAB experienced significant structural transformation evidenced by apparent changes in the lattice region. Beyond 3 GPa, NaAB gradually transformed into an amorphous phase, as suggested by the depleted lattice modes and broad band profiles. The pressure induced phase transitions were found to be completely reversible upon decompression. The N-H and B-H stretching modes displayed blue shifts in the entire compression process which was different from the previous study on ammonia borane but similar to another alkali metal amidoborane, lithium amidoborane. This phenomenon pointed to the absence of dihydrogen bonding in

NaAB. The low dehydrogenation temperature of NaAB without the influence of dihydrogen bonding implied a probably different mechanism. Future experiments such as *in situ* X-ray and neutron diffraction are needed to study the phase transition and the absence of dihydrogen bonding.

5.5 References

- (1) Graetz, J. *Chem. Soc. Rev.* **2009**, *38*, 73.
- (2) Staubitz, A.; Robertson, A. P. M.; Manners, I. *Chem. Rev.* **2010**, *110*, 4079.
- (3) Irvine, J. J. *Mater. Chem.* **2008**, *18*, 2295.
- (4) Stephens, F. H.; Pons, V.; Baker, R. T. *Dalton Trans.* **2007**, 2613.
- (5) Marder, T. B. *Angew. Chem. Int. Ed.* **2007**, *46*, 8116.
- (6) Baitalow, F.; Baumann, J.; Wolf, G.; Jaenicke-Rossler, K.; Leitner, G. *Thermochim. Acta* **2002**, *391*, 159.
- (7) Hugel, T.; Hartl, M.; Lentz, D. *Chem-Eur J.* **2011**, *17*, 10184.
- (8) Gutowska, A.; Li, L. Y.; Shin, Y. S.; Wang, C. M. M.; Li, X. H. S.; Linehan, J. C.; Smith, R. S.; Kay, B. D.; Schmid, B.; Shaw, W.; Gutowski, M.; Autrey, T. *Angew. Chem. Int. Ed.* **2005**, *44*, 3578.
- (9) Bluhm, M. E.; Bradley, M. G.; Butterick, R.; Kusari, U.; Sneddon, L. G. *J. Am. Chem. Soc.* **2006**, *128*, 7748-7749.
- (10) Stephens, F. H.; Baker, R. T.; Matus, M. H.; Grant, D. J.; Dixon, D. A. *Angew. Chem. Int. Ed.* **2007**, *46*, 746.
- (11) Neiner, D.; Karkamkar, A.; Linehan, J. C.; Arey, B.; Autrey, T.; Kauzlarich, S. M. *J. Phys. Chem. C* **2009**, *113*, 1098.
- (12) Kalidindi, S. B.; Indirani, M.; Jagirdar, B. R. *Inorg. Chem.* **2008**, *47*, 7424.

- (13) Yan, J. M.; Zhang, X. B.; Han, S.; Shioyama, H.; Xu, Q. *Angew. Chem. Int. Ed.* **2008**, *47*, 2287.
- (14) Zimmerman, P. M.; Paul, A.; Zhang, Z. Y.; Musgrave, C. B. *Angew. Chem. Int. Ed.* **2009**, *48*, 2201.
- (15) Xiong, Z. T.; Yong, C. K.; Wu, G. T.; Chen, P.; Shaw, W.; Karkamkar, A.; Autrey, T.; Jones, M. O.; Johnson, S. R.; Edwards, P. P.; David, W. I. F. *Nat. Mater.* **2008**, *7*, 138.
- (16) Wu, H.; Zhou, W.; Yildirim, T. *J. Am. Chem. Soc.* **2008**, *130*, 14834.
- (17) Wu, C. Z.; Wu, G. T.; Xiong, Z. T.; Han, X. W.; Chu, H. L.; He, T.; Chen, P. *Chem. Mater.* **2010**, *22*, 3.
- (18) Spielmann, J.; Jansen, G.; Bandmann, H.; Harder, S. *Angew. Chem. Int. Ed.* **2008**, *47*, 6290.
- (19) Kang, X. D.; Fang, Z. Z.; Kong, L. Y.; Cheng, H. M.; Yao, X. D.; Lu, G. Q.; Wang, P. *Adv. Mater.* **2008**, *20*, 2756.
- (20) Xiong, Z. T.; Wu, G. T.; Chua, Y. S.; Hu, J. J.; He, T.; Xu, W. L.; Chen, P. *Energ Environ. Sci.* **2008**, *1*, 360.
- (21) Shimoda, K.; Zhang, Y.; Ichikawa, T.; Miyaoka, H.; Kojima, Y. *J. Mater. Chem.* **2011**, *21*, 2609.
- (22) Weng, B. C.; Wu, Z.; Li, Z. L.; Yang, H. *Energy* **2012**, *38*, 205.
- (23) Huang, Z. G.; Autrey, T. *Energ. Environ. Sci.* **2012**, *5*, 9257.
- (24) Chua, Y. S.; Chen, P.; Wu, G. T.; Xiong, Z. T. *Chem. Commun.* **2011**, *47*, 5116.
- (25) Sandra, F. P. R.; Demirci, U. B.; Chiriac, R.; Moury, R.; Miele, P. *Int. J. Hydrogen Energy* **2011**, *36*, 7423.
- (26) Liu, A.; Xie, S. T.; Dabiran-Zohoory, S.; Song, Y. *J. Phys. Chem. C* **2010**, *114*, 11635.
- (27) Liu, A.; Song, Y. *J. Phys. Chem. B* **2011**, *115*, 7.

- (28) Prasad, D. L. V. K.; Ashcroft, N. W.; Hoffmann, R. *J. Phys. Chem. A* **2012**, *116*, 10027.
- (29) Najiba, S.; Chen, J. H.; Drozd, V.; Durygin, A.; Sun, Y. Z. *J. Appl. Phys.* **2012**, *111*.
- (30) Lin, Y.; Ma, H. W.; Matthews, C. W.; Kolb, B.; Sinogeikin, S.; Thonhauser, T.; Mao, W. L. *J. Phys. Chem. C* **2012**, *116*, 2172.
- (31) Liu, A.; Song, Y. *J. Phys. Chem. C* **2012**, *116*, 2123.
- (32) Paolone, A.; Teocoli, F.; Sanna, S.; Palumbo, O.; Autrey, T. *J. Phys. Chem. C* **2013**, *117*, 729.
- (33) Xie, S. T.; Song, Y.; Liu, Z. X. *Can. J. Chem.* **2009**, *87*, 1235.
- (34) Filinchuk, Y.; Nevidomskyy, A. H.; Chernyshov, D.; Dmitriev, V. *Phys. Rev. B* **2009**, *79*.
- (35) Hess, N. J.; Schenter, G. K.; Hartman, M. R.; Daemen, L. L.; Proffen, T.; Kathmann, S. M.; Mundy, C. J.; Hartl, M.; Heldebrant, D. J.; Stowe, A. C.; Autrey, T. *J. Phys. Chem. A* **2009**, *113*, 5723.
- (36) Najiba, S.; Chen, J. H. *Proc. Natl. Acad. Sci. U. S. A.* **2012**, *109*, 19140.
- (37) Fujii, A.; Patwari, G. N.; Ebata, T.; Mikami, N. *Int. J. Mass Spectrom.* **2002**, *220*, 289.
- (38) Lu, J.; Fang, Z. G. Z.; Sohn, H. Y. *Inorg. Chem.* **2006**, *45*, 8749.
- (39) Wolstenholme, D. J.; Titah, J. T.; Che, F. N.; Traboulee, K. T.; Flogeras, J.; McGrady, G. S. *J. Am. Chem. Soc.* **2011**, *133*, 16598.

Chapter 6. Summary and future work

In this thesis, I have studied high-pressure effects on three potential hydrogen storage materials, borane trimethylamine (BTMA), dimethylamine borane (DMAB) and sodium amidoborane (NaAB), by *in situ* vibrational spectroscopy. Our work demonstrated the first high pressure studies of these three compounds and revealed important structural information. Several possible high pressure-induced phase transitions were observed in each sample. Additionally, the structural stability and reversibility of these pressure-induced phase transitions were examined. Based on the changes of Raman and IR profiles, the possible structures in different pressure regions were also discussed. Finally, the implications of the results obtained in our high pressure research were proposed.

Although our study has revealed unprecedented spectroscopic and structural information of BTMA, DMAB and NaAB under high pressure, more in-depth and detailed studies are still needed. For instance, the proposed structures in different pressure regions still remain to be undecided and need to be finally confirmed by *in situ* high pressure X-ray diffraction. Moreover, the dehydrogenation process of such hydrogen storage materials occurs in pyrolysis.¹⁻⁴ For this reason, it is of particular interest to investigate the structural transformation and hydrogen release of these materials as a function of pressure combined with temperature.

Recently, it has been reported that NH_3BH_3 can form a novel H_2 containing complex, i.e., $\text{NH}_3\text{BH}_3\text{-H}_2$, under high pressure.⁵ These novel complexes can store a substantial amount

of extra hydrogen. Therefore, exploring the possibility of synthesizing similar complexes, such as $\text{NaNH}_2\text{BH}_3\text{-H}_2$ under high pressure can further enhance the hydrogen storage performance of ammonia borane derivatives. Finally, theoretical calculations can be adopted to assist with understanding the high pressure behavior and designing novel hydrogen storage materials.

6.1 Reference

- (1) Huang, Z. G.; Autrey, T. *Energ. Environ. Sci.* **2012**, *5*, 9257.
- (2) Jiang, Y.; Berke, H. *Chem. Commun.* **2007**, 3571.
- (3) Shimoda, K.; Zhang, Y.; Ichikawa, T.; Miyaoka, H.; Kojima, Y. *J. Mater. Chem.* **2011**, *21*, 2609.
- (4) Xiong, Z. T.; Yong, C. K.; Wu, G. T.; Chen, P.; Shaw, W.; Karkamkar, A.; Autrey, T.; Jones, M. O.; Johnson, S. R.; Edwards, P. P.; David, W. I. F. *Nat. Mater.* **2008**, *7*, 138.
- (5) Lin, Y.; Mao, W. L.; Mao, H. K. *Proc. Natl. Acad. Sci. U.S. A.* **2009**, *106*, 8113.

Appendix: Supporting materials for Chapter 5

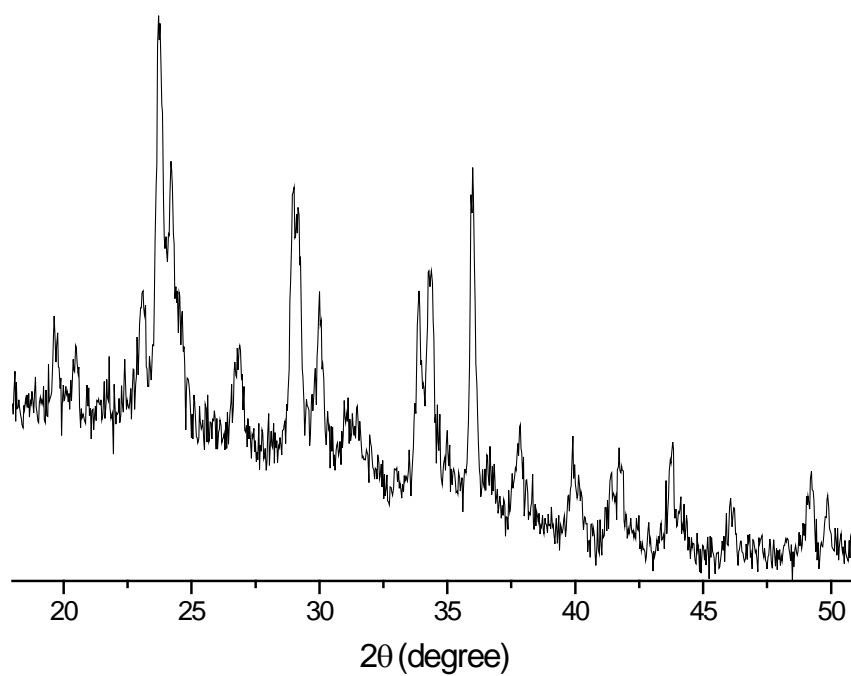


Figure A1. X-ray diffraction pattern of NaNH_2BH_3

Curriculum Vitae

Education

- **Sept. 2011 ~ Present** **University of Western Ontario, Canada**

Major: Physical Chemistry

Degree: Master of Science candidate

- **Sept. 2007 ~ Jun. 2011** **Sun Yat-Sen University, China**

Major: Polymeric Material and Engineering.

Degree: Bachelor of Science

Core Courses:

Graduate Courses:

Synchrotron Radiation, Crystallography I, Structural Chemistry and Solid Material

Patent

"Method for preparing i-type clopidogrel bisulfate" CN 101805354, the fifth author

Conference

11/2012 Poster presentation: *"In Situ High-Pressure Study of Dimethylamine Borane by Raman and IR Spectroscopy"* on CAMBR (Center for Advanced Materials and Biomaterials Research) London, Ontario, Canada.

Career Highlights

- **09/2011-Present** Research Assistant in Song's Group, University of Western Ontario;
- **09/2011-Present** Teaching Assistant for Chem 1100 and Chem 1200 courses, University of Western Ontario.

Awards & Honors

01/2012 Western Graduate Research Scholarship (WGRS);

09/2009 Outstanding Student Scholarship, Sun Yat-sen University;